UNIVERSIDAD AUTÓNOMA DE MADRID

DOCTORAL THESIS

Isotropic nanocrystalline MnAl(C) permanent magnet powder

Author:

Javier Rial Rodríguez

Supervisor:

Dr. Alberto Bollero Real

Facultad de Ciencias

Departamento de Física de la Materia Condensada

Tesis doctoral presentada para optar al Título de Doctor en Ciencias Físicas

Madrid, 25 de Octubre de 2019

Abstract

Permanent magnet composites are characteristic materials that can create their own persistent magnetic field without the need of any other external magnetic field. This unusual property has been taken advantage in the developing of new technological applications, facilitating the production of faster and smaller devices.

The development of new and better permanent magnet compounds during the last century has been possible thanks to the research of new structures and/or through the creation of novel compounds. This tireless research has allowed overcoming some socio-political problems in the continuous technological development and the resource shortage of some valuable elements (rare earths) needed to produce permanent magnets and required in many technological applications. Nowadays, the challenge of finding new permanent magnet materials without Neodymium and Dysprosium (main rare earth elements used in the strongest permanent magnets aimed for room temperature applications) remains. The goal is achieving a diversification in the permanent magnet market sector with the development of rare earth-free alternatives able of filling the gap between ferrites, Alnico and Nd,Dy-based magnets.

This thesis has been focused on the study of one of the most promising alternatives to substitute the bonded Nd-based permanent magnets based on its outstanding intrinsic magnetic properties and abundance of its constituent elements: MnAl. In this research, it is presented an in deep study of the MnAl system by the modification of its micro- and nano-structure and the control of the MnAl-phases present in the material. This research has been performed through the combined use of the gas atomization and the ball-milling techniques, and importantly, exploring the short milling time regime by optimization of the milling process. This approach has made possible to modify its nanostructure, phase transformation process and, in consequence, its permanent magnet properties (with a strong effort focused on coercivity development).

The influence that the choice of parameters in the fast-ball milling process has on the nanostructuring and phase transformation of the MnAl system has been studied in detail. The control of the milling time and the impact energy exerted on the MnAl particles during the process, and the subsequent

annealing treatment needed for development of the permanent magnet properties, are demonstrated to be determining factors to tune magnetization and coercivity in a controlled manner.

The possibility of applying temperature simultaneously during recording of XRD patterns has allowed the configuration of Temperature-XRD maps, thus allowing to observe the gradual phase evolution in MnAl with temperature and, accordingly, the crystallization of the ferromagnetic τ-MnAl phase. This information, in combination with microstructural results, has been decisive to understand the mechanisms behind the development of permanent magnet properties in the MnAl system.

The second part of the research presented in this thesis has focused on establishing the correlation between composition and structure of the starting MnAlC powder with its magnetic properties after the nanostructuring process. The results show a strong dependence of the initial composition in the effectiveness of the nanostructuring process, demonstrating that the Mn:Al ratio in the starting composite influences strongly the final magnetic properties of the alloy. It has also been studied the effect of the initial size of the gas atomized MnAl particles on the ball-milling process, proving that there is a threshold size above which the ultrafast ball milling technique is not efficient in improving the permanent magnet properties.

The novel route here used consisting of combining gas-atomization and ultrafast-milling provides a new method for coercivity development in isotropic nanocrystalline MnAl powders for permanent magnet applications, with potential for industrial implementation based on its short processing time, low-energy consumption, foreseen cost-efficiency, and easy scalability.

Resumen

Los imanes permanentes son materiales característicos que pueden crear su propio campo magnético persistente sin la necesidad de ningún otro campo magnético externo. Esta propiedad inusual es aprovechada en el desarrollo de nuevas aplicaciones tecnológicas, consiguiendo producir dispositivos más rápidos y pequeños.

El desarrollo de nuevos y mejores imanes permanentes durante el último siglo ha sido posible gracias a la investigación de nuevas estructuras y / o mediante la creación de nuevos compuestos. Esta investigación ha permitido superar problemas sociopolíticos en el desarrollo tecnológico y la escasez de recursos de algunos valiosos elementos (tierras raras) necesarios para producir imanes permanentes y requeridos en muchas aplicaciones tecnológicas. Hoy en día, el desafío de encontrar nuevos materiales de imanes permanentes sin neodimio (Nd) y disprosio (Dy) (principales elementos de tierras raras utilizados en los imanes permanentes más fuertes destinados a aplicaciones a temperatura ambiente) permanece. El objetivo es lograr una diversificación en el sector del mercado de imanes permanentes con el desarrollo de alternativas libres de tierras raras capaces de llenar el gap entre los imanes basados en ferritas y Alnico y los imanes basados en Nd-Dy.

Esta tesis se ha centrado en el estudio de una de las alternativas más prometedoras para sustituir los imanes permanentes inyectados de Nd en función de sus excelentes propiedades magnéticas intrínsecas y la abundancia de sus elementos constitutivos: MnAl. En esta investigación, se presenta un estudio profundo del sistema MnAl mediante la modificación de su microestructura y nanoestructura y el control de las fases de MnAl presentes en el material. Esta investigación se ha desarrollado mediante el uso combinado de la atomización de gas y las técnicas de molienda de bolas y, lo que es más importante, explorando el régimen de tiempo de molienda corto mediante la optimización del proceso de molienda. Este enfoque ha permitido modificar su nanoestructura, el proceso de transformación de fase y, en consecuencia, sus propiedades de imán permanente (con un fuerte esfuerzo centrado en el desarrollo de la coercitividad).

La influencia que tiene la elección de los parámetros en el proceso de molienda rápida en la nanoestructuración y la transformación de fase del sistema MnAl se ha estudiado en detalle. Se ha demostrado en este trabajo que

el control del tiempo de molienda y la energía de impacto ejercida sobre las partículas de MnAl durante el proceso, y el posterior tratamiento de recocido necesario para el desarrollo de las propiedades del imán permanente, son factores determinantes para ajustar la magnetización y la coercitividad de manera controlada.

La posibilidad de aumentar la temperatura durante las medidas de rayos X ha permitido la creación de mapas de Temperatura-XRD, que ha permitido observar la evolución gradual de las distintas fases del MnAl con la temperatura y, en consecuencia, la cristalización de la fase ferromagnética τ-MnAl. Estos resultados, combinados con los resultados microestructurales, han sido decisivos para comprender los mecanismos detrás del desarrollo de las propiedades de imán permanente en el sistema MnAl.

La segunda parte de la investigación presentada en esta tesis se ha centrado en establecer la correlación entre la composición y la estructura del polvo de MnAlC inicial con sus propiedades magnéticas después del proceso de nanoestructuración. Los resultados muestran una fuerte dependencia de la composición inicial en la efectividad del proceso de nanoestructuración, lo que demuestra que la relación Mn: Al en el compuesto inicial influye de manera notable en las propiedades magnéticas finales de la aleación. También se ha estudiado el efecto del tamaño inicial de las partículas de MnAl gas-atomizadas en el proceso de molienda de bolas, demostrando que hay un tamaño límite por encima del cual la técnica de molienda de bolas ultrarrápida no es eficiente para mejorar las propiedades del imán permanente.

La nueva ruta aquí utilizada que consiste en combinar el proceso de gas-atomizado y la molienda ultrarrápida proporciona un nuevo método para el desarrollo de la coercitividad en MnAl nanocristalino e isotrópico en polvo para aplicaciones de imanes permanentes, con gran potencial para una futura implementación en la industria gracias a su corto tiempo de procesamiento, bajo consumo de energía, gran rentabilidad y fácil escalabilidad.

Agradecimientos

Este trabajo ha sido posible gracias a la ayuda de muchas personas que, directa o indirectamente, me han permitido construir esta tesis doctoral durante los últimos años.

En primer lugar, me gustaría expresar mi gratitud hacia mi Director de Tesis Alberto Bollero, quien ha hecho posible que hoy esté escribiendo las últimas páginas de este libro. Alberto, tú confiaste en mí cuando era sólo un estudiante de grado y me ofreciste aprender y avanzar a tu lado, hasta el día de hoy. Tu ayuda tanto científica, literaria como personal me ha ayudado a convertirme en el científico que soy. Acabo esta etapa con una mochila llena de conocimientos y experiencias gracias a ti, y sólo me queda darte las gracias por estos años.

Si bien es cierto que fue Alberto quien me ofreció trabajar en el laboratorio de imanes permanentes, esa oferta nunca hubiera sucedido si Marije Villa no nos hubiera presentado. Marije, acudí a ti con un cosquilleo científico hace muchos años, y tu buen ojo sabiendo donde podía encajar me ha permitido acabar siendo doctor, por lo que solo tengo palabras de agradecimiento hacia ti.

Agradecer también la ayuda de Julio Camarero, mi tutor de tesis, quien me encandiló en el magnetismo desde segundo de carrera. Nos conocimos mientras hacia unos experimentos sobre el freno de Foucault hace 7 años, y quien me iba a decir a mí que esos días en el laboratorio cambiarían mi vida para siempre. Tu forma de ver la ciencia motiva a todos los que estamos a tu alrededor, algo que muy pocos consiguen. Gracias por ser el primero en enseñarme el magnetismo, y espero volver a coincidir contigo en algún proyecto de investigación.

En segundo lugar, me gustaría dar las gracias a todas las personas que me ayudaron científicamente durante estos últimos años, los que estuvieron ahí para enseñarme a manejarme por primera vez en un laboratorio de imanes, desde "*los de polvo*" (Noe, Karol, Javi P, Jiayan, Ester, Javi dV, Jose Luis) hasta "*los de láminas*" (Cristina, Eva, Melek). Vuestra ayuda para entender los retos del día a día ha sido crucial para llegar hasta donde he llegado. Quiero hacer una mención especial a Noelia, técnico de laboratorio durante

casi todo mi doctorado. Noe, esta tesis nunca podría haber salido sin ti. La cantidad de experimentos que hicimos juntos me hubieran sido imposible hacerlo en solitario. Una tesis es aprender ciencia, pero también a trabajar en equipo; y eso lo aprendí contigo.

También agradecer la ayuda a los que llegaron después (Dani, Carla, Nadia). Explicar mi trabajo y lo aprendido a vosotros me ha ayudado a consolidar todos esos detalles científicos que a veces pasamos por encima. Espero que disfrutéis del doctorado tanto a nivel científico como personal. Tenéis una carrera enorme por delante y todas las herramientas disponibles para llegar tan lejos como queráis.

A parte de la ayuda científica, creo que es necesario un gran componente humano para sacar una tesis adelante. En este aspecto, quiero volver a mencionar a Carla, Dani, Javi dV y Melek por los cafés, los gswitch, las arañas y las risas. Muchas veces esa desconexión momentánea ayudaba más que mil horas frente a la pantalla. En este sentido, también agradecer a toda la gente del IMDEA que estuvo ahí para desconectar y para divertirse (Diego, David, Fer J, Alberto A, Jose Manuel y mil nombres más).

Agradecer a todos los amigos que estuvieron conmigo durante la carrera, a toda esa *gentucilla* que pasaban conmigo mil horas en la universidad (ya fuera estudiando o jugando al mus) y otras mil de viaje o de fiesta. Si he acabado investigando es porque, gracias a vosotros, nunca perdí el gusto por la física. Vosotros conseguisteis que estuviera contento hasta estudiando *astrófisica cuántica*, conseguíais que pasar horas en la biblioteca no fuera tan malo si podía contar con vosotros. Gracias a Sergio, July, Dario, Alvaro, Raquel, Helena, Pablo, Javi, Mario, Adrian, Melek, Guille y, en especial, a Cris y a Jorge. Poca gente ha aguantado más al *tonto del Rial* que vosotros 2, sufriendo juntos todas esas navidades en la *24h*, intentando fructíferas *alineaciones* (aunque Jorge nunca confiara) y buscando como sacar adelante todo el trabajo atrasado. Creo, sin miedo a equivocarme, que durante la carrera pasé más tiempo con vosotros que con mis padres. Gracias por todas las risas, el apoyo, las copas y los viajes. Disfrutad vuestra etapa en San Sebastián, y nos vemos en el próximo destino.

Agradecer también a Guille por todo lo que vino después de la carrera. Has sido mi compañero de piso, de tesis, y de una etapa de mi vida. Ha sido un placer tenerte al lado durante estos últimos 2 años, viendo como sufrías cada vez que abría una lata de atún…como he disfrutado de estos años de tesis gracias a gente como tú. Que contento estoy de haber podido vivir contigo mi

primera independencia, y te deseo lo mejor en todo lo que te venga por delante.

Dar las gracias también a toda la gente de *Sanse* por la desconexión, el apoyo desde fuera en los momentos malos y por aguantar mis *discursitos sobre lo guays que son mis imanes*. Gracias a los *machos* Pablo, Adrian A, Adrian G, Adrian E, Jose, Sergio y Pablo y a las *gambinas* Marta, Lydia, Raquel, Sandra, Raquel y Sara por todas las fiestas, las vacaciones, las tonterías y las risas. Espero seguir contando con vosotros estemos donde estemos. También a los *guleros* Sergio, Abel, Miriam, Lidia e Idoia por los *viajes*, las escapadas y las desconexiones. Agradecer también en especial a Idoia por su apoyo durante esta etapa final de la tesis, ofreciendo su ayuda para todo lo que estuviera en su mano. Sin ti, estoy seguro de que esta etapa final hubiera sido mucho más difícil. Y, por último, a los *ruben Hood*, los *Etatsila*, los *NoJaimes*, a los que siempre han estado ahí para demostrar que cualquier problema es mínimo si tienes la gente correcta a tu lado. Gracias a Daniel, a Rubén, a Adrián, a Sergio y a Jaime. Más de 10 años juntos, y todo un futuro por delante. Que nada nos cambie, y que estemos donde estemos, siempre tengamos un rato para un *domingo de tertulia*.

Gracias a mi familia, el apoyo incondicional que siempre está a mi lado.

A mi *marti*, a la que me parezco como si fuéramos gemelos, y que nunca se cansará de hacer tonterías conmigo. A Edu, mi hermano pequeño que en muchos aspectos me ha apoyado como un hermano mayor, con el que me he divertido toda mi vida. Hermanos como vosotros son una suerte.

Agradecer por supuesto a mis padres Eduardo y Loli, quienes han hecho posible todas y cada una de las cosas que me he propuesto en esta vida. Vuestro sacrificio por y para mí me hacen sentir tremendamente afortunado. Gracias Papá por enseñarme lo divertido de la ciencia desde pequeño, por tu paciencia y tu empeño en enseñarme que el esfuerzo tiene su recompensa. Gracias Mamá por todo el esfuerzo que has hecho siempre por mí, cuidándome en todo lo que podía necesitar. Vaya donde vaya, voy a necesitar siempre de tus tupper para tener ese extra de energía. Por más *caminos*, más risas y más momentos a tu lado.

Y, por último, quiero darle las gracias a la persona que más me ha ayudado durante mi tesis desde dentro y desde fuera. Melek, me has ayudado en el laboratorio siempre que era necesario en cualquier experimento, en discusiones científicas que conseguían despejar mi mente, con mil bromas para que sacara una sonrisa y, por si fuera poco, te has portado mejor que

nadie desde fuera. Saber que te tenía para cualquier cosa a mi lado ha permitido que las cosas hayan salido así de bien. Ojala cada uno de nosotros tuviera alguien como tú a su lado, porque tu ayuda y tu sonrisa son un tesoro. Nos quedan mil y una aventuras juntos, y espero poder seguir ayudándonos como lo hemos hecho hasta ahora. *Somos equipo.*

Contenido

Chapter 1

1.Introduction

This chapter makes a brief revision of fundamental aspects of permanent magnets (PMs) starting from the characteristic hysteresis loop, which shows the magnetic response of the material to an external field. Intrinsic magnetic properties, which are the base to end with excellent extrinsic magnetic properties through microstructural modification, are explained.

A revision of the historical evolution of permanent magnets is also done, which is closely related to the technological development. Some rare-earth free PM alternatives are described, concluding with the MnAl system, the system under study in this Thesis.

1.1 Permanent magnets

1.1.1 Hysteresis loop

The essential characteristic of any ferromagnetic material is the irreversible nonlinear response of magnetization **M** to an external magnetic field **H**. This response is represented by its hysteresis loop.

In a ferromagnetic material, increasing the external field causes an alignment of its magnetic moments in the same direction than the external field. This alignment of the magnetic moments results in an increase of the induced magnetization. When all the magnetic moments of the material are aligned parallel to the field, the increment of **H** does not promote any change in the measured magnetization. The maximum magnetization obtained in a material is known as *magnetic saturation*, M_s. It is marked in Figure 1 as *point A*. The saturation of a material is an intrinsic property of each material, and it is independent of any external factor.

When the external field **H** is reduced from the maximum achieved value, the magnetic moments begin to desalinate due to their thermal energy and internal forces that rotates the magnetic moments to other preferential orientations. When the external field is completely removed, i.e. **H= 0**, there is a residual magnetization in the sample because of net sum of all the magnetic moments

of the material, which is known as the "memory" of the system. The residual magnetization presented in one material is defined as *remanence magnetization*, M_r, and it is marked in Figure 1 as *point B*. The remanence is an extrinsic property which depends on a host factors including the sample shape, surface roughness, microscopic defects, thermal story, as well as the rate at which the field is swept in order to trace the loop. Experimentally, the materials present an intermediate remanence between 0 and M_s.

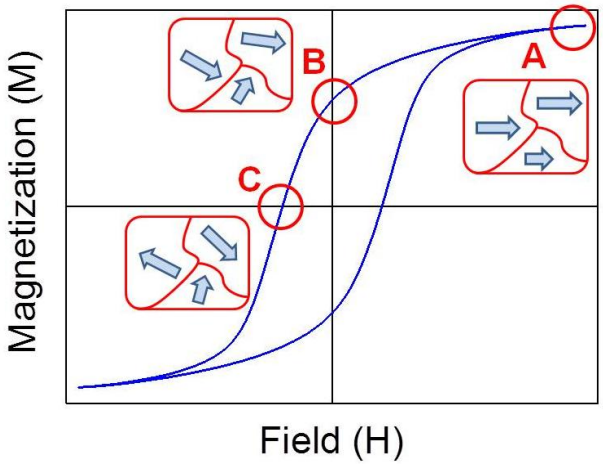

Figure 1. Hysteresis loop of a magnetic material, where it has been marked the most characteristics values: (A) the maximum magnetization obtained, M_s, (B) the magnetization which remains when the applied field is restored to zero, M_r, and (C) the reverse field needed to reduce the magnetization to zero, H_c.

If the external field is reversed, the magnetic moments will start to nucleate in this sense, causing a detriment in the net magnetization of the material. As the magnetic field increases in the opposite direction, the total magnetization of the material decreases, until the external field reaches a value at which the net magnetization in the material is zero. The field necessary to desmagnetize the material (i.e. M= 0) is defined as *coercivity field*, H_c. It can be found in Figure 1 as *point C*.

The highest coercivity that can be reached occurs when all the magnetic moments maintains, in absence of external field, the same orientation than in the saturation state and all of them nucleate at the same external field. If all the magnetic moments nucleate to the opposite sense at the same external field, the material will be still saturated, but in the opposite direction. It means that the coercivity will be the same field than the necessary to saturate the material, and it will be determined just by the structure and the constituent elements of the compound. The highest coercivity that theoretically might be possible in one material is known as anisotropy field and it is represented as H_k. Nevertheless, as the coercivity is an extrinsic property, the value will

depend on other factors like shape and size of the sample or the external temperature. Consequently, the coercivity of one material will be a value between 0 and H_k.

Depending on the applications, the desired magnetic properties will be different. By definition, a permanent magnet *is an object than creates its own persistent magnetic field, without the need of any other external field*. Based on that, the desired remanence magnetization in a permanent magnet must be as high as possible. In addition, in order to maintain the magnetization during its use, it is necessary a high coercivity to avoid its demagnetization if any other magnetic field is close to the object.

In consequence, the best optimization of the remanence magnetization and coercive field is achieved if all the magnetic moments are still aligned in absence of external field (i.e. $M_r = M_s$) and they nucleate simultaneously at the highest field possible (i.e. $H_c = H_k$). It means that the best magnetic properties for a permanent magnet in a material will be limited at first instance by its saturation and its anisotropy field, two intrinsic properties.

However, while it is true that the highest magnetic properties of a permanent magnet are determined by its intrinsic properties (M_s and H_k), the defects of the material or the absence of the perfect geometry in the "real" permanent magnets makes impossible to obtain the theoretical properties of the magnetic material in a manufactured permanent magnet.

1.1.2 Maximum energy product, $(BH)_{max}$

The maximum energy product of a magnet, $(BH)_{max}$, is a measurement for the maximum amount of magnetic energy stored in a magnet. The $(BH)_{max}$ can be considered as the magnetic density of one material, and it is considered the figure of merit of the permanent magnets.

The maximum energy stored in a magnet is calculated from **B**, the magnetic flux density, which is calculated by the equation [1]:

$$\mathbf{B} = \mu_0(\mathbf{H} + \mathbf{M}) \qquad (1)$$

Where H is the applied external field and M is the induced magnetization in the material and μ_0 is the magnetic permeability in a classical vacuum.

As it is shown in equation 1, the magnetic flux density depends linearly with the magnetization , so it also has an irreversible non linear dependence with the external field. However, as the magnetic flux density has a second linear contribution of H, due to the external magnetic field that is passing through the material, the hysteresis loop of **B** presents important differences compared with the hysteresis loop of **M**, as it is shown in Figure 3.

Despite the energy stored only can be calculated from **B,** the characterization of the magnetic materials is done through the induced magnetization. For that reason, hereinafter, the representation that will be showed in the manuscript is the M(H) hysteresis loops.

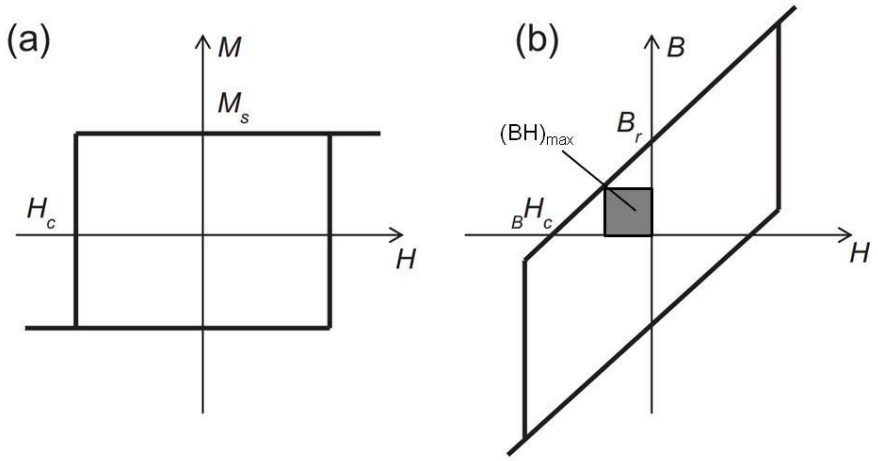

Figure 3.Representation of an ideal hysteresis loop of (a) *M(H)* and (b) *B(H)* [2]. The shaded area in the B(H) representation corresponds to the $(BH)_{max}$ of the material.

In a visual way, the $(BH)_{max}$ is the maximum value of BxH on the second quadrant of the B-H loop (shaded area in Figure 3 (b)).

It is equal to $\frac{1}{2}\int|BH|dV$ [3], where the integral is over the magnetic volume.

In this integral, the field *B* is the field generated by the magnet, and H is the demagnetizing field, that can be approximately related to the magnetization by [2]:

$$H_d \approx -NM \qquad (2)$$

Where N is a factor that will be between 0 and 1, and it depends only on the magnetic shape. To calculate the maximum energy product, it is considered that the magnetization in the material is always the saturation magnetization

and the coercive field is equal to H_k, i.e. the hysteresis loop of the magnetization is a square.

By combination of equation 1 and 2,

$$|BH| = \mu_0(-NM + \mathbf{M}) \times (-NM) = \mu_0 M_s^2 (N - N^2) \quad (3)$$

Differentiating with respect to N to find the $(BH)_{max}$ it is obtained that N has to be 0.5, and

$$|BH|_{max} = \frac{1}{4}\mu_0 M_s^2 \quad (4)$$

This is the maximum value for the energy product of a magnet. However, as the magnetization normally deviates from the ideal square loop supposed during the calculation, the $(BH)_{max}$ of the materials is always lower than its theoretical energy product.

As an example, if one material is isotropic and it does not have any texture, the maximum remanence magnetization will be $\frac{M_s}{2}$, so the maximum value for the energy product will be reduced by 4.

During the history, the main challenge with permanent magnets has been always the improvement of the $(BH)_{max}$. This evolution is presented in the following section.

1.1.3 Intrinsic magnetic properties

The intrinsic properties are independent of how much of a material is present and it is also independent of the shape of the magnet. The intrinsic properties are mainly dependent on the fundamental chemical composition of the material and its crystallographic structure.

The intrinsic magnetic properties in a permanent magnet are the *Saturation magnetization*, the *Curie temperature* and the *Anisotropy field*.

1.1.3.1 Saturation magnetization

As it was explained in section 1.1.1, the saturation magnetization is the maximum magnetization possible in the material under application of a

sufficiently strong external magnetic field, and it is related with the magnetic moments of the material. As it is an intrinsic property, the domains size or the defects in the material cannot modify its value. It will only be determined by the sum of the magnetization moment of each atom, which will depend on the crystal structure.

Each element of the periodic table has different magnetic moment, so the magnetization of the constitutional elements will explain the total magnetization of the material. Because of that, diamagnetic elements are not desired in a permanent magnet since they are repelled by a magnetic field. The desired elements in a permanent magnet are the paramagnetic and the ferromagnetic ones, because they are attracted by a magnetic field.

The other important factor is the crystallographic structure. The net magnetic moment of one unit cell will be given by the sum of all the magnetic moments inside it, and the kind of structure will determine the ferromagnetic/antiferromagnetic coupling of the atoms. As an example, if some atoms of iron (ferromagnetic) are coupled antiferromagnetic between them, the net magnetization will be reduced.

The combination of the choice of proper elements and the optimal structure for these elements is determinant to build a competitive permanent magnet.

1.1.3.2 Curie temperature

In physics, the Curie temperature, T_c, is the temperature above which ferromagnetic materials lose their permanent magnetic properties [1].

It has been explained before that the magnetic moments of a ferromagnetic material aligns parallel to an external field, and it can maintain the magnetization when the external field is removed. When the temperature of the system increases, the alignment of the magnetic moments becomes weaker, and some of the moments will start to be randomly oriented, decreasing the total magnetization. The Curie temperature is defined as the temperature at which the total magnetization is zero, or what it is the same, the temperature at which all the magnetic moments are randomly oriented.

The Curie temperature will determine, therefore, the possible applications of a permanent magnet. One permanent magnet can be good enough at certain

temperatures and to become useless if the working temperature of the magnet is above its Curie temperature.

1.1.3.3 Magnetocrystalline anisotropy and anisotropy field

Anisotropy is the property of being directionally dependent, which implies different properties in different directions. In magnetism, this term means that the magnetic properties depend on the direction in which they are measured.

There are several kinds of anisotropy in magnetism: magnetocrystalline anisotropy, shape anisotropy, stress anisotropy or exchange anisotropy [1] [4]. Among them, only magnetocrystalline anisotropy is intrinsic to the material.

The magnetocrystalline anisotropy is the interaction between the crystal electric fields and the localized electrons. As a consequence of that, the primary source of this anisotropy comes from the spin-orbit interaction. The orbital motion of the electrons couples with the crystal electric field, creating direction where the energy is minimal, the "easy"-axis. This interaction will tend to align the spontaneous magnetization along the preferential direction. Generally, the tendency for magnetization to lie along an easy axis in a uniaxial material is represented by the energy density term [4]:

$$E_a = K_1 \sin^2 \theta + K_2 \sin^4 \theta \quad (5)$$

Where θ is the angle between M and the anisotropy axis, and K_1 and K_2 are the magnetocrystalline anisotropy constant of the material.

If the material is magnetized along its easy-axis, it will easily maintain the magnetization parallel to the external field during the demagnetization process. In an ideal case where there is no thermal energy, the magnetic moments will be always aligned in the same direction, and they will only change the sense when the applied external field is high enough as to nucleate the moments parallel to it.

In the opposite case, if the material is magnetized along its "hard"-axis (the perpendicular direction to the easy-axis), the magnetic moment of the material will rotate from the hard to the easy-axis when the external field is removed. In this case, it will be produce a coherent rotation of the magnetic moments. The field needed to saturate the magnetization of a uniaxial crystal in a hard direction is defined as the anisotropy field, H_k.

This field can be determined by

$$H_k = \frac{2K_1+4K_2}{\mu_0 M_s} \quad (6)$$

As it was explained in the previous section, this field represents the maximum possible coercivity that might be achieved in one material. In consequence, as the magnetocrystalline anisotropy is related to the anisotropy field, a high anisotropy raises the coercivity of the material.

Materials with a high magnetic anisotropy will easily maintain their own magnetization during the demagnetization process, obtaining a high coercivity and a high remanence magnetization. On the other hand, materials with low magnetic anisotropy usually have low coercivity.

Nevertheless, it is important to remark that the anisotropy field just determines the upper limit of the coercive field in the material. Defects and other inhomogeneities can reduce the coercivity of the real magnet.

1.1.4 Coercivity

The coercivity is the intensity of the applied magnetic field required to reduce the magnetization of one material to zero, after the magnetization of the sample has reached the saturation value. In other words, the coercivity of one material is the resistance of the material to becoming demagnetized.

The coercivity of one material has an upper limit determined by the anisotropy field, as it was explained before. This value only can be reached if the magnetization reversal of a single-domain particle occurs through nucleation of the magnetic vector from one easy axis to another. However, the coercivity measured in the particles is always lower than the anisotropy field, being generally just 20-30% of the anisotropy field [3]. This appararent contradiction between the *real* coercivity and the *theoretical* coercivity is known as Brown's paradox [3]. The reason of the difference between them is that all real materials are inhomogeneous, and magnetization reversal is initiated in a small nucleation volume around a defect. The complex magnetization reversal process, which is sensitive to the size of the particles and its microstructure, reduces the maximum coercivity of the material.

Figure 2 from the book of J.M.D. Coey [3] summarizes the processes involved in magnetization reversal. The control and analysis of the factors

mentioned is necessary to understand the coercivity of the system and to increase it.

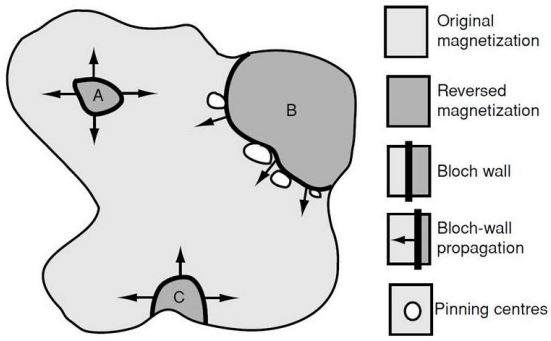

Figure 2. Processes involved in magnetization reversal. *A* is a reversal domain which nucleates in the bulk at a defect, *B* is a reverse domain which has grown to the point where it is trapped by pinning centres and *C* is a reverse domain which nucleates at a surface asperity [3].

The first important factor that must be considered is the size of the domains and the particles. The magnetic domains theory explains that if one ferromagnetic material is cooled below the T_c, the local magnetization of a ferromagnetic particle can spontaneously divide into many magnetic domains, which are separated by domain walls.

While in each domain the magnetization points in a uniform direction, the direction of the magnetic moments in different domains may not be the same. Therefore, the vector sum of all the magnetic moments will be lower than the sum of the net moment of each magnetic domain. The presence of a multidomain structure will also cause the appearance of propagative demagnetization process. If one magnetic domain nucleates, it will propagate along the material to the adjacent domains (Figure 2), making not necessary to apply a field strong enough as to nucleate all the magnetic domains. It will be sufficient to apply a field high enough to nucleate just one domain, decreasing therefore the coercivity in the system. As the number of magnetic domains in a particle increases, coercivity decreases.

Only if the particle size is smaller than the critical diameter (D_s) the whole particles includes only one stable magnetic domain. This system is known a single-domain particle. In this system, there is only presence of non-propagative demagnetization process, according to the Stoner-Wohlfarth theory [5] [4]. In this case, the coercivity decreases as the diameter of the

magnetic particles deviates from D_s. Then, the optimal coercivity is obtained in a single-domain magnet with the diameter of the particle close to D_s. The critical diameter of the domain depends on a balance of three energies including exchange, anisotropy, and magnetostatic energy within a magnet.

In a multidomain system where the demagnetization process occurs by nucleation and propagation of the domains, it is possible to raise the coercivity by the domain wall pinning (Figure 2). These nonmagnetic inclusions (normally inhomogeneities in the samples) can pin the domains walls, reducing the velocity of their movement [3]. Strong pinning arises when the defects have a dimension comparable to the domain wall width, and planar defects are the most effective pinning centres because the whole wall finds itself with a different energy when it encompasses the defect. Weak pinning occurs when many small defects are distributed through the wall.

The second factor that will limit the coercivity is the microstructure. According to Kronmüller et al. approximation [6], the coercivity can be defined as

$$H_c = \alpha H_k - N_{eff} M_s \quad (3)$$

Where α and N_{eff} are microstructural parameters. α is a corrective factor applied to the anisotropy field, and its value is in the range of $0 < \alpha < 1$, depending on the defects and grain alignment. N_{eff} is the effective demagnetization factor, stemming from macroscopic sample, or the microscopic grains. It resides in the demagnetization field that is induced due to the presence of free magnetic poles on the surface of the magnetized particle (figure 2).

1.2 Historical evolution of permanent magnet materials

The huge increment of the number of technological devices during the last century has caused a big expansion of the permanent magnets market, due to the necessity of permanent magnets in many applications. The technological objective throughout the history of continuous improvement of the current devices has always required searching for new magnetic materials whose properties allow creating more powerful magnets than the previous ones in a particular volume of space.

From the first *natural magnets* based on magnetite (Fe_3O_4) to the strongest magnets produced nowadays based on neodymium, the investigation of new and better permanent magnets has allowed to discover new materials during the last century.

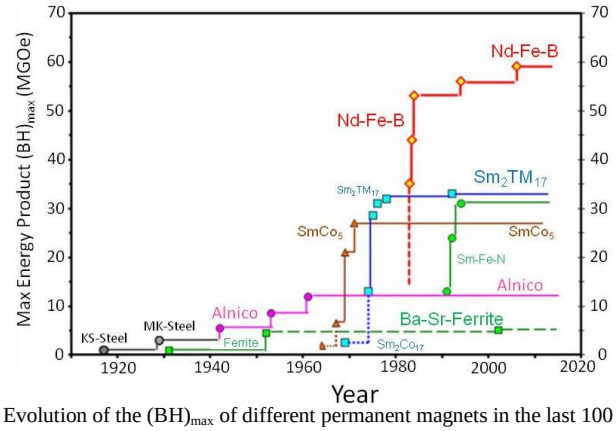

Figure 4. Evolution of the $(BH)_{max}$ of different permanent magnets in the last 100 years [7]

Without taking into account the magnetite (since it is a natural magnet), the first artificial magnet was produced in 1745 by Gowin Knight[8]. It was based on magnetized steel, and it was the strongest magnet until the XX century, when the steel magnets were enhanced by the addition of cobalt, increasing their coercivity.

The first important advance was achieved in 1930, when T. Mishima discovered that an alloy of iron, nickel, aluminium with minority additions of Cu Ti and Si had a coercivity of 400 Oe, double that the best magnets based on steel of the era [9]. These magnets were called Alnico, due to their majority composition of aluminium (Al) nickel (Ni) and cobalt (Co) [4].

The magnetization in this kind of magnets derives from the formation of two different phases in the alloy, one ferromagnetic FeCo-rich and one weakly

magnetic NiAl-rich phase. The processing performed nowadays in these alloys has allowed to reach $(BH)_{max}$ values in the range of 5-7 MGOe [10]. Furthermore, several alnicos alloys present some of the highest Curie temperatures of any magnetic material discovered to the date, with Curie temperatures around 800 ºC [11]. However, the main problem with Alnicos magnets was their low coercive field, being them easily demagnetized by an external field

Despite the big difference between the magnetic properties of the Alnicos and steel magnets, the most relevant achievement accomplished with the Alnico magnets was the beginning of new way of thinking about magnetic materials: the idea of a multiphase system where the combination of all of them creates a new composite material with better magnetic properties that those of the individual components alone.

After the discovery of the Alnicos, the next revolution came from the hexaferrites, based on iron-oxide, when the Philips Natuurkundig Laboratorium sintered for the first time barium hexaferrite, in 1950 [12]. These magnetic iron-oxide compounds possess a typical composition $MFe_{12}O_{19}$ (or $MO\text{-}6Fe_2O_3$, for this reason they are called hexa-ferrites), where M represents the divalent metals Ba, Sr, or Pb [13] [14]. The hexaferrites are ferrimagnetic, with both ferromagnetic and antiferromagnetic coupling between atomic moments; and the magnetic coupling depends on the specific crystallographic position of Fe ions, through oxygen-mediated indirect superexchange interactions. These magnets possess a rather low $(BH)_{max}$, below 5 MGOe [14], but their low price and their electrically insulating properties made them a very important alternative since 1950 until these days.

The golden age of the permanent magnets would come twenty years later, by the discovery of the rare-earth magnets. The composites made with a mixture of rare-earth (RE) elements and transition metals (TM) pulverized all the magnetic properties records achieved till the date with other magnetic materials.

In the 1960s, Strnat et al. reported, for the first time, high energy products in ferromagnetic intermetallic phases of the types $RE(TM)_5$, with the hexagonal $CaCu_5$-type crystal structure [15]. It was astonishing the large magnetization in these compounds, donated by the RE-elements, achieving a record $(BH)_{max}$ of 5.1 MGOe with $SmCo_5$, later optimized to almost 18 MGOe [16].

In 1970s, the research of the RE-permanent magnets resulted in a new RE-based intermetallic compound, the $RE_2(TM)_{17}$. The “2-17” compound present

similar crystal structure than the "1-5" compound, but the higher content of cobalt offers a higher magnetization, raising the $(BH)_{max}$, as well as a higher Curie temperature [17]. The compound Sm_2Co_{17} reported a theoretically $(BH)_{max}$ of 60 MGOe [18], but the commercialized Sm_2Co_{17} magnets had a energy product between 22 and 32 MGOe [19] [20].

However, the high price of Sm and Co and the geopolitical events made necessary to find a Co-free alternative, using iron-based rare-earth compounds. The first attempts with Fe (instead of Co) show that the Re_2Fe_{17} magnets had a low Curie temperature and low magnetocrystalline anisotropy [21] [22], so it was discarded as a permanent magnet material. Nonetheless, in 1984, when it was trying to form new "2-17" Co-free magnets, a new Fe-based magnet based on the ternary $Nd_2Fe_{14}B$ phase was discovered quasi-simultaneously by General Motors, Sumitomo and the U.S. Naval Research Laboratory [23] [24] [25]. The key component in the discovery of this permanent magnet was the use of boron during the attempts trying to make Nd_2Fe_{17} stable, which led to form this ternary intermetallic compound, the $Nd_2Fe_{14}B$ [23]. The complex structure of this compound is a tetragonal structure with 68 atoms and 6 crystallographic distinct iron sites per unit cell [26]. These new permanent magnets were commercialized in mid-1980s with a $(BH)_{max}$ in the range of 5 to 60 MGOe [27], depending on the detailed composition. However, if it is true that the magnets present the highest energy product reported, they have a low Curie temperature of 300-400 ºC [26] [28], so the operating temperature is restricted to 100 ºC. This problem was partially-solved with the addition of Dy as dopand [29], increasing the operating temperature above 150 ºC.

Years later, trying to reduce the cost of the magnets, the $Nd_2Fe_{14}B$ were combined with epoxy to form bonded magnets [30], reducing their $(BH)_{max}$ 4 times. However, it is enough to cover the applications where it is not necessary a high energy product and more intricate shapes are needed.

From the 1980s until today, the PM-market has been dominated by the SmCo and the NdFeB permanent magnets.

However, as in the 1980s when the problem with the Co-supply did necessary to find new alternatives, the resource supply problem that has been raised after the RE-crisis originated by China (China supplies more than the 80% of the total RE) in 2012 has created again the necessity to find new alternatives [31]. If 40 years ago the scope was the creation of new permanent magnets

without cobalt, the challenge at present is the production of new PM-composites without rare-earth materials.

1.3 RE-free permanent magnet alternatives

1.3.1 Criteria and viability of proposed alternatives: towards a common sense-mediated market diversification

Unlike the previous crisis, when the exclusion of the cobalt did not avoid the production of permanent magnets with a theoretical $(BH)_{max}$ higher than the existing ones, the exclusion of rare-earth elements as a constituent of the new composites will limit the maximum energy product that can be achieved. For that reason, it would be too optimistic to talk about a new magnetic composite that will substitute the RE-PM in all the applications where they are being used in a short-medium term.

The big expansion of new technologies in this century has allowed the fabrication of a large number of different devices, each of them with different energy necessities. According to a market report produced by MCP in 2015, the total sales of PMs are distributed to an approximately 50-50 between RE-PMs and by PMs based on ferrites [32]. Hard ferrites are extensively used in electric motors where it does not demand a requirement on power density, due to their low cost [33]. However, for those applications that do have a tight weight and size limitation, such as the generator in a wind turbine, ferrites magnets are useless and the RE-PMs are the only choice. Nevertheless, the performance gap between hard ferrite magnets (< 5MGOe) and RE sintered magnets (>30 MGOe) causes that several motors and applications with moderate requirement on power density are using RE-PM because there is no alternative without rare earth materials [34]. Based on that, one possible way to try to solve the problem with the rare-earth materials would be the research of alternatives attending on the actual demand in the permanent magnets market. The scope of the new research is, thus, to develop new magnets that could fill the gap between hard ferrites (5 MGOe) and RE sintered magnets (30 MGOe).

The search for new permanent magnets to fill the gap needs to meet certain requirements. In addition to the condition of the exclusion of RE-materials as a constituent, the composite must be cheaper than the current alternatives or the RE-magnets themselves. Cui et al. designed a table where it is compared the cost and the magnetic properties of the actual magnets, and they calculated

the cost properties ratio of the actual magnets [34]. This ratio is the magnet cost ($/kg) divided by remanent magnetization and by coercivity (Table 1). Any viable alternative proposed should offer a better ratio than ferrites or RE-magnets.

Table 1. Comparison of the different cost properties ratio for the most used permanent magnets nowadays, and their estimation for 2022 [34].

Composite	$/kg/kG/kOe	
	2016	2022
NdFeBDy	0.23	0.46
SmCo	0.78	1.17
Ferrite	0.33	0.33

1.3.2 Examples of RE-free magnets alternatives

1.3.2.1 $L1_0$-Type alternatives

The typical high-symmetry cubic structures present in the majority of the magnetic transition metal alloys show a low magnetocrystalline anisotropy, reducing the anisotropy field of the possible magnet. However, certain transition metal compounds form in the tetragonal $L1_0$ structure, which is characterized by high uniaxial magnetocrystalline anisotropy that could raise the anisotropy of the compounds.

The $L1_0$-structure (space group P4/*mmm* or AuCu I structure) consists of alternating layers of two different constituent elements, parallel to the tetragonal c-axis, creating a natural superlattice. The tetragonal distortion of this phase along the c-axis is responsible for the high magnetocrystalline anisotropy of the system, typically in the range $K_1 \sim 10^6$-10^7 J/m^3.

This chemically ordered structure is formed from the disordered face-central-cubic (fcc)-A1 structure through a disorder-order transformation. The precursor phase A1 is a cubic structure where the occupation of a given atomic site by either of the two component elements is equal. In contrast, in the $L1_0$-structure each crystallite size has a different probability of being occupied by the two atoms types. The *A* atoms occupy the 1a (0,0,0) positions, while the *B* atoms occupy the 1d (½, ½, ½) positions. A1 and $L1_0$ structures are represented in Figure 5.

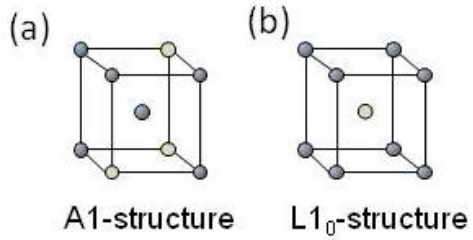

Figure 5. Schematic representation of disorder fcc A1-structure (a) and ordered tetragonal $L1_0$-structure (b). In the A1 structure, the two different components occupied random positions, while in the $L1_0$ structure the position of each element is well defined.

The $L1_0$-structure has been theoretically reported in different compounds such FePt, FeNi or MnAl. This structure eases to maintain the large magnetization of its constituents and, at the same time, provides them with large mangnetocrystalline anisotropy, making these compounds very promising alternatives to substitute the RE-PMs.

1.3.2.2 $L1_0$-FePt

The tetragonal chemically ordered $L1_0$ phase provides the FePt with strong magnetic properties. In this system, the high magnetization comes from the Fe. Opposite to the hexaferrites, the $L1_0$ FePt does not present any second Fe-sublattice that could be coupled antiferromagnetically with the principal lattice, easing to reach a M_s close to the saturation achieved in $Nd_2Fe_{14}B$ (1.43 vs 1.6 T) [35].

The $L1_0$ promotes a huge magnetocrystalline anisotropy in the system (K_1= 6.6 MJ/m^3) and the system possess ultrahigh coercivity in sub-10 nm size nanocrystals [36] [37], so the FePt is a great promise for permanent magnets and also for magnetic memories devices. In addition to the magnetic properties, the FePt is more ductile than the RE-PMs and chemical inert.

The$L1_0$-ordered FePt phase can be obtained by different approaches, but the most typical process is by a heat treatment of the disordered A1 FePt (fcc structure) precursor [38] [39]. The A1 FePt phase can be stabilized at room temperature by quenching from high temperatures [40] [41].

As it is shown in Figure 6, the $L1_0$ structure is only obtained when there are a nearly equal number of Fe and Pt atoms (35-55% Pt). In $Fe_{100-x}Pt_x$ alloys deviating from $35 < x < 55$ stoichiometry, the $L1_0$ is not obtained, and it is formed the stable cubic superstructures $L1_2$ with the composition $FePt_3$ (if $x>55$) and Fe_3Pt (if $x<35$).

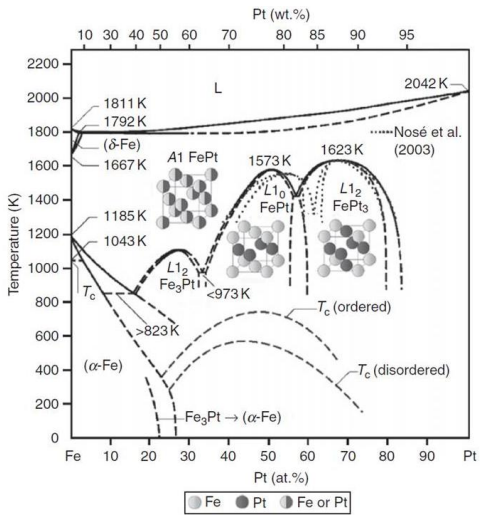

Figure 6. Phase diagram of the Fe-Pt system made by Lyubina et al. [38]. Crystallographic structures of the A1, $L1_0$ and $L1_2$ phases are shown in their corresponding equilibrium regions.

The Fe_3Pt ordered in a $L1_2$ structure presents a higher magnetization than the $L1_0$ FePt structure (1.8 vs 1.43 T) [42], but the absence of anisotropy constant in the $L1_2$ makes impossible to use it as a permanent magnet. However, an optimal exchange coupling of FePt-Fe_3Pt nanocomposites reaches the $(BH)_{max}$ up to 54 MGOe, reported by Liu et al. [43]. In the other case, if x>55, the $FePt_3$ ordered in a $L1_2$ structure has a paramagnetic response [44].

Despite the promising magnetic properties of the $L1_0$ FePt, the high price of Pt limits its use to very specialized low volume applications such as in magnetic micro-electromechanical systems, magnetic MEMS, or in aggressive environments as in dentistry.

1.3.2.3 $L1_0$-FeNi

The $L1_0$-FeNi or Tetrataenite is one of the most promising alternatives. The tetraenite is an ordered alloy containing equiatomic Fe and Ni, and it was observed for the first time in 2010 by the Institute Geophysics and Planetary Physics at UCLA, when John T. Wasson was analyzing some meteorites [45]. The lattice structure for the $L1_0$-FeNi is a chemically ordered fct superstructure with alternating monatomic layers of Fe and Ni along the c-axis [46]. As the magnetization comes from the ferromagnetic coupling between the Fe-Fe and Ni-Ni atoms, the long range order is extremely important. Furthermore, the magnetic anisotropy constant is also correlated with the long-range order parameter (S). For these two reasons, the formation of high S-$L1_0$ FeNi is essential to obtain a material that could be use as a permanent magnet.

It has been reported that the $L1_0$ structure is formed by an extraordinarily slow diffusion at the order-disorder transition temperature 593 K from the disorder fcc A1 structure [46]. The tetrataenite reported from meteorites was formed by a cooling rate of just 5 K per million years for the temperature interval of 973 K to 623 K [47]. Therefore, the challenge with the tetranite is the artificial synthesis of the $L1_0$ in the lab. The most significant advances in this direction have been done on the shape if thin films [48]. Other approaches aiming to develop the $L1_0$-FeNi phase, such as melt-spinning [49] have ended with a maximum volume fraction of only ~13 wt%.

The low diffusion of Fe and Ni makes harder the formation of the phase by the use of conventional annealing techniques. Goto et al. took a novel approach to synthesize the tetraenite by nitrogen insertion [46]. First of all, the FeNiN, which has the same order arrangement than the tetrataenite, is formed

by nitriding A1-FeNi powder with ammonia gas. Subsequently, FeNiN is denitrided by topotactic reaction to remain just FeNi maintaining the a- and c-constant, obtaining therefore the $L1_0$ structure (Figure 7).

There are a lot of efforts on the synthesis of the tetrataenite due to its high theoretical magnetic properties. The tetrataenite has a M_s estimated of 15.7 kG and an anisotropy constant of 1.3 MJ/m^3 [50], and it is expected a $(BH)_{max}$ of 56 MGOe [51], even higher than the actual magnets. However, the synthesis of the phase is not even the main problem; the biggest challenge is the production of a textured fully dense bulk magnet at a temperature lower than the order-disorder temperature (593 K).

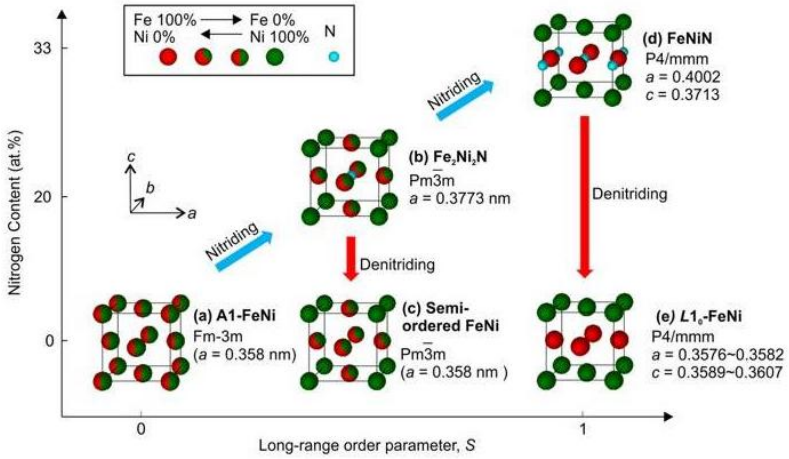

Figure 7. Conceptual diagram for fabrication path of ordered FeNi alloys by NITE method Models of crystal lattices for (a) A1-FeNi, (b) Fe_2Ni_2N (c) semi-ordered FeNi, (d) FeNiN, and (e) $L1_0$-FeNi are depicted with Fe (red), Ni (green), and N (light blue) atoms. Atoms identified by red and green indicate that Fe and Ni are randomly arranged according to the ratios of coloured areas. Face-centred cubic (FCC) structures are depicted as a basis for comparison, although unit cells are individually different [46].

1.3.2.4 $L1_0$-MnAl

The MnAl, as the other alternatives explained before, only presents one ferromagnetic phase, the $L1_0$ phase. Tetragonal $L1_0$ phase in the MnAl was discovered in the late 1950s by Kono and Koch [52] [53]. The ferromagnetic phase of the MnAl presents a theoretical magnetic moment of 2.37-2.40 μm/f.u., which would result in a M_s of 165 emu/g [54] [55]. Nonetheless, it has been reported that the system may also present antiferromagnetism, decreasing the saturation of the system [56].Unlike the previous materials where the optimal stoichiometry in the $L1_0$structure was 50-50, The $L1_0$ structure in the MnAl is stable if the percentage of Mn is the range of 50-58, obtaining the most sable structure when this value is 55 [57]. In a 50-50 case, the Mn atoms should occupy the (0,0,0) sites, and the Al the (½, ½, ½) sites; but the excess of Mn causes that some Mn atoms occupy the "not-desired" (½, ½, ½) sites, ordering antiferromagnetically with the rest of Mn atoms. The Mn situated in the "wrong" position decrease the total magnetization of the unit cell. The highest experimentally saturation magnetization measured is 112 emu/g in a $Mn_{51}Al_{49}$ sample, measured at room temperature [58].

This material presents a strong magnetocrystalline anisotropy of 1.7 MJ/m^3[59], superior than other alternatives like FeNi; and a Curie temperature of T_C= 650 K [59], superior to that of the NdFeB magnets. According to its intrinsic properties and using its theoretical density of 5.16 g/cm^3, the $L1_0$-MnAl presents a theoretical $(BH)_{max}$ of 12.6 MGOe [54].

Provided successful development of permanent magnet properties in MnAl system, these magnets will be able of competing with low-grade RE-PMs, while being above the maximum values and temperature range operation of ferrites and more expensive RE-free PMs (Alnico and PtCo alloys). Moreover, MnAl –based PMs are lighter than RE-PMs (MnAl is one-third times lighter than NdFeB), which will make them suitable for applications with space constrain and issues. The $L1_0$-MnAl also presents high resistance to corrosion and a cheap cost of the constitution elements, making it a strong alternative in front of the actual magnets.

The mechanical and magnetic properties of the MnAl and the low cost of its constitutional elements make the MnAl one of the most promising alternatives for the next decade. While some of the new composites are still in the basic research, the formation of $L1_0$-MnAl is already possible. The improvement of

its magnetic properties could open a new era in the permanent magnets with low-intermediate energy product.

1.4 System under investigaction: MnAl(C)

The MnAl is ferromagnetic when the Mn and the Al are ordered in the tetragonal $L1_0$ structure, which is a metastable structure in this composite. The improvement of the magnetic properties in the MnAl goes through the understanding of the MnAl system and the characteristics of each phase that can be formed.

1.4.1 Phase diagram of MnAl

The understanding of possible structures in the MnAl compound can only be reached by studying its phase diagram. The general form of the phase diagram was established in 1940 using DTA techniques. This diagram was improved in further investigations by specific heat and structure analysis. Liu et al. did the last change in 1996 [60], during their research on the stability of the high temperature phases. Figure 8 shows the optimized phase diagram of the Al-Mn system, reported by Shukla and Pelton in 2008 [61].

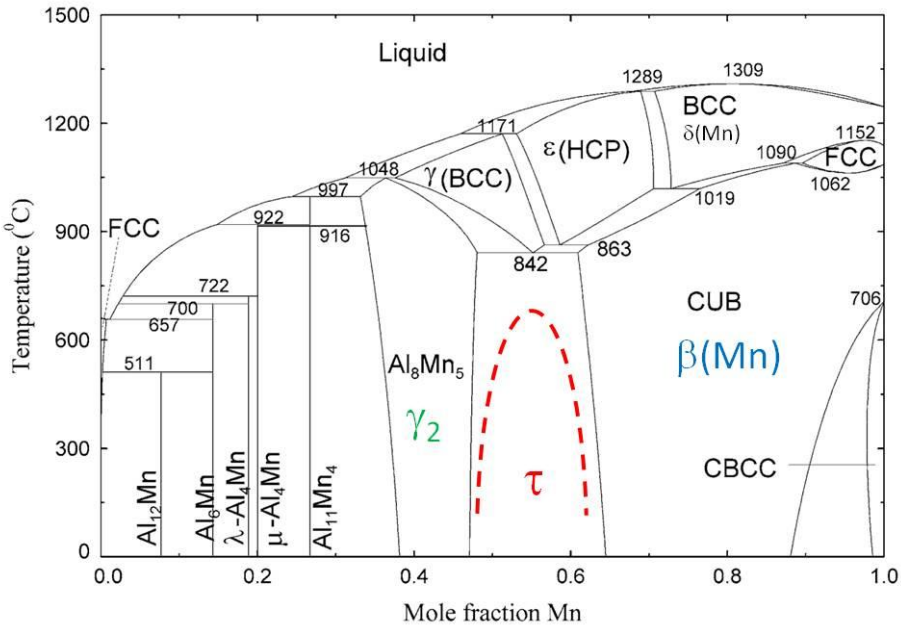

Figure 8. Phase diagram of the MnAl [61]. In color, the ferromagnetic τ ($L1_0$)-phase (red) and the possible decomposition phases of the τ-phase: the β- (blue) and the γ_2- (green) phases.

The phase diagram shows several solid solution phases, attending on the percentage of Mn. The only ferromagnetic phase in this diagram is the $L1_0$ structure, the metastable τ-phase (Figure 8). Surrounding the τ-phase, another 5 phases can be detected. These phases can be classified according to the temperature at which they crystallize: the room-temperature phases γ_2- and β(Mn)-; and the high temperature γ-, ε- and δ(Mn)- phases. The high temperature phases will decompose into the RT-phases, and they only can be maintaining at room temperature through a quenching.

The τ-phase is a metastable composition that is only possible to achieve if the percentage of Mn is between 50 and 58, as reported by Kono and Koch, [61]. The ferromagnetism of the Mn atoms is due to the distance between them. It is necessary a separation of 2.96 Å (or more) to change the antiferromagnetism coupling of the Mn atoms to a ferromagnetic one [62] [63]. The orientation of the magnetic moments is aligned along the c-axis of the tetragonal structure, so the anisotropy of the system is also along this axis. The formation of the τ-phase is only possible from the high-temperature ε-phase. This transformation will be explained in the following section.

τ-phase is a metastable phase, which means that it can decompose in other phases with higher stability. The possible decomposition of the τ-phase is into the γ_2- and β-phases. Both phases are non-ferromagnetic, and the high stability of each one avoids the recrystallization of the τ-phase once they have been already formed.

Al_8Mn_5 or γ_2-phase is a rombohedral R3m structure that can be formed when the Mn content is 31-48 at. % of the sample [64]. γ_2-phase is non-ferromagnetic because the Mn atoms are coupling antiferromagnetic in the structure. γ_2-phase is formed by cooling of the γ-phase, which is formed only at temperatures above 800 ºC. However, this structure can be formed from the ε-phase by two eutectoid reactions (i.e. $\varepsilon \rightarrow \gamma + \beta$-Mn and $\gamma \rightarrow \gamma_2$) if the content of Mn is superior to 52 at % [61] [64], or just by a reversible reaction from γ if the content of Mn is lower than the 52 at %.

The other possible phase that can be obtained from the decomposition of the τ-phase is the β-phase. β-phase is actually β(Mn)-phase, because it is a pure Mn phase, where the Al is presented inside the Mn-structure [65]. β-Mn is a paramagnetic cubic phase which can be formed from the hexagonal MnAl-ε phase by a massive transformation or from the δ-Mn phase, attending on the initial composition of the material [55] [60]. As the ε- and δ- phases are high

temperatures phases, the transformation mentioned before occurs at temperatures lower than 850 ºC [60]. If the atomic percentage of Mn is superior to 50%, β(Mn)-phase is also the most stable phase of the RT-phases, which means that the amorphous MnAl powder presented in the sample will recrystallite in this non-ferromagnetic phase [61].

The high temperature γ- and δ(Mn)- phases are both base-central-cubic (BCC) structures, where the main difference between them is the ratio of the elements. γ- is an Al-structure, and δ is a Mn-structure [60]. Both phases are only crystallized at temperatures above 850 ºC, and they need a stoichiometric composition away of the $Mn_{50}Al_{50}$. As the aim of this thesis has been the studio of the permanent magnets properties of the MnAl(C), which comes from the τ-phase, the stoiciometry and the temperatures used in the experiments were chosen in order to made impossible the formation of these two phases. Thus, ε-phase will be the only high temperature phase observed in the studied samples.

The ε-phase is a hexagonal HCP structure that is formed at temperatures higher than 900 ºC. Slow cooling of the system at 2 ºC/min avoids retaining the phase at room temperature, resulting in the formation of a mixture of the three RT γ_2- β- and τ-phases. However, it has been reported DONDE that it is possible to retain this phase by quenching at velocity superior to 600 ºC/min. If the ε-phase has been quenched; the annealing of this structure will transform the ε-phase into τ-phase or into a mixture of γ_2 and β-phase, attending on the annealing temperature.

1.4.2 Mechanism behind the ε to τ-MnAl phase transformation

The formation of the $L1_0$ τ-MnAl phase is necessary to obtain permanent magnetic properties in the material. As it has been explained before, the τ-phase is a metastable phase that cannot be formed from amorphous powder, being only possible to form this phase by a transformation from its precursor, the ε-phase.

The transformation of this phase has been extensively studied. The initial studies indicated that the transformation could occur through a displacive or marensitic transformation following metastable B19 ordering within the hcp phase ($\varepsilon \rightarrow \varepsilon' \rightarrow \tau$) [66] [67]. However, following studies by optical and

electronic microscopy and kinetic analyses have indicated that the formation of the τ-phases involves two steps: nucleation and growth process.

The nucleation process occurs following the model of Plitcha et al. [68]. In this model, the nucleation occurs when the coherent/semicoherent boundary energy is less than or equal to one-half the grain-boundary energy. This means that possible defects in the ε-grains will nucleate at lower temperature than the grains without any damage; and it indicate also that the nucleation of the τ-phase starts in the grain boundaries, as it was proved by Soffa et al [69].

In the second step, the growth process transforms the rest of the ε-phase into τ-phase. The growth process is described as a massive transformation, where the annealing temperature is critical in the velocity of the process. A higher annealing temperature reduces the time needed to transform all the ε-phase into τ-phase.

As the ε-phase is a high-temperature phase that can be quenched to retain the phase at room temperature, the mechanism explained above can take place in two different ways.

If the material is at a temperature above 900 ºC (i.e. the ε-phase is the most stable phase), one possible way to transform the phase is by a controlled cooling of the MnAl sample from 900 ºC to room temperature, at a velocity of 10 ºC/min [63] [69]. In this case, the cooling rate is critical in the phase transformation, a slower cooling causes the degradation of the τ-phase in the not desired γ_2- and β-phase [70]. Using this procedure, the possible defects in the grains or any induced strain in the particles are eliminated, reducing the coercivity of the system.

On the other hand, if the ε-phase has been quenched and the sample is at room temperature, the transformation will take place through a heat treatment. An annealing process will transform the ε-phase into τ-phase. If in the previous case the cooling rate was critical, the most important parameter in this method is the annealing temperature. A too low annealing temperature does not achieve any modification of the structure, and a too high annealing temperature cause a degradation of the powder into the non-ferromagnetic γ_2- and β-phase. Furthermore, the optimal temperature for the transformation is not the same in all MnAl samples. The optimal annealing temperature varies, between other reasons, attending on the presence or absence of carbon, normally used to stabilize the τ-phase. It has been reported that carbon

increases the onset temperature of the ε→τ transformation [71]. For that reason, DSC measurements of the ε-phase samples are very useful to determine the optimal annealing temperature for them.

1.4.4 State of the art of the MnAl system

The good intrinsic properties of the MnAl has attracted the attention of numerous scientific groups during the last years, making the research of the $L1_0$ structure in the MnAl system one of the most promising lines worldwide. While the formation of the τ has been achieved by different non-equilibrium processing techniques such as arc melting [63] [72] [73] [74], drop-synthesis [59], melt spinning [75] [76] [77] and gas-atomization [78], the maximization of its magnetic properties (high magnetization and high coercivity) is still a challenge.

The research of the τ-phase can be divided into two main groups: Study of the formation of the ferromagnetic τ-phase with high magnetic saturation and improvement of the coercivity in the τ-MnAl system.

The studies of the maximization of the magnetic saturation of the MnAl(C) focus their attention in the optimization of the magnetic moment of the Mn in the $L1_0$ structure, trying to remove the antiferromagnetic coupling between some Mn atoms by doping the system with a third element or optimizing the MnAl composition. In this line, the use of C has been proved as an excellent candidate to increase the stability of the phase and, at the same time, raise the saturation of the system [67] [71] [72] [79]. The C is introduced in the (½, ½, ½) sites, avoiding the antiferromagnetic coupling between the Mn. Fang et al. reported how the addition of C in the MnAl structure eases to increase their saturation from 88 to 110 emu/g [59]; and Wei et al. also reported a high saturation magnetization of 125 emu/g by the doping the MnAl system with C [74]. However, these works reported samples with a low value of coercive field, below 1 kOe, making them not suitable for PM applications.

Bittner et al. [80] reported that the coercivity of the τ-phase is different attending on the way that it has been obtained: direct transformation from ε-phase by quenching produces τ-phase with a really low coercivity (<0.4 kOe) while the two-steps-process of ε-phase quenching and subsequent annealing can produce τ-phase powder with a coercivity between 1 and 1.5 kOe, still quite low for permanent magnets applications. Bittner et al. also explains in

their research that one of the most promising ways to increase the coercivity is by cold working of the MnAl powder, reporting H_c above 3 kOe.

The research of the improvement of the coercivity in the MnAl system by mechanical milling is the second main research mentioned before. It has been reported that is possible to raise the coercivity through microstructure refinement and induced strain in MnAl powder by ball-milling [63] [81]. The ball-milling process modifies the size and the shape of the particles, inducing also changes in the microstructure. With this technique, high coercive field values (H_c over 5 kOe) have been reported after several hours of milling. Fang et al. [59] and Zeng et al. [63] reached a Hc = 5.2 kOe after 4 and 8 h of milling, respectively, while similar coercivity values were obtained by Lu et al. for a milling time of above 20 h [73].

Despite the values reported in these works exceed the coercivities reported in papers with a high magnetization; their low magnetization avoids the use of these powders in permanent magnet applications. There is a compromise between the magnetization and the coercivity in the MnAl. It is necessary to obtain samples with a competitive coercivity without neglecting the remanence magnetization in order to use them as a permanent magnet.

In addition to the necessity to find a compromise between M_r and H_c, it is also necessary to reduce the milling time needed to nanostructure the material. First, to avoid undesired relaxation effects and undesired phase transformation processes due to the high temperatures achieved during long milling times and, second, in view of industrial implementation, to develop a process economically viable.

Bibliography

[1] Soshin Chikazumi and Chad D Graham. *Physics of Ferromagnetism 2e*. Number 94. Oxford University Press on Demand, 2009.

[2] JMD Coey. Permanent magnets: Plugging the gap. *Scripta Materialia*, 67(6):524–529, 2012.

[3] John MD Coey. *Magnetism and magnetic materials*. Cambridge university press, 2010.

[4] Bernard Dennis Cullity and Chad D Graham. *Introduction to magnetic materials*. John Wiley & Sons, 2011.

[5] Edmund Clifton Stoner and EP Wohlfarth. A mechanism of magnetic hysteresis in heterogeneous alloys. *Philosophical Transactions of the Royal Society of London. Series A, Mathematical and Physical Sciences*, 240(826):599–642, 1948.

[6] Thomas Schrefl, Josef Fidler, and H Kronmüller. Remanence and coercivity in isotropic nanocrystalline permanent magnets. *Physical Review B*, 49(9):6100, 1994.

[7] Sustainable Energy. Magnet Energy. http://www.magnetnrg.com/pm history.html.

[8] Gowin Knight. Iii. a letter from gowin knight, mb to the president; concerning the poles of magnets being variously placed. *Philosophical Transactions of the Royal Society of London*, 43(476):361–363, 1745.

[9] T Mishima. Nickel-aluminum steel for permanent magnets. *Ohm*, 19:353, 1932.

[10] TO Paine, LI Mendelsohn, and FE Luborsky. Fine-particle magnets. *Electrical Engineering*, 76(10):851–857, 1957.

[11] Alex Hubert and Rudolf Schäfer. *Magnetic domains: the analysis of magnetic microstructures*. Springer Science & Business Media, 2008.

[12] JJ Went and GW Rathenau. Gorter, gw v. oosterhout. *Philips Techn. Rev*, 13:194, 1952.

[13] Koichi Haneda and Hiroshi Kojima. Intrinsic coercivity of substituted bafe12o19. *Japanese Journal of Applied Physics*, 12(3):355, 1973.

[14] Amitabh Verma, OP Pandey, and Puneet Sharma. Strontium ferrite permanent magnet-an overview. 2000.

[15] Karl Strnat, G Hoffer, J Olson, W Ostertag, and JJ Becker. A family of new cobalt-base permanent magnet materials. *Journal of Applied Physics*, 38(3):1001–1002, 1967.

[16] J Ping Liu, Eric Fullerton, Oliver Gutfleisch, and David J Sellmyer. *Nanoscale magnetic materials and applications*, volume 10. Springer, 2009.

[17] KHJ Buschow. Magnetism and processing of permanent magnet materials. *Handbook of magnetic materials*, 10:463–593, 1997.

[18] K Strnat. The hard-magnetic properties of rare earth-transition metal alloys. *IEEE Transactions on Magnetics*, 8(3):511–516, 1972.

[19] C. Chen G. C. Hadjipanayis J. Zhou, R. Skomski and D. J. Sellmyer. Smâ€“coâ€“cuâ€“ti high-temperature permanent magnets. *Appl. Phys. Lett*, 77:1514, 2000.

[20] F. JimÃ©nez-Villacorta L.H. Lewis. Perspectives on permanent magnetic materials for energy conversion and power generation. *Metallurgical and Materials Transactions A*, 44:220, 2013.

[21] John Michael David Coey. *Rare-earth iron permanent magnets*. Number 54. Oxford University Press, 1996.

[22] FJ Cadieu. Recent advances in pseudobinary iron based permanent magnets. *International materials reviews*, 40(4):137–148, 1995.

[23] John J Croat. High coercivity rare earth-iron magnets, January 29 1985. US Patent 4,496,395.

[24] Yutaka Matsuura, Masato Sagawa, and Setsuo Fujimura. Process for producing permanent magnet materials, July 1 1986. US Patent 4,597,938.

[25] Norman C Koon. Hard magnetic alloys of a transition metal and lanthanide, September 6 1983. US Patent 4,402,770.

[26] JF Herbst. R 2 fe 14 b materials: Intrinsic properties and technological aspects. *Reviews of Modern Physics*, 63(4):819, 1991.

[27] Oliver Gutfleisch. Controlling the properties of high energy density permanent magnetic materials by different processing routes. *Journal of Physics D: Applied Physics*, 33(17):R157, 2000.

[28] S Liu and GE Kuhl. Development of new high temperature and high performance permanent magnet materials. Technical report, DAYTON UNIV OH RESEARCH INST, 2000.

[29] ZW Liu, RV Ramanujan, and HA Davies. Improved thermal stability of hard magnetic properties in rapidly solidified re–tm–b alloys. *Journal of Materials Research*, 23(10):2733–2742, 2008.

[30] Raja K Mishra. Microstructure of hot-pressed and die-upset ndfeb magnets. *Journal of applied physics*, 62(3):967–971, 1987.

[31] Steven Chu. *Critical materials strategy*. DIANE Publishing, 2011.

[32] Global Industry Analysts. Nutraceuticals: A global strategic business report, 2010.

[33] Robert C Pullar. Hexagonal ferrites: a review of the synthesis, properties and applications of hexaferrite ceramics. *Progress in Materials Science*, 57(7):1191–1334, 2012.

[34] Jun Cui, Matt Kramer, Lin Zhou, Fei Liu, Alexander Gabay, George Hadjipanayis, Balamurugan Balasubramanian, and David Sellmyer. Current progress and future challenges in rare-earth-free permanent magnets. *Acta Materialia*, 2018.

[35] David J Sellmyer and Ralph Skomski. *Advanced magnetic nanostructures*. Springer Science & Business Media, 2006.

[36] Narayan Poudyal, Girija S Chaubey, Vikas Nandwana, Chuan-bing Rong, Kazuaki Yano, and J Ping Liu. Synthesis of fept nanorods and nanowires by a facile method. *Nanotechnology*, 19(35):355601, 2008.

[37] Shouheng Sun. Recent advances in chemical synthesis, self-assembly, and applications of fept nanoparticles. *Advanced Materials*, 18(4):393–403, 2006.

[38] J Lyubina, B Rellinghaus, O Gutfleisch, and M Albrecht. Structure and magnetic properties of l10-ordered fe–pt alloys and nanoparticles. In *Handbook of magnetic materials*, volume 19, pages 291–407. Elsevier, 2011.

[39] Kevin Elkins, Daren Li, Narayan Poudyal, Vikas Nandwana, Zhiqiang Jin, Kanghua Chen, and J Ping Liu. Monodisperse face-centred tetragonal fept nanoparticles with giant coercivity. *Journal of Physics D: Applied Physics*, 38(14):2306, 2005.

[40] LM Magat, GV Ivanova, LV Solina, NN Shchegoleva, and Ya S Shur. Coercive force and structure of an fe-pt alloy. *FIZIKA METALLOV METALLOVEDENIE*, 29(2):400–403, 1970.

[41] AY Yermakov and VV Maykov. Magnetic-properties of quick-quenched ordering copt and fept base alloys. *FIZIKA METALLOV I METALLOVEDENIE*, 60(4):747–750, 1985.

[42] AZ Menshikov and YU Dorofeev. Magnetic structure of ordered fe-pt alloys. *Fizika Metallov Metallovedenie*, 38(3):505–518, 1974.

[43] Yi Liu, Thomas A George, Ralph Skomski, and David J Sellmyer. Aligned and exchange-coupled fept-based films. *Applied Physics Letters*, 99(17):172504, 2011.

[44] S Maat, O Hellwig, G Zeltzer, Eric E Fullerton, GJ Mankey, ML Crow, and JL Robertson. Antiferromagnetic structure of fept 3 films studied by neutron scattering. *Physical review B*, 63(13):134426, 2001.

[45] John T Wasson. Relationship between iron-meteorite composition and size: Compositional distribution of irons from north africa. *Geochimica et Cosmochimica Acta*, 75(7):1757–1772, 2011.

[46] Sho Goto, Hiroaki Kura, Eiji Watanabe, Yasushi Hayashi, Hideto Yanagihara, Yusuke Shimada, Masaki Mizuguchi, Koki Takanashi, and Eiji Kita. Synthesis of single-phase l 1 0-feni magnet powder by nitrogen insertion and topotactic extraction. *Scientific reports*, 7(1):13216, 2017.

[47] KB Reuter, David B Williams, and JI Goldstein. Determination of the fe- ni phase diagram below 400 c. *Metallurgical Transactions A*, 20(4):719–725, 1989.

[48] T Shima, M Okamura, S Mitani, and K Takanashi. Structure and magnetic properties for l10-ordered feni films prepared by alternate monatomic layer deposition. *Journal of Magnetism and Magnetic Materials*, 310(2):2213–2214, 2007.

[49] Akihiro Makino, Parmanand Sharma, Kazuhisa Sato, Akira Takeuchi, Yan Zhang, and Kana Takenaka. Artificially produced rare-earth free cosmic magnet. *Scientific reports*, 5:16627, 2015.

[50] Louis Néel, J Pauleve, R Pauthenet, J Laugier, and D Dautreppe. Magnetic properties of an ironâ€"nickel single crystal ordered by neutron bombardment. *Journal of Applied Physics*, 35(3):873–876, 1964.

[51] A Mubarok, N Bordeaux, E Poirier, FE Pinkerton, J Gattacceca, P Rochette, R Reisener, LH Lewis, and JI Goldstein. Microstructural and magnetic characterization of the nwa 6259 iron meteorite. *Meteoritics and Planetary Science Supplement*, 76, 2013.

[52] Hiroshi Kono. On the ferromagnetic phase in manganese-aluminum system. *Journal of the Physical Society of Japan*, 13(12):1444–1451, 1958.

[53] AJJ Koch, P Hokkeling, MG vd Steeg, and KJ De Vos. New material for permanent magnets on a base of mn and al. *Journal of Applied Physics*, 31(5):S75–S77, 1960.

[54] JH Park, YK Hong, S Bae, JJ Lee, J Jalli, GS Abo, N Neveu, SG Kim, CJ Choi, and JG Lee. Saturation magnetization and crystalline anisotropy calculations for mnal permanent magnet. *Journal of Applied Physics*, 107(9):09A731, 2010.

[55] Akimasa Sakuma. Electronic structure and magnetocrystalline anisotropy energy of mnal. *Journal of the Physical Society of Japan*, 63(4):1422–1428, 1994.

[56] Alexander Edström, Jonathan Chico, Adam Jakobsson, Anders Bergman, and Jan Rusz. Electronic structure and magnetic properties of l 1 0 binary alloys. *Physical Review B*, 90(1):014402, 2014.

[57] Ch Muller, HH Stadelmaier, B Reinsch, and G Petzow. Metallurgy of the magnetic tau-phase in mn-al and mn-al-c. *Zeitschrift fuer Metallkunde*, 87(7):594–597, 1996.

[58] L Pareti, F Bolzoni, F Leccabue, and AE Ermakov. Magnetic anisotropy of mnal and mnalc permanent magnet materials. *Journal of applied physics*, 59(11):3824–3828, 1986.

[59] Hailiang Fang, Sofia Kontos, Jonas Ångström, Johan Cedervall, Peter Svedlindh, Klas Gunnarsson, and Martin Sahlberg. Directly obtained τ-phase

mnal, a high performance magnetic material for permanent magnets. *Journal of Solid State Chemistry*, 237:300–306, 2016.

[60] XJ Liu, R Kainuma, H Ohtani, and K Ishida. Phase equilibria in the mn-rich portion of the binary system mnî—¸ al. *Journal of alloys and compounds*, 235(2):256–261, 1996.

[61] Adarsh Shukla and Arthur D Pelton. Thermodynamic assessment of the al-mn and mg-al-mn systems. *Journal of phase equilibria and diffusion*, 30(1):28–39, 2009.

[62] MA Bohlmann, JC Koo, and JH Wise. Mn-al-c for permanent magnets. *Journal of Applied Physics*, 52(3):2542–2543, 1981.

[63] Q Zeng, I Baker, JB Cui, and ZC Yan. Structural and magnetic properties of nanostructured mn–al–c magnetic materials. *Journal of Magnetism and Magnetic Materials*, 308(2):214–226, 2007.

[64] M Ellner. The structure of the high-temperature phase mnal (h) and the displacive transformation from mnal (h) into mn 5 al 8. *Metallurgical Transactions A*, 21(6):1669–1672, 1990.

[65] Vladimir Sliwko, Peter Mohn, and Karlheinz Schwarz. The electronic and magnetic structures of alpha-and beta-manganese. *Journal of Physics: Condensed Matter*, 6(32):6557, 1994.

[66] JJ Van Den Broek, H Donkersloot, G Van Tendeloo, and J Van Landuyt. Phase transformations in pure and carbon-doped al45mn55 alloys. *Acta Metallurgica*, 27(9):1497–1504, 1979.

[67] T Ohtani, N Kato, S Kojima, K Kojima, Y Sakamoto, I Konno, M Tsukahara, and T Kubo. Magnetic properties of mn-al-c permanent magnet alloys. *IEEE Transactions on Magnetics*, 13(5):1328–1330, 1977.

[68] MR Plichta, WAT Clark, and HI Aaronson. The nucleation kinetics, crystallography, and mechanism of the massive transformation. *Metallurgical Transactions A*, 15(3):427–435, 1984.

[69] C Yanar, JMK Wiezorek, WA Soffa, and V Radmilovic. Massive transformation and the formation of the ferromagnetic l1 0 phase in manganese-aluminum-based alloys. *Metallurgical and Materials Transactions A*, 33(8):2413–2423, 2002.

[70] Hailiang Fang, Johan Cedervall, Francisco Javier Martinez Casado, Zdenek Matej, Jozef Bednarcik, Jonas Ångström, Pedro Berastegui, and Martin Sahlberg. Insights into formation and stability of τ-mnalzx (z= c and b). *Journal of Alloys and Compounds*, 692:198–203, 2017.

[71] Ping-Zhan Si, Hui-Dong Qian, Chul-Jin Choi, Jihoon Park, and Hong-Liang Ge. A novel method for measuring the phase transformation temperature and enhanced coercivity in cold-rolled mnalcx (x= 0–5) alloys. *Journal of Magnetism and Magnetic Materials*, 451:540–545, 2018.

[72] ZW Liu, C Chen, ZG Zheng, BH Tan, and Raju V Ramanujan. Phase transitions and hard magnetic properties for rapidly solidified mnal alloys doped with c, b, and rare earth elements. *Journal of Materials Science*, 47(5):2333–2338, 2012.

[73] Wei Lu, Junchao Niu, Taolei Wang, Kada Xia, Zhen Xiang, Yiming Song, Hong Zhang, Satoru Yoshimura, and Hitoshi Saito. Low-energy mechanically milled τ-phase mnal alloys with high coercivity and magnetization. *Journal of Alloys and Compounds*, 675:163–167, 2016.

[74] JZ Wei, ZG Song, YB Yang, SQ Liu, HL Du, JZ Han, D Zhou, CS Wang, YC Yang, A Franz, et al. τ-mnal with high coercivity and saturation magnetization. *AIP Advances*, 4(12):127113, 2014.

[75] I Janotová, P Švec Sr, P Švec, I MatÊ¼ko, D Janickovic, J Zigo, M Mihalkovic, J Marcin, and I Škorvánek. Phase analysis and structure of rapidly quenched al-mn systems. *Journal of Alloys and Compounds*, 707:137–141, 2017.

[76] I Janotová, P Švec Sr, P Švec, I Mat'ko, D Janickovic, B Kunca, J Marcin, and I Škorvánek. Formation of magnetic phases in rapidly quenched mn-based systems. *Journal of Alloys and Compounds*, 749:128–133, 2018.

[77] Zhen Xiang, Xiao Wang, Yiming Song, Lunzhou Yu, Erbiao Cui, Baiwen Deng, Dan Batalu, and Wei Lu. Effect of cooling rates on the microstructure and magnetic properties of mnal permanent magnetic alloys. *Journal of Magnetism and Magnetic Materials*, 475:479–483, 2019.

[78] Anurag Chaturvedi, Rumana Yaqub, and Ian Baker. Microstructure and magnetic properties of bulk nanocrystalline mnal. *Metals*, 4(1):20–27, 2014.

[79] Florent Calvayrac, Anna Bajorek, Nirina Randrianantoandro, et al. Mechanical alloying and theoretical studies of mnal (c) magnets. *Journal of Magnetism and Magnetic Materials*, 462:96–104, 2018.

[80] F Bittner, J Freudenberger, L Schultz, and TG Woodcock. The impact of dislocations on coercivity in l10-mnal. *Journal of Alloys and Compounds*, 704:528–536, 2017.

[81] Luke G Marshall, Ian J McDonald, and LH Lewis. Quantification of the strain-induced promotion of τ-mnal via cryogenic milling. *Journal of Magnetism and Magnetic Materials*, 404:215–220, 2016.

Chapter 2

2.Experimental details

2.1 Material synthesis: Gas atomization

The need to crystallize non-equilibrium phases (ε- and τ- phase) in the MnAl powders makes necessary to carry out a rapid solidification process to produce the desired alloy. The term *rapid solidification* is applied to a solidification from the melt, where there is a short-time interval between initiation and completion of solidification which facilitates the preservation of the non-equilibrium phases produced at high temperature. The non-magnetic ε-phase is produced at high temperature (above 1273 K) and the rapid solidification process avoids the decomposition of the ε-phase into the non-magnetic phases β and γ_2. The techniques generally used to produce MnAl have been arc-melting [1] [73] [63] [74], drop-synthesis [70], melt spinning [75] [76] [77] and gas-atomization [78].

In this work, the powder used has been produced by gas-atomization process, this is a droplet method patented in 1872 by Marriot Huddersfield [10]. He designed a very simple atomizer where the metal stream falls onto a horizontal gas jet, producing the metal drops. This technique was first applied in the production of zinc powder. In 1920s, Professor Hall re-designed the gas-atomization process, patented a new instrument for the production of steel particles [11]. The basic design shown in his patent is still in use and has yet to be significantly improved. In the 1980s, the gas atomization technique was started to use to produce other metals like Titanium [12], and nowadays the gas-atomization it is a well-known method used in industry to produce a large number of different compounds.

In the actual design, the molten manganese steel is atomized thanks to a nozzle at high pressure, transforming the melting material into aerosol particles (Figure 1). The molten material breaks up to into spherical droplets as a result of surface tension. The atomizing media used to MnAl particles should be argon or nitrogen, to avoid oxidation.

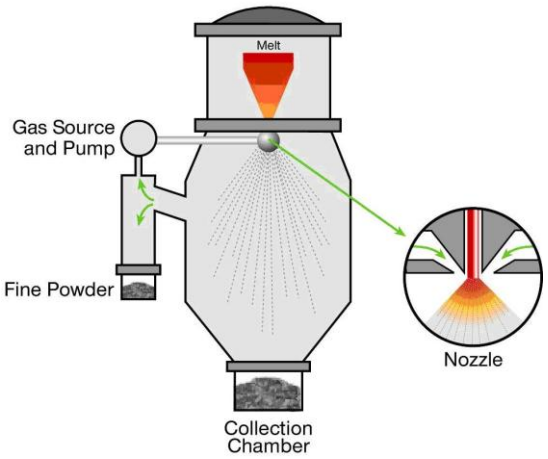

Figure 1. Diagram of the vertical gas atomization process [13].

The advantage of this process versus other rapid solidification process, such as melt spinning, is the control of the shape and the size of the particles. The control of the gas pressure, for example, facilitates the control of the yield of finer particle sizes [14].

The other main advantage of the gas atomization process is the scalability of the system. Laboratory atomizers produce less than 1kg per run, but there are commercial scale facilities with capacities up to 50.000 tons per year [15]. The study of the MnAl system with gas atomized particles could ease to scale the use of MnAl as a permanent magnet by the industry.

2.2 Micro- and nanostructuring of gas atomized powder: Planetary ball milling

Independently of the preparation method (gas-atomization, melt spinning, arc melting, etc) the as-prepared MnAl powder typically presents a coercivity below 2 kOe, a value too low for permanent magnet applications.

As already stated in the Introduction, the coercivity in magnetic samples can be improved by introducing defects or modifications in its structure. As the ball milling process is a technique that allows the modification of the morphology and the microstructure of the materials, it can improve the coercive field of the MnAl powder.

Therefore, the planetary ball mill is the most used alternative. In this system, the rotating pots are installed on the revolving disk, and the movement of the pots is opposite to that of the disk (Figure 2). The difference in speeds between the balls and pots produces an interaction between frictional and impact forces, which releases high dynamic energies.

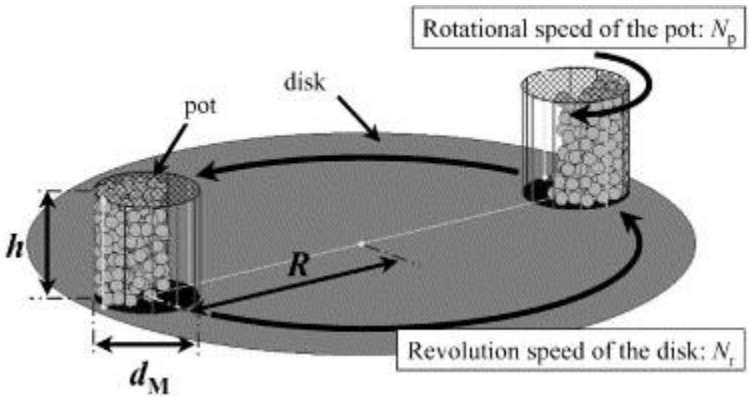

Figure 2. Schematic diagram of the planetary ball milling [16].

Due to the high dynamic energies of the method, the planetary ball milling is used for different applications: mechanical alloying, mechanical milling and mechanochemistry.

Mechanical alloying is a processing technique where high-energy ball milling is used to fracture and re-weld powder particles of different elements to produce a homogeneous material. Once that the homogeneity has been achieved, the desired structure in the material is obtained by a heat treatment of the amorphous powder resulting from the milling process.

In the 1980s, Schultz et al. [17] demonstrated that NdFeB magnets could be produced by mechanical alloying of its constituents elements Nd, Fe and B and a subsequent annealing of the amorphous phase obtained. Since then, this technique has been widely used to prepare a variety of alloys.

One direct descendant of the mechanical alloying is the mechanical milling. In this technique, the material is milled inside the planetary ball milling without reaching the level of amorfization achieved during the mechanical alloying. In this case, the material introduced is already crystallize, and the ball milling is only required to modify the morphology and the microstructure of the material, allowing to produce nanostructural changes in particles with an average size superior to 100 μm.

In chemistry, the use of mechanochemical processes in planetary ball mills is widely employed to synthesize both scientific and commercial materials. The advantage of using planetary ball mills instead of conventional chemical or processing routes is the reduction of the number of reagents, as well as higher yield. [16]

In this project research, the planetary ball milling has been used only for mechanical milling to modify the micro- and nanostructure of the MnAl gas-atomized particles in order to improve its permanent magnet properties.

Different authors have reported an increase in the coercivity of the MnAl powder after the ball milling process [73] [63] [81] [19] [20] [21], and the milling time needed in each experiment ranges from 1h [21] to more than 20h [73].

In this work, it has been done a breakthrough in the milling time typically used to improve the coercivity in the MnAl powder. It has been used a high rotational speed of the disk of 900 rpm, what allows to have a high impact energy during the milling. Additionally, it has been generally used tungsten carbide (ρ=15.8 g/cm^3) vials, in front of the typically vials made with steel (ρ=15.8 g/cm^3). The use of a milling media made with a high-density material increases the impact energy of the balls into the powders. The use of this system, where a high rotational speed combined with a milling media made with a high-density material, allowing the modification of the microstructure of the particles in less than 5 minutes of milling.

This short milling time has been explored recently in a variety of rare earth free permanent magnets material such a Co-ferrite and Sr-ferrite, obtaining an increment of the coercivity in less than 20 minutes of ball milling [22]. Following the previous experiments performed with ferrites, the diameter of the balls used has been 1.6 mm, and the mass-to-powder ratio has been 40:1.

In order to mitigate the oxidation and reduce the formation of aggregates during the milling process, the powders were surfactant-assisted milled. The surfactant used was oleic acid, with a powder-to-oleic acid ratio of 5:1.

2.3 Structural characterization

2.3.1 Differential scanning calorimetry (DSC)

The nucleation of the τ-phase from the ε-phase increases the heat flow energy of the MnAl system, which can be observed in a DSC measurement. It is possible, therefore, to optimize the annealing temperature of different milled powders by analyzing the temperature at which the τ-phase transformation peak is observed in DSC experiments.

The crystallographic transition has been determined using a TA Instrument model SDT Q600 with a maximum operation temperature of 1473 K. Measurements were performed by a annealing under a N_2 flow of 100 mL/min from room temperature to 973 K, using a temperature ramp of 10 K/min.

In order to perform the measurements 10 milligrams of MnAl powder were introduced inside a small cylindrical pan, placed inside the equipment, and close to a reference empty pan. The emission difference between both of them during the simultaneous annealing allowed the measurement of the powder heat flow energy. When the transformation of the ε-phase into the τ-phase in the MnAl particles starts, the heat flow energy of the sample increases and one peak is observed in the DSC measurement. The onset of the τ-formation is defined as the intersection of the tangent of the peak with the extrapolated baseline.

2.3.2 Electron microscopy

2.3.2.1 Scanning electron microscopy (SEM)

The morphology characterization of the as-atomized and milled MnAl powder was performed by Scanning electron microscopy, using a Zeiss-Evo scanning electron microscope (SEM). Elemental analysis of the different samples was performed by Energy Dispersive X-ray Spectroscopy (EDX) technique.

The technician staff at IMDEA Nanociencia (Madrid, Spain) performed the SEM measurements. EDX analysis was carried out at the Institute of Physics IPSAS in Bratislava (Slovakia) with the assistance of Prof. Peter Svec and Dr. Peter Svec Jr.

2.3.2.2 Transmission Electron Microscopy (TEM)

Detailed structural analysis of the constituent phases in the MnAl powder was carried out by scanning transmission electron microscopy (STEM) using a probe corrected FEI Titan Themis 300 operated at 200 kV. The HAADF (High Angle Annular Dark Field) detector collection angles were fixed to 136-200 mrad. This equipment is located at the Institute of Physics IPSAS, in Bratislava, measurements were carried out by Dr. Peter Svec Jr.

2.3.3 X-ray diffraction

The analysis of crystallographic structures in the MnAl powder has been performed using an X-Ray Diffractometer (XRD), X'Pert PRO Theta/2Theta Panalytical, with Cu-K(alpha)radiation.

Constructive interference between X-rays diffracted by a crystalline material is obseved when the Bragg´s law is fulfilled. The Bragg´s law or Bragg condition is:

$$2dsin\theta = n \qquad (1)$$

Where d is the interplanar spacing of the crystal lattice corresponding to a family of planes given by the (hkl) Miller indices, θ is the angle between the incident beam and the (hkl) planes, n is a positive integer and λ is the wavelength of the radiation (λ_{Cu}= 1.54060 Å) [23]

The position and the intensity of the peaks in the XRD data will provide information about the phases presented in the MnAl and their order; and the width and the shape of these peaks will provide information about the crystallite size and the internal stress of the different phases.

2.3.3.1 Interpretation of diffraction peaks and phase identification

The distance between the crystallographic planes *d* corresponding to a family planes given by the (hkl) Miller indices, can be determined by the equation:

$$d = \frac{a}{\sqrt{h^2+k^2+l^2}} \quad (2)$$

Where *a* is the lattice parameter of a particular crystallographic system and *h*, *k* and *l* are the different Miller indices.

Equation (2) proves that different crystallographic systems (i.e $a_1 \neq a_2$) could have the same d-spacing, satisfying the Bragg condition at identical angle. Being MnAl a polycrystalline material is then possible to observe overlaps of peaks in X-ray diffraction experiments

The position and the intensity of the experimental peaks have been compared with the standard reference patterns in order to determine the crystallographic structure related with each peak. The references patterns used during this thesis were obtained from the database of the "Interdepartmental Research Service (SIdI)" of the Universidad Autonoma de Madrid (Madrid).

2.3.3.2 Determination of the order parameter in MnAl(C)

A material composed by two types of atoms, A and B, is ordered when its A atoms arrange themselves in an orderly, periodic manner on one set of atomic sites, and the B atoms do likewise on another set. When this periodic arrangement of A and B atoms persists over large distances in the crystal, it is known as long-range order.

As magnetic properties in MnAl are exclusively due to ordered Mn atoms in the τ-phase (tetragonal $L1_0$ structure), it is necessary to have a high long-range order in the MnAl τ-phase to obtain a high magnetization.

Based on a theoretical ratio of $Mn_{50}Al_{50,}$ in the $L1_0$ structure there are 2 "average" atoms per unit cell; one of Mn and one of Al. Therefore, the atomic scattering factor of the "average" Mn-Al atom is given by

$$f_{av} = \frac{1}{2}f_{Mn} + \frac{1}{2}f_{Al} \quad (3)$$

As the structure factor is defined as $F = \sum f e^{2\pi i(hu+kv+lw)}$

In a complete disorder structure, there are 2 atoms per unit cell, at positions 0 0 0, and $\frac{1}{2}\frac{1}{2}\frac{1}{2}$. Therefore, the structure factor is given by

$$F = f_{av}\left[1 + e^{\pi i(h+k+l)}\right] \quad (4)$$

- $F = 2f_{av} = f_{Mn} + f_{Al}$ for $h+k+l$ even,
- $F = 0$ for $h+k+l$ odd.

On the other hand, in a complete order structure, each unit cell contains one Mn atom at 0 0 0, and one aluminum atom at $\frac{1}{2}\frac{1}{2}\frac{1}{2}$. The structural factor is then:

$$F = f_{Mn} + f_{Al}\left[e^{\pi i(h+k+l)}\right] \quad (5)$$

- $F = f_{Mn} + f_{Al}$ for $h+k+l$ even,
- $F = f_{Mn} - f_{Al}$ for $h+k+l$ odd.

The diffraction lines from planes where (h+k+l) is even are called *fundamental lines*, since they occur at the same positions and with the same intensities in the patterns of both ordered and disordered alloys. The extra lines which appear in the pattern of an ordered alloy, arising from planes where (h+k+l) is odd, are called *superlattice lines*, and their presence is direct evidence that ordering has taken place.

Structure factors of complete order and disorder cases can be combined as:

- $F_f = f_{Mn} + f_{Al}$ for $h+k+l$ even,
- $F_s = S(f_{Mn} - f_{Al})$ for $h+k+l$ odd.

Where **S** is defined as the order factor, and it is a natural value between 0 and 1.

Now, if we assume that the relative integrated intensities of a superlattice and fundamental line are given by their relative$|F^2|$, and we consider the scattering factor is equal to the atomic number (i.e f=Z); the relation between the intensity of the superlattice lines and the fundamental lines in a complete order (S=1) MnAl τ-phase is:

$$\frac{\text{Intensity superlattice line}}{\text{Intensity fundamental line}} \approx \frac{|F|_s^2}{|F|_f^2} = \frac{(25-13)^2}{(25+13)^2} \approx 0.1 \quad (6)$$

It means that, in a complete ordered MnAl structure, the intensity of the superlatice lines will be one-tenth of the intensity of the fundamental lines. This is the highest possible ratio between both lines. In the opposite case, when MnAl is in a complete disordered structure, the intensity of the superlattice lines would be 0 (S=0), and the ratio between the superlattice and the fundamental lines would be also 0.

Therefore, the order S of the τ-phase can be calculated from the relation between the intensity of superlattice and fundamental peaks; taking into account the ratio between the experimental data and the theoretical intensity of the peaks. As *S* is proportional to *F* and in consequence, to $\sqrt{I}$, the order factor S is

$$S=\sqrt{\frac{I_{superlattice}}{I_{fundamental}}}=\sqrt{\frac{I^{exp}_{superlattice}/I^{th}_{superlattice}}{I^{exp}_{fundamental}/I^{th}_{fundamental}}}=\sqrt{\frac{I^{exp}_{s}I^{th}_{f}}{I^{exp}_{f}I^{th}_{s}}} \quad (7)$$

Equation (7) has been used in this work to determine the order of the τ-phase structure in the different samples.

2.3.3.3 Rietveld analysis

There are several systematic errors that could cause a broadening of the peaks, and they will be the same in each measurement. The measuring instrument increases the width of the diffraction peaks due to the divergence of the beam and the broadening of the incident ration; and the measuring angle step can also increase the minimum width detectable, increasing therefore the broadening of the peaks. The highest systematic error in the XRD measurements presented in this work comes from the angle step, and it is 0.006 º.

In the material, the internal stresses and the grain size will determine the width of the peaks in the XRD measurement.

If the crystallite size becomes smaller, the diffracting plane of that phase also reduces, and it promotes an increase in the width of the peak. The effect of the grain size on the width can be calculated by the Scherrer's equation:

$$\Delta_{size}(2\theta) = \frac{k\lambda}{D\cos(\theta_B)} \quad (8)$$

Where $\Delta_{size}(2\theta)$ is the width of the peak (in radians), κ is a dimensionless shape factor, λ the wavelength, θ_B the Bragg angle and D the crystallite size. The shape factor is related to the line shape profile and can be considered as 0.89 for a Gaussian [24]. The width of the diffraction peak, $\Delta^{hkl}(2\theta)$, has been calculated by the width at half maximum.

On the other hand, increasing the internal stress,ε, causes a variation in the d-spacing, Δd, that will promote a broadening in the diffraction peak. By differentiating Bragg's law it can be shown that strain affects the peak in the following way:

$$\Delta_{strain}(2\theta) = 2tan(\theta_B) \quad (9)$$

The Williamson-Hall method [25] considers the width of the peak as a combination of the strain and the size effect. In this method, the combined effect is determined by a simple sum of each contribution, calculated by combining equation (8) and (9). Rearrangement of that sum gives:

$$\Delta^{hkl}(2\theta)\cos({\theta_B}^{hkl}) = \frac{\lambda}{D} + 2\varepsilon\sin(\theta^{hkl}) \quad (10)$$

Comparing the equation (10) with the standard equation for a straight line

$y = mx + c$

It is clear how by plotting $\Delta^{hkl}(2\theta)\cos({\theta_B}^{hkl})$ versus $sin(\theta^{hkl})$ it can be obtained the strain component from the slope (2) and the size component from the intercept ($\frac{\lambda}{D}$).

2.3.3.4 X-ray diffraction in temperature

The analysis of the crystallization temperature of the τ-phase performed by DSC measurements was completed by X-ray diffraction measurements in temperature. The in-situ evolution of crystallographic structures with increased temperature from room temperature to 773 K (500 ºC) with a ramp rate of 1 K/min was measured with a Bruker D8 Advance diffractometer with Cu-Ka radiation. The diffractometer was operated in grazing incidence mode

(incident anlge set to 10º) with parallel beam arrangement using a parallel Goebel mirror in the primary beam and a parallel plate collimator (0.35º) and a LiF monochromator to suppress the fluorescence arising from the presence of Mn in the diffracted beam. This allowed obtaining real-time temperature dependent XRD (T-XRD) maps.

2.3.4 Magnetic characterization: vibrating sample magnetometry

The magnetic characterization of the samples has been performed using a vibrating sample magnetometer (VSM). The working principle of VSM, invented by Simon Foner in 1959 [26], is based on Faraday's law of electromagnetic induction.

One sample is situated at the end of a rod, which is vibrating in a vertical direction, promoting an oscillatory movement in the sample. The vibrating sample is situated inside a coil system and between an electromagnet that, by applying a magnetic field, will magnetize the sample. The vibrating magnetic sample will induce an alternating voltage in the detection coils, which is compared with the alternating voltage induced by a reference permanent magnet. The difference between both voltages allows the determination of the magnetic moment of the sample.

The measurement of the samples is performed by the introduction of the powder inside a paramagnetic capsule, and cotton is added inside the capsule in tore to avoid the powder movement during the measurement. Once the powder and cotton are inside the capsule, it is situated at the end of the rod to initiate the measurement. As the VSM output signal is just the total magnetic signal of the sample, it is necessary to know the exact weight of the powder introduced inside the capsule to be able to calculate the magnetization per gram. The weight of the sample is performed before the introduction of the cotton in the capsules, on a high precision scale with a precision of 0.01 mg. The typical amount of powder used in each measurement is 15 mg.

Magnetic properties of the different samples were determined at room temperature using a LakeShore 7400 series VSM with a maximum applied magnetic field of 20 kOe. The calibration of the VSM was performed with a pure nickel sphere.

Bibliography

[1] ZW Liu, C Chen, ZG Zheng, BH Tan, and Raju V Ramanujan. Phase transitions and hard magnetic properties for rapidly solidified mnal alloys doped with c, b, and rare earth elements. *Journal of Materials Science*, 47(5):2333–2338, 2012.

[2] Wei Lu, Junchao Niu, Taolei Wang, Kada Xia, Zhen Xiang, Yiming Song, Hong Zhang, Satoru Yoshimura, and Hitoshi Saito. Low-energy mechanically milled τ-phase mnal alloys with high coercivity and magnetization. *Journal of Alloys and Compounds*, 675:163–167, 2016.

[3] Q Zeng, I Baker, JB Cui, and ZC Yan. Structural and magnetic properties of nanostructured mn–al–c magnetic materials. *Journal of Magnetism and Magnetic Materials*, 308(2):214–226, 2007.

[4] JZ Wei, ZG Song, YB Yang, SQ Liu, HL Du, JZ Han, D Zhou, CS Wang, YC Yang, A Franz, et al. τ-mnal with high coercivity and saturation magnetization. *AIP Advances*, 4(12):127113, 2014.

[5] Hailiang Fang, Johan Cedervall, Francisco Javier Martinez Casado, Zdenek Matej, Jozef Bednarcik, Jonas Ångström, Pedro Berastegui, and Martin Sahlberg. Insights into formation and stability of τ-mnalzx (z= c and b). *Journal of Alloys and Compounds*, 692:198–203, 2017.

[6] I Janotová, P Švec Sr, P Švec, I MatÊ¼ko, D Janickovic, J Zigo, M Mihalkovic, J Marcin, and I Škorvánek. Phase analysis and structure of rapidly quenched al-mn systems. *Journal of Alloys and Compounds*, 707:137–141, 2017.

[7] I Janotová, P Švec Sr, P Švec, I Mat'ko, D Janickovic, B Kunca, J Marcin, and I Škorvánek. Formation of magnetic phases in rapidly quenched mn-based systems. *Journal of Alloys and Compounds*, 749:128–133, 2018.

[8] Zhen Xiang, Xiao Wang, Yiming Song, Lunzhou Yu, Erbiao Cui, Baiwen Deng, Dan Batalu, and Wei Lu. Effect of cooling rates on the microstructure and magnetic properties of mnal permanent magnetic alloys. *Journal of Magnetism and Magnetic Materials*, 475:479–483, 2019.

[9] Anurag Chaturvedi, Rumana Yaqub, and Ian Baker. Microstructure and magnetic properties of bulk nanocrystalline mnal. *Metals*, 4(1):20–27, 2014.

[10] NA Yefimov and Stanislav Naboychenko. *Handbook of non-ferrous metal powders: technologies and applications*. Elsevier, 2009.

[11] Everett J Hall. Process for disintegrating metal, February 14 1928. US Patent 1,659,291.

[12] Pei Sun, Zhigang Zak Fang, Ying Zhang, and Yang Xia. Review of the methods for production of spherical ti and ti alloy powder. *Jom*, 69(10):1853–1860, 2017.

[13] https://www.carpenteradditive.com/technical-library/powder production/.

[14] IE Anderson. Boost in atomizer pressure shaves powder-particle size. *Advanced Materials & Processes*, 140(1):30–32, 1991.

[15] H Jones. Chapter 3, rapid solidification. *Non-equilibrium processing of materials. 1st ed. Amsterdam: Pergamon*, pages 23–45, 1999.

[16] Christine Friederike Burmeister and Arno Kwade. Process engineering with planetary ball mills. *Chemical Society Reviews*, 42(18):7660–7667, 2013.

[17] L Schultz, Jo Wecker, and E Hellstern. Formation and properties of ndfeb prepared by mechanical alloying and solid-state reaction. *Journal of applied physics*, 61(8):3583–3585, 1987.

[18] Luke G Marshall, Ian J McDonald, and LH Lewis. Quantification of the strain-induced promotion of τ-mnal via cryogenic milling. *Journal of Magnetism and Magnetic Materials*, 404:215–220, 2016.

[19] KP Su, XX Chen, HO Wang, DX Huo, and ZW Liu. Effect of milling on the structure and magnetic properties in mn54al46 flakes prepared by surfactant-assisted ball milling. *Materials Characterization*, 114:263–266, 2016.

[20] Shuang Zhao, Yuye Wu, Chi Zhang, Jingmin Wang, Zhongheng Fu, Ruifeng Zhang, and Chengbao Jiang. Stabilization of τ-phase in carbon-doped mnal magnetic alloys. *Journal of Alloys and Compounds*, 755:257–264, 2018.

[21] Michael Lucis, Timothy Prost, Xiujuan Jiang, Meiyu Wang, and Jeffrey Shield. Phase transitions in mechanically milled mn-al-c permanent magnets. *Metals*, 4(2):130–140, 2014.

[22] FJ Pedrosa, J Rial, KM Golasinski, M Rodrguez-Osorio, G Salas, D Granados, J Camarero, and A Bollero. Tunable nanocrystalline cofe 2 o 4 isotropic powders obtained by co-precipitation and ultrafast ball milling for permanent magnet applications. *RSC Advances*, 6(90):87282–87287, 2016.

[23] Leonid V Azároff and Raymond J Donahue. *Laboratory experiments in x-ray crystallography*. McGraw-Hill, 1969.

[24] AL Patterson. The scherrer formula for x-ray particle size determination. *Physical review*, 56(10):978, 1939.

[25] GK Williamson and WH Hall. X-ray line broadening from filed aluminium and wolfram. *Acta metallurgica*, 1(1):22–31, 1953.

[26] Simon Foner. Versatile and sensitive vibrating-sample magnetometer. *Review of Scientific Instruments*, 30(7):548–557, 1959.

Chapter 3

3. Nanostructuring and phase transformation by rapid-milling of gas-atomized MnAl powder

MnAl gas atomized powder has been nanostructured by ball milling technique and post-annealing treatment. In order to understand the nanostructuring process, different milling parameters, as the milling time or the impact energy, have been controlled during the milling process. Morphological, microstructural and magnetic characterizations of the different milled samples have been performed. The milling parameters and the post-annealing temperature have been optimized based on these different characterizations, improving the magnetic properties of the powder.

3.1 Influence of milling time in the short milling time regime

It has been reported in previous studies how the ball milling process can improve the magnetic properties of the MnAl system, raising the coercivity [63][81][3][59]. By comparison with the dozen hours that have been reported [73] [6], the fast-ball milling process used in this work can reduce the ball milling times from hours to unprecedented times below 5 minutes. The optimization of the milling time is critical in the development of the magnetic τ-phase. In this experiment, a rotation speed of 900 rpm has been used with tungsten carbide vials and balls, as well as ball-to-powder mass of 40:1. $Mn_{54}Al_{46}$ powders were milled by surfactant-assisted (oleic acid) mechanical milling, in order to reduce possible oxidation. The powder-to-oleic acid ratio used in this experiment was 5:1.

3.1.1 Morphological and microstructural properties

$Mn_{54}Al_{46}$ powder produced by gas-atomization under argon atmosphere has been used in this experiment as a starting material. As it can be observed in Figure 1 (a), the as-atomized powder consists on spherical particles with an average size of 3.5 (± 0.5) μm. XRD patterns of the starting gas-atomized MnAl particles (Figure 1 (b)) shows Bragg diffraction peaks of ε- and γ_2-phases, without any traces of the ferromagnetic τ-phase; which is in good agreement with previous works [6] [78] . Rietveld refinement indicates that the phase fraction of the starting powder is ~75 % ε-phase and ~25% of γ_2-phase. This amount of γ_2-phase presented in the starting material is formed during the gas-atomized process if the cooling is not fast enough [78]. The crystallite size determined from the XRD pattern for the ε-phase is 110 nm.

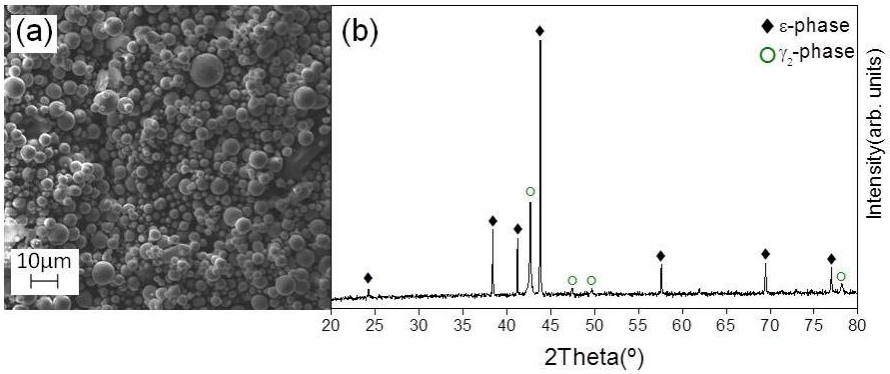

Figure 1. SEM image (a) and XRD data (b) of starting gas-atomized MnAl (scale bar: 10 μm)

In order to nanostructure the gas-atomized MnAl, the powder was milled using the fast ball-milling process; a well-known technique that can reduce the typically milling time of several hours to just a few minutes [22]. The high rotational speed and the ball to powder mass ratio used make possible to modify homogeneously the microstructure in minutes. The milling times used in this experiment have been 30, 90, 180 and 270 s. SEM images of the MnAl milled at the different milling times is represented in Figure 2.

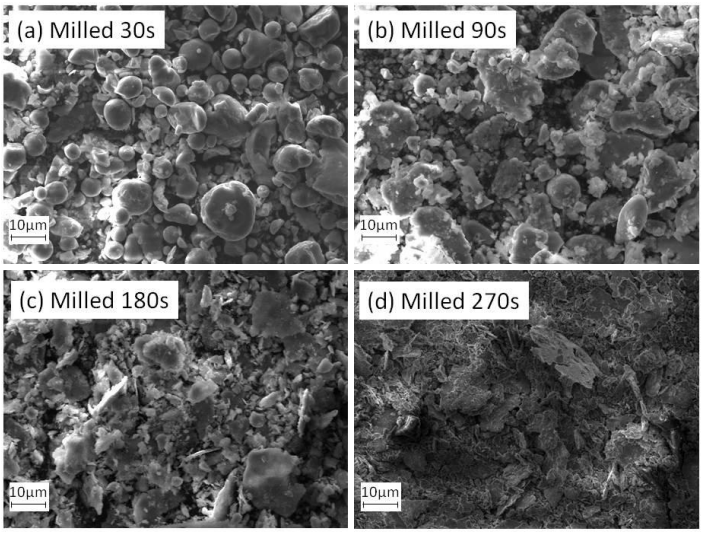

Figure 2. SEM images of the powder milled 30 (a), 90 (b), 180 (c) and 270 s (d). Scale bar: 10 μm

As it can be observed in Figure 2 (a), only 30 s of ball milling is sufficient to modify the morphology of the starting material (Figure 1 (a)). In this case, it is still discernible the original spherical shape of the particles, but there are some broken particles in the powder. The increment of milling time up to 90 s eases to destroy the initial spherical shape of the particles, obtaining a mixture of large and smaller particles (Figure 2 (b)). A milling time of 180 s changes the morphology of the particles, observing, in this case, flake-like shape particles, with the same mixture observed in the previous case (Figure 2 (c)). The increment of the milling time from 180 to 270 s promotes thinner particles, maintaining the average particle size of the powder milled 180 s (Figure 2 (d)).

In order to study the evolution of the microstructure with the milling time, XRD measurements of the different milled samples have been performed, which are represented in Figure 3.

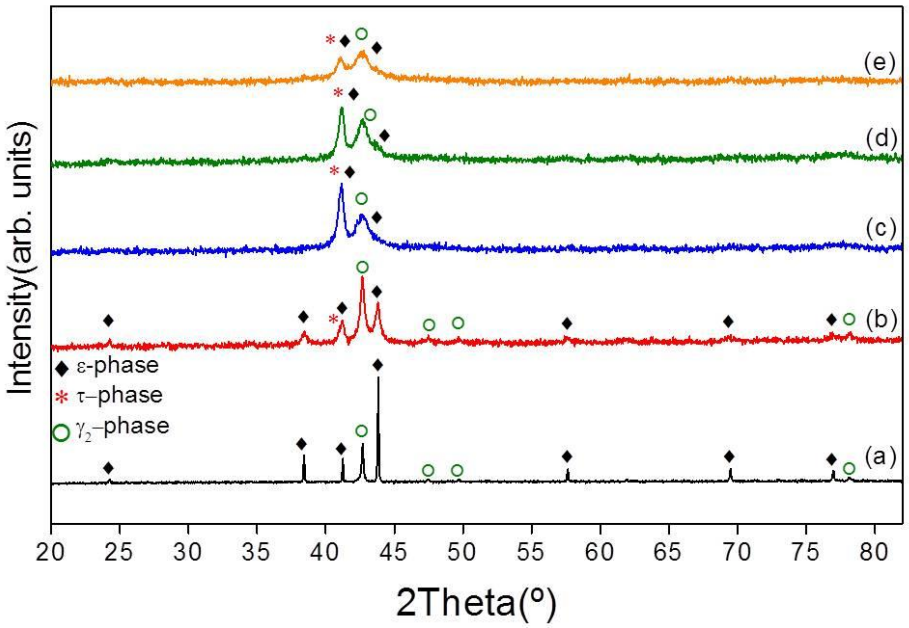

Figure 3. XRD patterns of the starting (gas-atomized) (a) and the samples milled for 30 (b), 90 (c), 180 (d) and 270 s (e).

The increment of milling time promotes broader peaks (Figure 3), which means that the milling process reduces the mean crystallite size of the ε-phase. It has been calculated by Scherrer method [9] how just 30 s of milling drastically reduces the crystallite size of the ε-phase from 110 nm to 17 nm. The increment of the milling time above 90 s promotes a reduction of the mean crystallite size under 10 nm. Longer milling times also promote a detriment in the peak intensity accompanying the broadening of the peaks, which means that an amorphization of the powder occurs during the milling process.

Apart of the ε- and γ_2-phases already present in the starting material, one peak of τ-phase is observed in the XRD patterns of the milled samples. The formation of the τ-phase means that the fast-milling process is able to transform the ε-phase into the ferromagnetic τ-phase without any heat treatment. Direct transformation of ε into τ was previously reported in cryomilled ribbons [81], but this is the first time that directly ε→τ transformation has been achieved during the ball milling, without any amount of τ-phase in the starting material. The formation of τ-phase could be explained as a consequence of the microstrain induced during the milling that

eases the ε-to-τ phase transformation through a displacive shear mechanism, as it has been reported before by Marshall et al [81].

The magnetic behavior of the milled samples has been proved by magnetic measurements (Figure 4), and it has been correlated with the XRD patterns.

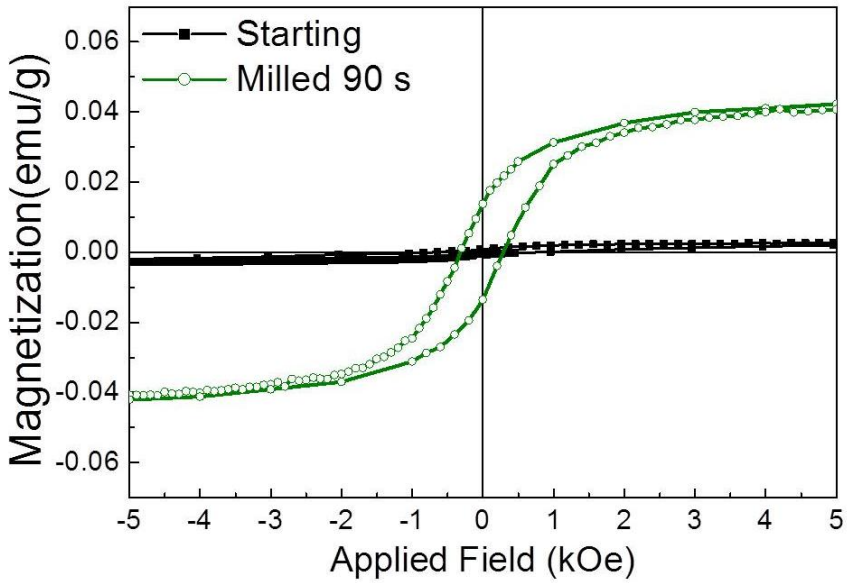

Figure 4. Hysteresis loops of the starting material and the samples milled for 30 and 270 s.

It is observed in Figure 4 how, after 90 s of milling, the material has a clearly small ferromagnetic response. This result can be perfectly correlated with the XRD measurements. The starting MnAl only presents ε- and γ_2- phase, so that the magnetic response only can be paramagnetic. After 90 s of ball milling process, a small peak of τ-phase is observed in the XRD patterns. This small amount of τ-phase is appreciated in the magnetic measurement, observing this small hysteresis loop.

Nevertheless, despite the partial transformation of ε- into the ferromagnetic τ-phase during the ball milling, a post-annealing treatment is needed to complete the transformation of the ε-phase into the τ-phase, developing the permanent magnet properties.

3.1.2 Optimization of the post-annealing temperature and magnetic characterization

The morphological and microstructural changes induced during the ball milling process, such as particles breakage and crystallite size reduction will most likely influence the temperature required to initiate the $\varepsilon \rightarrow \tau$ transformation. DSC analysis was performed to calculate the onset temperature of each sample. As-atomized and milled sample were annealed at 10 ºC/min up to XX in N_2 atmosphere. While the onset temperature is 415 ºC in the as-atomized material (Figure 5), the milling process reduces the onset temperature up to 375 ºC when the milling time is 30 s, and up to 370 ºC when the milling time is above 90 s. The refinement of the crystallite size reduces the thermal energy needed to initiate the transformation of the ε-phase into the ferromagnetic τ-phase, achieving therefore this reduction in the onset temperature in all the milled samples.

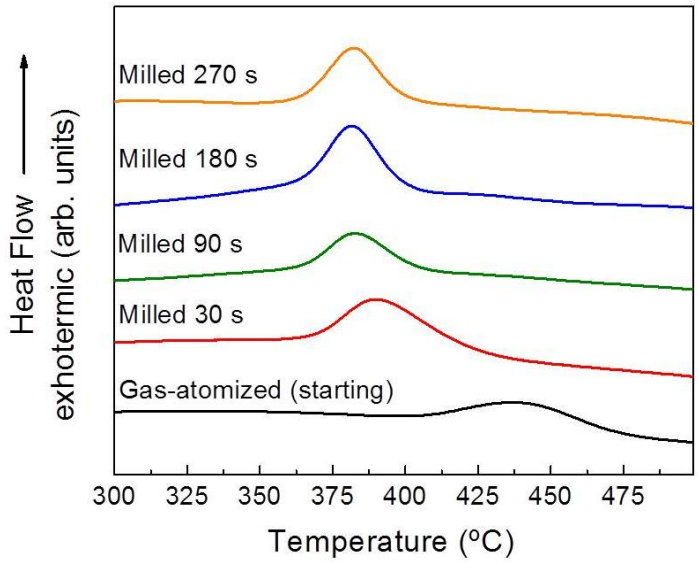

Figure 5. DSC measurements of the starting MnAl particles and the samples milled for 30, 90, 180 and 270s. Heating rate: 10 K/min.

In order to rule out the combined effect of milling followed by annealing from only those due to the annealing process, the as-milled powders and the starting gas-atomized particles have been annealed simultaneously in N_2 atmosphere at different temperatures, in the range of 340-450 ºC, during 10 min. Figures 6 (a), (b) and (c) show the XRD patterns of the samples annealed at the representative temperatures of 365, 400 and 450 ºC for 10 min, respectively.

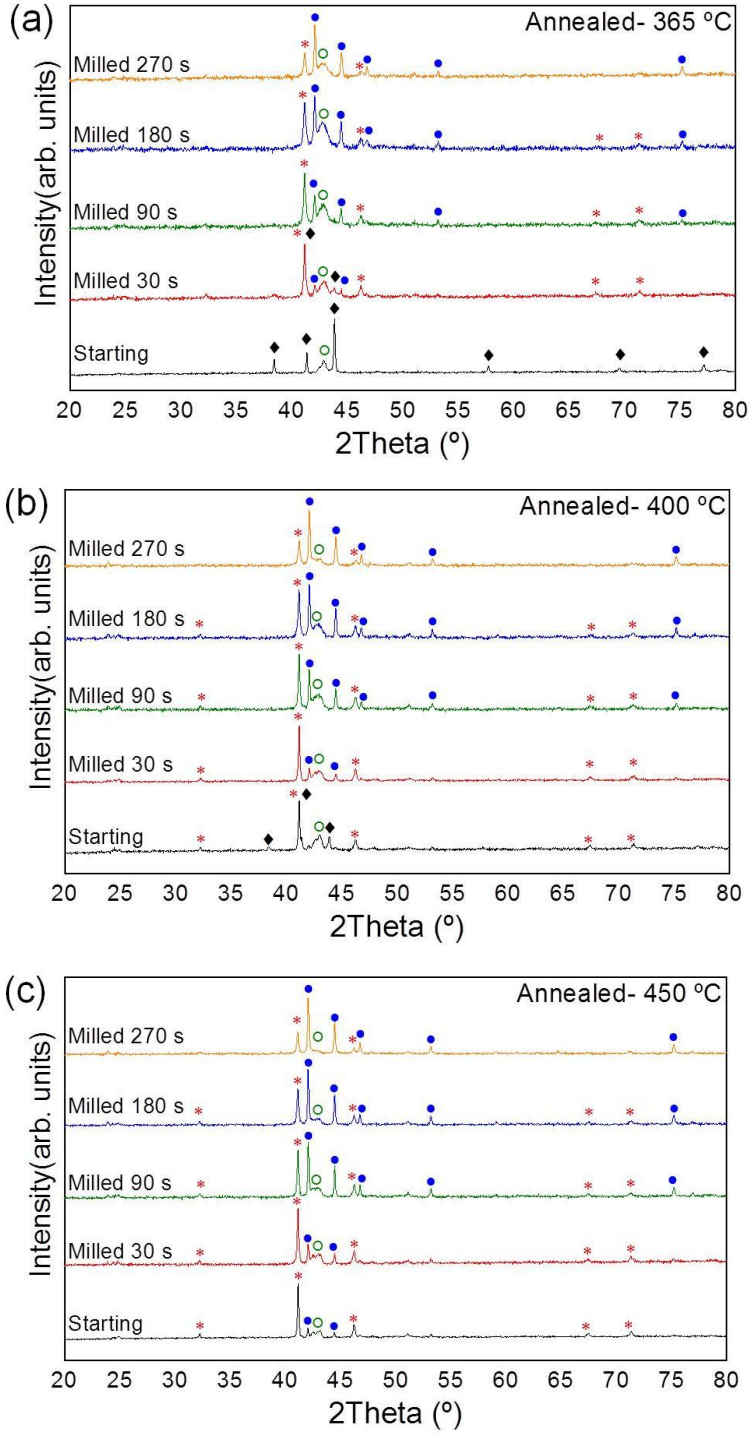

Figure 6. XRD patterns of the as-atomized and milled powder annealed at 365 ºC (a), 400 ºC (b) and 450 ºC (c). (♦) ε-phase, (*) τ-phase, (●) β-phase and (O) γ_2-phase

Heating of the starting material at 365 ºC is not enough to nucleate the ferromagnetic τ-phase (Figure 6 (a)). As it was explained before, the starting MnAl gas-atomized particles need a higher temperature to transform the ε-phase into τ-phase. On the other hand, this temperature is sufficient to form τ- and β- phase in the milled samples, in parallel to the dramatically decreased content of the ε-phase. The decrease in the crystallite size of the ε-phase during the milling eases the nucleation of the τ-phase at 365 ºC. The formation of the τ-phase during the annealing process is also accompanied by the formation of the non-magnetic β-phase. β-phase is more stable than the τ-phase [66] [11], and it is formed during the annealing process by the crystallization of the amorphous powder formed during the milling.

Based on the β/τ ratio (Figure 7 (a)) calculated using the reference intensity ratios (RIR) method [zhou2018xrd], the milled samples annealed at 365 ºC can be separated in two different regimes. Milling time as short as 30 s is sufficient to refine the crystallite size without beginning of amorphization, obtaining a high content of τ-phase after the heat treatment. As it can be observed in Figure 6 (a), the powder milled only for 30 s has less than 10% of β-phase content in the material. On the other hand, by increasing the milling time, it is observed a detriment in the content of τ-phase accompanied by an enhanced content of the β-phase, obtaining a β/τ ratio higher than 0.5 (Figure 7 (a)). Milling times above 30 s refine further the crystallite size of the ε-phase but also amorphize the material, that will recrystallize preferentially to the β-phase through subsequent annealing, i.e. reducing the overall fraction content of the τ-phase present in the samples, as it is shown in Figure 7 (a). As the samples milled the longest times promote the highest amount of amorphous powder, the sample milled 270s presents the highest β/τ ratio, above 2, after the heat treatment at 365 ºC.

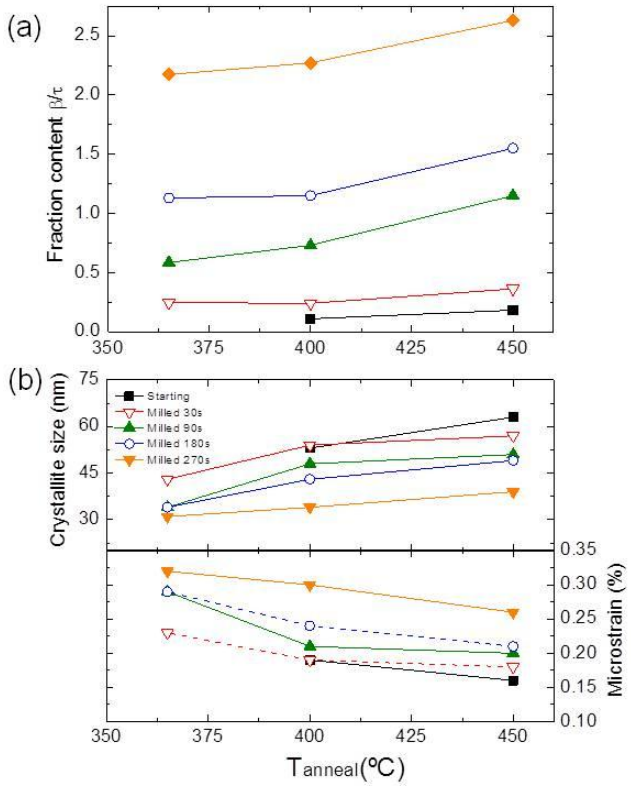

Figure 7. (a) β/τ ratio of the milled samples annealed at 375, 400 and 450 ºC. (b) Evolution of crystallite size and microstrain of the τ-phase with the annealing temperature for the different samples under study.

The increment of the annealing temperature up to 400 ºC allows the nucleation of the τ-phase in the as-atomized material (Figure 6 (b)). However, there is still a remanence of ε-phase in the powder, which indicates that it is necessary to anneal the starting material at higher temperature to obtain the full transformation of ε- into τ-phase. Heat treatment at 450 ºC is high enough to complete the formation of the τ-phase. The kinetics for phase transformation is shifted to higher temperatures compared to the as-milled powder due to the enlarged crystallite size (one magnitude larger) of the ε-phase in the starting material. This large crystallite size of the starting material promotes also a large crystallite size of the τ-phase (Figure 7 (b)). The powders milled longer times present a smaller crystallite size of the τ-phase, due to the reduction of the crystallite size of the ε-phase during the milling process.

Higher annealing temperature does not change the amount of the τ-phase in the milled samples (in both cases it has been produced a complete nucleation

of τ-phase), but the increment of the annealing temperature results in a larger crystallite size in all the samples (Figure 7 (b)).

By comparison between the XRD patterns of the milled samples annealed at different temperatures (Figure 6), it is observed that the increment of the annealing temperature raises the amount of β-phase in the samples. The increase in temperature helps to crystallize the amorphous powder formed during the milling process into the β-phase (Figure 6 (b-c)). As the amount of β-phase increases and the amount of τ-phase is constant, the ratio between both phases (β/τ) increases-with the temperature (Figure 7 (a)).

Figure 8 illustrates the effect of annealing at 365 ºC on the recorded hysteresis loops of the starting gas-atomized MnAl particles and the milled (30, 90, 180 and 270 s) powders. The first thing to note is the presence of a small ferromagnetic contribution to the hysteresis loop measured for the starting material after annealing. Considering that magnetization values are directly related to the content of the ferromagnetic τ-MnAl phase in the material, the ferromagnetic behavior can be explained as due to the presence of the τ-MnAl phase with an excessively low content to be detected by XRD (Figure 6). The development of a significant ferromagnetic hysteresis loop observed when going from this annealed starting material to the powders milled for 30 s and annealed, agree with the large increase in the τ-MnAl phase detected by XRD (Figure 6). Additionally, and also due to an increased content of the τ-MnAl phase, a large increase in magnetization takes place when going from the as-milled powder (Figure 3) to the milled and annealed powders (Figure 6). An increased milling time (from 30 s to 90 and 270 s) results in decreased values of M_{20kOe} and M_r due to a diminished content of the τ-phase in favor of crystallization of the β-phase during annealing (Figure 7(a)), as previously discussed from the corresponding XRD patterns (Figure 6 (a)). The development of permanent magnet properties achieved by milling and annealing includes also a significantly increased coercivity (Figure 8). The mechanisms influencing coercivity in the milled and annealed samples are diverse and will be discussed in detail in the following section, although the combination of the three effects can be already advanced: morphological changes (Figure 2), the microstrain induced during the milling process (Figure 7(b)) and the increased content of the stable β-phase (Figure 7(a)), that has been reported to result in pinning effects for magnetization reversal [78].

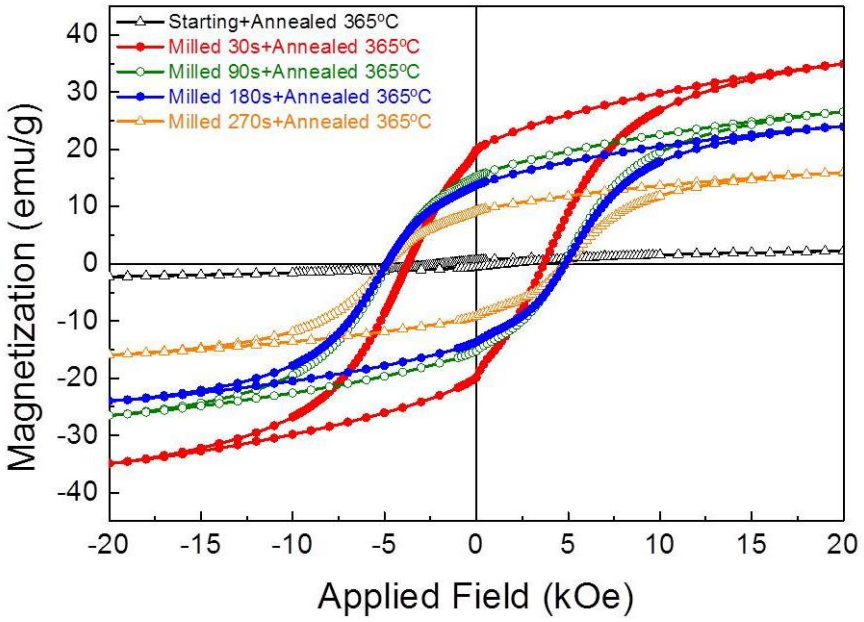

Figure 8. Hysteresis loops of the starting and milled samples annealed at 365 ºC during 10 min in N_2 atmosphere.

The evolution of $M_{20\ kOe}$, M_r and H_c of the starting material and the powders milled for 30, 90, 180 and 270 s with annealing temperature, T_{anneal}, is shown in Figure 9.

$M_{20\ kOe}$ and M_r follow the same tendency for each sample with increasing the annealing temperature (Figures 9 (a) and (b), respectively).

Magnetization is directly related to the content of the ferromagnetic τ-phase in the material and to its chemical order. The maximum applied field of 20 kOe used in this study is well below the 70 kOe reported in the literature to achieve saturation of the τ-phase [59] [74] [13] [14]. That is the reason why we will refer to M_{20kOe} instead of saturation magnetization, M_s.

It is clearly shown in Figure 9 an increase in magnetization measured for the milled powders with rising temperature up to 375 ºC, due to the increased content of the τ-phase. The increment of the temperature above 375 ºC leads practically to the stabilization of the magnetization values of the milled samples, in good agreement with the small variation of the content of the τ-phase for the annealed samples in the XRD measurements (Figure 6).

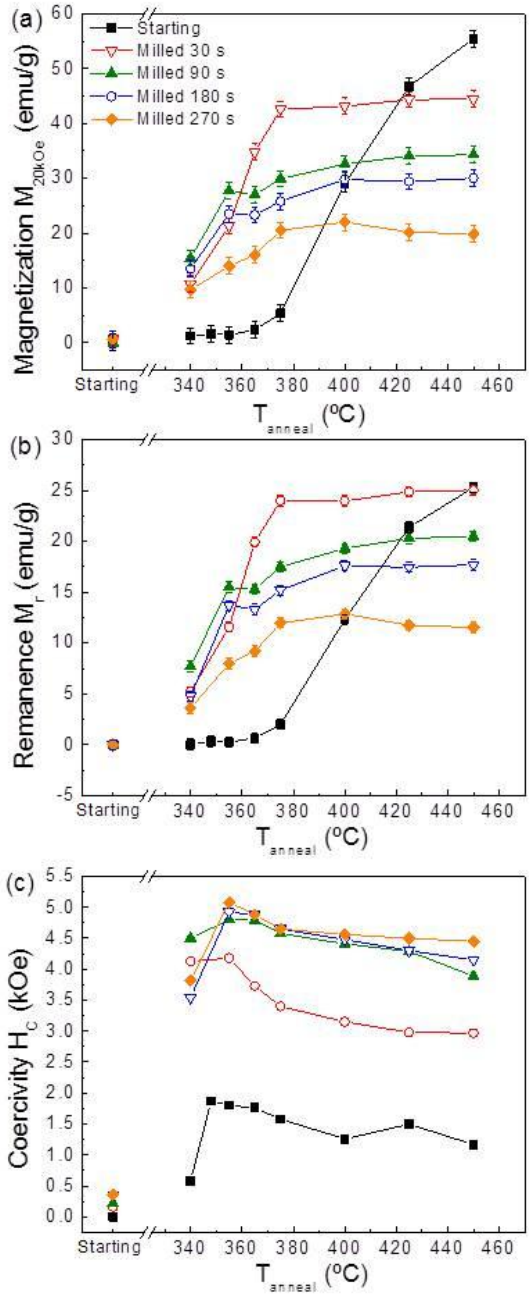

Figure 9. Evolution of the magnetization measured with a maximum applied field ok 20 kOe (a), remanence (b) and coercivity with the temperature for the as-atomized material and the milled powders.

On the other hand, the starting material presents a different evolution of the magnetization, without achieving an approximately constant regime. This is due to the retarded kinetics energy for the nucleation of the τ-phase, resulting from a larger crystallite size of the initial ε-phase (one order of magnitude larger than the milled powders). As the τ-phase is nucleated at higher temperature, the highest magnetization in the starting powder is obtained after the annealing at 450 ºC, thus 75 ºC higher than in the milled powders.

It is shown in Figure 9 (a) and (b) that powders milled longer times present lower magnetization M_{20kOe}. As the saturation magnetization is directly related with the amount of ordered τ-phase, the formation of the non-magnetic phase β during processing will be thus detrimental for the magnetization values. Apart from the amount of τ-phase in the samples, there is an added effect of using extended milling times, which is related to the chemical disorder in the as-milled powders. Determination of the long-range ordering parameter [9], S, of the τ-MnAl phase for milled samples after annealing at 450 ºC, and despite the reduced strain due to the relaxation effects induced by annealing, results in values of 0.93, 0.87, 0.86 and 0.83 for powder obtained from milling for 30, 90, 180 and 270 s, respectively. The decreased S values confirm the progressive degradation of the chemical order of the τ-phase with increasing the milling time, in good agreement with previous studies [81] [73]. The strain induced during the ball milling process in the powder results in an enhanced disorder and promotes Mn-Mn antiferromagnetic coupling, i.e. decrease in the net magnetic moment.

Evolution of coercivity, H_c, with annealing temperature is shown in Figure 9 (c). It is revealed that the sample with the lowest Hc value in the temperature range is the starting material, with Hc values below 2 kOe. Ball milling during 30 s eases an increase in coercivity of the powder up to 4.2 kOe, more than two times larger than the maximum Hc value obtained in the starting material. Powders annealed after increased milling times of 90, 180 and 270 s show a similar trend in coercivity, with the highest coercivity of 4.8, 4.9 and 5.1 kOe, respectively. These values are achieved after annealing the powders milled for 90 and 180 s at 365 ºC; and at 355 ºC the sample milled during 270 s. A coercive field above 5 kOe is one of the highest coercivities achieved in MnAl. Fang et al. [59] and Zeng et al. [63] reported a coercive field of 5.2 kOe, but the milling time used in their experiments was 4 and 8h, respectively. Similar coercive values were obtained by Lu et al. for a milling time above 20 h. [73]

Despite the mean crystallite size calculated for the τ-phase is well below the corresponding critical size for a single-domain size of about 710 nm [15]for all the powder under study, the particles are multidomain structure, due to their size (micrometer size) (Figure 2). As the structure is multidomain, the reversal magnetization process will consist of domain wall motion and wall pinning effect. The physical defects in the particles will act as pinning centers during magnetization reversal [80], blocking the propagation of the domains and raising the coercivity of the system. The density of physical defects increases with extended milling times. Increased milling times lead to reduced crystallite size and enlarged strain, the latter resulting in the increased density of defects. The microstrain is induced in the MnAl system during the ball milling and, despite the partial relaxation produced upon the annealing process; it is maintained to a certain extent (Figure 7 (b)). Samples milled longer times present higher microstrain and higher coercive values. As an example, annealing at 400 ºC of the starting non-milled particles and those milled for 270 s results in microstrains of 0.18 and 0.30, respectively. Apart of the pinning centers formed by the physical defects in the particles, it has been reported that the non-magnetic β-phase can act as pinning center during magnetization reversal [63] [81].

As it was explained before, β-phase is formed during the annealing process. An increase in the annealing temperature results in the augmented content of the β-phase; obtaining therefore a higher amount of pinning centers by increasing of the annealing temperature. Contrary to that, annealing of the as-milled powders leads to grain growth effects and strain relaxation (Figure 7 (b)) that will result in the decreased density of defects, i.e. a reduced number of pinning centers. Consequently, there is a counterbalance between the disappearance of defects due to relaxation in the annealing process and the increased content of the β-phase. This explains the moderate decrease in coercivity with increasing annealing temperature observed in Figure 9 (c) for samples milled for different durations. It is observed how the difference of 0.02% in the strain and the 10% of difference in the content of β-phase promote an important difference of more than 1.5 kOe between the coercivity of the starting material and the sample milled only 30 s. A remarkable increment from 4 kOe up to almost 5 kOe in the coercivity values is also observed between the samples milled 30 and 90 s, while for milling times above 90 s, the increase in coercivity after annealing is more moderate, less than 0.3 kOe. Longer milling times result in an increased amount of amorphous phase (Figure 3) that, through annealing, crystallizes to the stable β-phase (Figure 6). Thus, these samples show larger microstrain, above 0.2%

and a higher content of the β-phase (more than 40%) than the starting material and the sample milled 30 s, both beneficial in increasing coercivity through pinning effects.

3.2 Influence of varying the impact energy in the ball milling process

It has been explained how the ball milling process can raise the coercivity of the MnAl by the introduction of physical defects in the particles and the development of the non-magnetic β-phase. The formation of β-phase promotes a detriment in the magnetization [20], but it can raise the coercivity of the system [63].

The aim of this section is to discern the mechanism played by each phase in the evolution of the magnetic properties in MnAl. The optimization of the ratio between τ and β could facilitate to maximize the remanence magnetization and the coercivity at the same time.

It was explained in the previous section how the τ-phase is obtained from the nucleation of the ε-phase, and the β-phase is crystallized from the amorphous powder. As the amorphous powder is formed during the milling process, the control in the amount of the β-phase is achieved by the control of the impact energy during the milling process.

The energy transferred during the milling process is related with the kinetic energy of the balls, which is transferred to the powders during the collision, and with the total time of the milling process (longer milling time promotes more energy transferred).

To control the energy transferred, two milling media (i.e. balls and vessels materials used for milling) with different densities, ρ, were used. The dissimilarity in the density values of tungsten carbide ($\rho = 15.82 \times 10^3$ kg/m^3) and steel ($\rho = 7.64 \times 10^3$ kg/m^3) promotes a large difference in the kinetic energy of the balls during the ball milling.

If we consider the collision between the balls and the powder during the milling process as an inelastic collision, the energy transferred during the collision can be considered as:

$$E = \tfrac{1}{2} K_a m_b v_b^2 \qquad (1)$$

Where K_a is the constant describing the property collision (1) due to inelastic collision), m_b is the mass of the ball and v_b its velocity. This velocity is given by the expression:

$$v_b = K_b W_p R_p \quad (2)$$

Where K_b is a geometrical coefficient that can be considered as 1.06, due to the size of the balls (1.6 mm) [18]. W_p and R_p are the velocity and the radius of the milling system, respectively.

Substituting the values in equation (1), and considering a density of tungsten carbide and steel of 15.82 x 10^3 and 7.64 x 10^3 kg/m^3, respectively, the energies obtained are:

E (tungsten carbide media) = 8.3 x 10^4 Joule/collision.

E (steel media) = 4.0 x 10^4 Joule/ collision.

Consequently, the energy transferred to the powder during the collision when using tungsten carbide is about twice the value obtained when using steel. This result is of relevance to understanding the effect of using milling media with dissimilar densities on the microstructure and phase transformation of the material under study.

Gas atomized powders were milled, therefore, using steel and tungsten carbide media. The powder has been milled at two different durations, 90 and 270 s. In order to be systematic with the previous experiment, the same rotation speed of 900 rpm and the same ball-to-powder mass of 40:1 has been used in this work. In order to reduce possible oxidation, the experiment has been performed using oleic acid as surfactant-assisted. The powder-to-oleic acid ratio used in this experiment has been 5:1, as in the previous section.

3.2.1 Morphological and microstructural properties

$Mn_{54}Al_{46}$ gas atomized powder has been used in this experiment. As it is shown in the inset of Figure 10, the starting material consists on spherical particles with a size below 30 μm.

The XRD patterns of the as-atomized powder (Figure 10) show a lower content of γ_2 and higher content of ε-phase than in the previous experiment (Figure 1). ε-phase transforms into τ-phase during the annealing process, so that higher amount of ε-phase in the starting powder will promote higher

content of τ-phase in the non-milled powder after the annealing process, i.e. higher magnetization. The crystallite size of the ε-phase is 100 nm, in agreement with the previous section and with previous works [6].

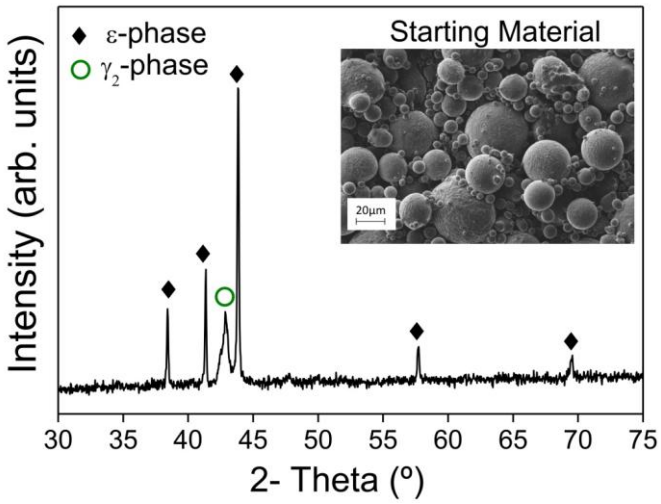

Figure 10. XRD characterization of the as-atomized $Mn_{54}Al_{46}$ starting particles. Inset: SEM images of the starting material. Scale bar: 20 μm.

As it can be observed in SEM images (Figure 11), the choice of the milling media has a straightway effect on the microstructure. Milling for 90 s using steel produces breakage in the particles, but the particles still maintain the initial mean particle size (Figure 11 (a)). An increment in the milling time up to 270 s promotes the reduction of the particle size and the formation of flatten particles (Figure 11 (b)).

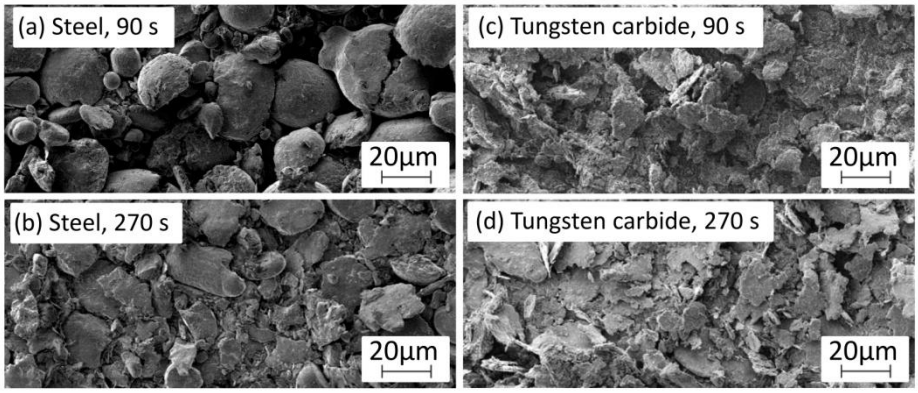

Figure 11. SEM images of milled MnAl particles using steel media for (a) 90 s and (b) 270 s; and tungsten carbide media for (c) 90 s and (d) 270 s. Scale bar: 20 μm.

By comparison, the use of tungsten carbide results in flake-like shape particles already after milling for only 90 s (Figure 11 (c) and (d)). The higher impact energy of the tungsten carbide balls eases this morphological transformation from spherical particles to thinner flake-like shape ones, reducing also the surface size below 15 μm.

As well as the morphological changes, the use of vials made with two different materials causes changes in the microstructure. Figure 12 shows the XRD patterns for the as-milled powder using steel and tungsten carbide media for 90 and 270 s. XRD pattern of the as-atomized powder is included in Figure 12 (a) for comparison. As it is shown in Figure 12 (a) and (b), the samples milled with steel present broader peaks, as it may be observed from the direct comparison done in Figure 12 (a), caused by the reduction of the crystallite size of the ε-phase. Milling with steel media during 90 s causes a reduction in the crystallite size of the ε-phase from 100 to 30 nm. The increment of the milling time up 270 s to promotes a reduction below 15 nm (Figure 12 (b)). Contrasting with the previous experiment, the use of steel does not introduce any new phase in the powder (i.e. only presence of ε and γ_2-phases).

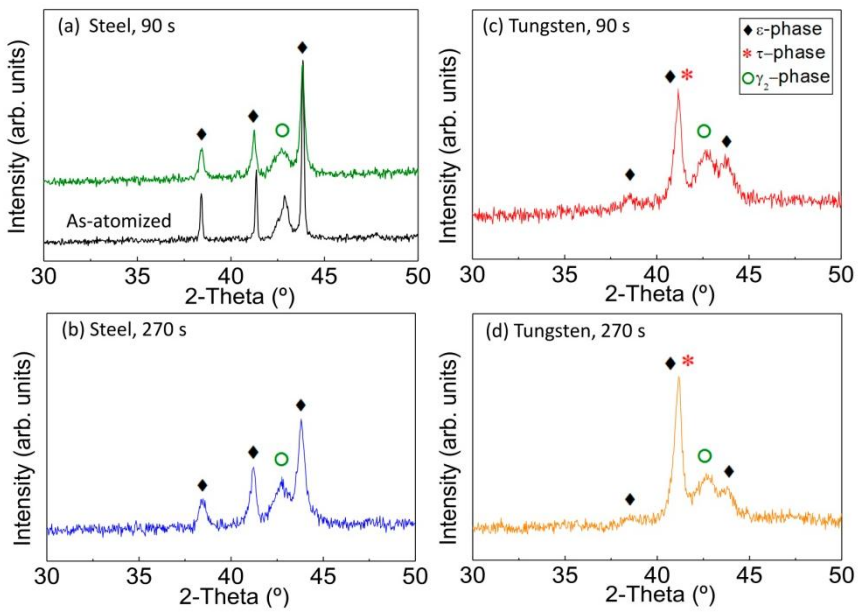

Figure 12. X-ray diffraction patterns of Mnal particles after milling with steel media for media for (a) 90 s and (b) 270 s; and tungsten carbide media for (c) 90 s and (d) 270 s. Fig. 2 (a) includes XRD pattern of the as-atomized MnAl powder for the aim comparison.

On the other hand, the use of tungsten carbide as milling media leads to the ε- into τ-MnAl phase transformation already in the as-milled state (Figure 12 (c) and (d)), which agrees with the results obtained in the previous section. The higher impact energy resulting from the larger density of the tungsten carbide also promotes a reduction of the ε-phase below 10 nm (in agreement with the previous section) and a beginning of amorphization after ball milling during just 90 s, as can be observed in Figure 12 (c).

The morphological and microstructural differences between the starting material, the samples milled with steel and the samples milled with tungsten carbide vials will cause different magnetic properties after the annealing process.

3.2.2 Optimization of the post-annealing temperature and magnetic characterization.

In order to optimize the annealed temperature, DSC measurements of the as-atomized and milled samples was performed to calculate the onset temperature in each material. In order to be systematic with the previous section, the DSC measurements were performed at 10 ºC/min in N_2 atmosphere. The different DSC curves are represented in Figure 13. It can be observed, by comparison between the different samples, a decrease in the transformation temperature values when increasing milling time and/or using a milling media with a higher density.

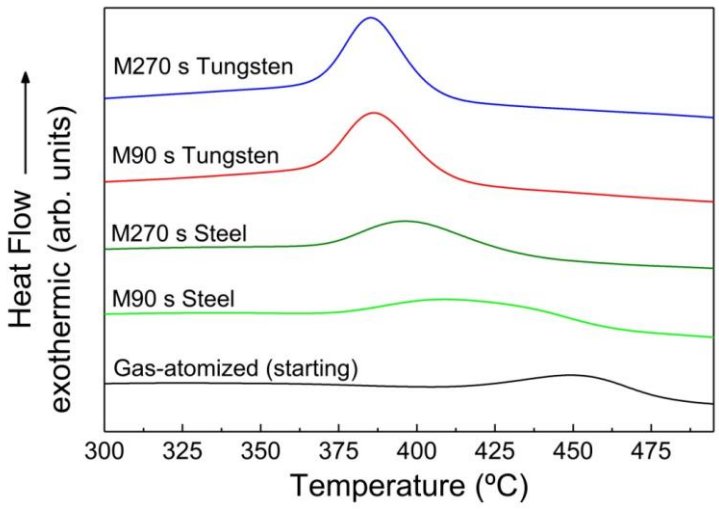

Figure 13. DSC measurements of the starting MnAl particles and the samples milled with steel media for media for 90 s and 270 s; and tungsten carbide media for 90 s and 270 s. Heating rate: 10 ºC/min.

In addition to the DSC analysis, and in order to get a better understanding of the phase evolution for each sample, temperature dependent XRD analysis has been performed. It has been studied the evolution of the XRD patterns between 35 and 50 º with in situ applied temperature (T-XRD maps) from 50 to 500 ºC, and it is represented in Figure 14.

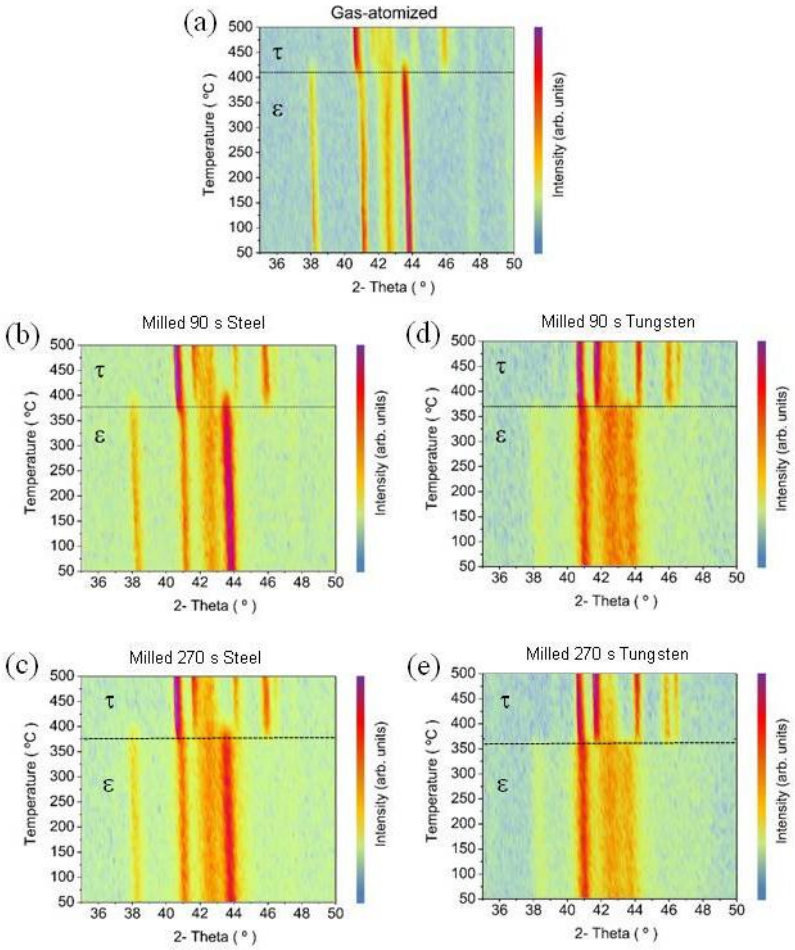

Figure 14. Temperature dependent X-ray diffraction pattern map of (a) gas-atomized MnAl powder; (b) powder milled with steel media for 90 (b) and 270 (c) s; and powder milled with tungsten carbide media for 90 (d) and 270 (e) s. Samples were annealed in-situ from 50 to 500 ºC using a temperature ramp of 1 K/min during recording of the measurement. Dashed lines are guide to the eyes showing the transition temperature for the transformation of ε- to τ-phase.

By comparison between the different T-XRD maps, it is also possible to conclude that the increment in the milling time and/or the use of a milling media with a higher density promotes a detriment in the transformation temperature. The transition temperatures calculated in this case are in

excellent agreement with those previously obtained by DSC measurements [Table 1].

Table 1.Transition temperature for the ε-to-τ phase transformation determined from the exothermic peak measured by DSC (Fig. 13), and onset temperature for beginning of the ε-to-τ phase transformation determined from the T-XRD maps (Fig. 14).

Material	**[DSC analysis]** T_{trans} **(ε-to-τ) (ºC)**	**[T-XRD maps]** T_{onset} **(ε-to-τ) (ºC)**
Gas-atomized (starting)	415 - 480	415
M90s Steel	375 - 465	375
M270s Steel	369 - 435	370
M90s Tungsten	368 - 410	365
M270s Tungsten	368 - 405	365

The reduction in the transformation temperature can be understood by considering the microstructural modification observed in XRD patterns of as-atomized and as-milled powders (Figure 12). The milling process leads to microstructural refinement of the gas-atomized MnAl powder accompanied by an increased disorder of the phases [81], causing a detriment in the energy needed to produce the transformation, producing therefore the ε→τ transition at lower temperature. This refinement will be more dramatic by increasing the milling time or by increasing the density of the milling media, due to the enhanced impact energy exerted to the powder during balls collision.

The microstructure refinement also evolves to amorphization with increasing milling time (Figure 12). The amorphous powder will crystallite into β-phase during the subsequent annealing of the as-milled powder at the same time that the ε-phase transforms into τ-phase (Figure 14). The coexistence of both phases was confirmed by STEM analysis of the powder resulting from recording the T-XRD map shown in Figure 14. Representative HAADF STEM micrographs from structures of both constituent phases are shown in Figure 15. These micrographs are determining the structures on the basis of their respective projections along indicated axes and measured inter-atomic (columnar) distances.

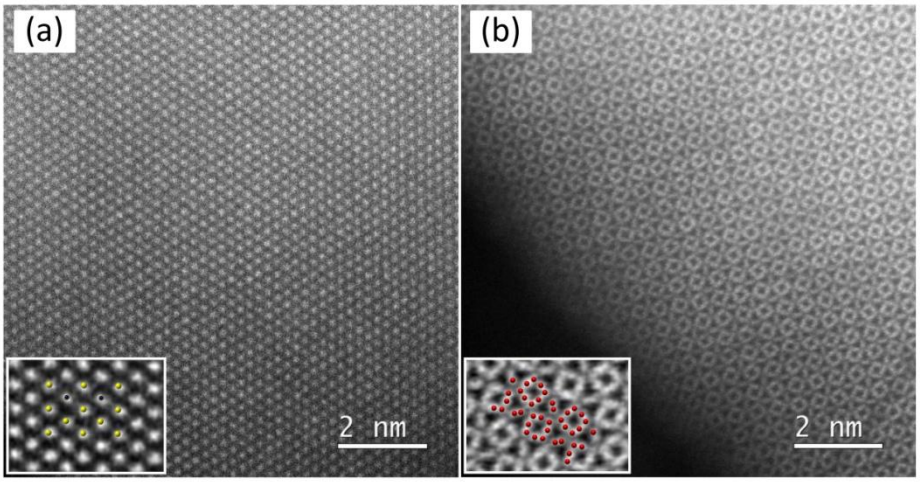

Figure 15. HAADF STEM micrographs confirming the presence of (a) τ-MnAl [011] and (b) β-(Al)Mn [010] phases coexisting in the MnAl powder milled for 270 s with tungsten carbide media. Corresponding unit cell models, 2 x 1 x 1, are overlaid in magnified Wiener filtered insets. Al- blue and Mn- yellow atomic positions are shown for the case of τ-MnAl and Al/Mn – red for the case of β-(Al)Mn [010]. Every projection is accompanied with the corresponding structural model overlay as shown from the Wiener filtered insets at the bottom of each micrograph.

In order to complete the analysis of the phases formed during the annealing, it has been represented in Figure 16 the XRD patterns of all samples under study at two different annealing temperatures (375 and 450 ºC), i.e. equivalent to two lines in the Y-axis of Figure 14, to study the evolution of ε-, τ- and β-phases in the starting powder and milled (90 and 270 s, with steel and tungsten carbide media) powders.

It is worth making a simplified analysis of the XRD evolution shown in Figure 16, which will be extremely useful to understand the evolution of the magnetic properties in the following section:

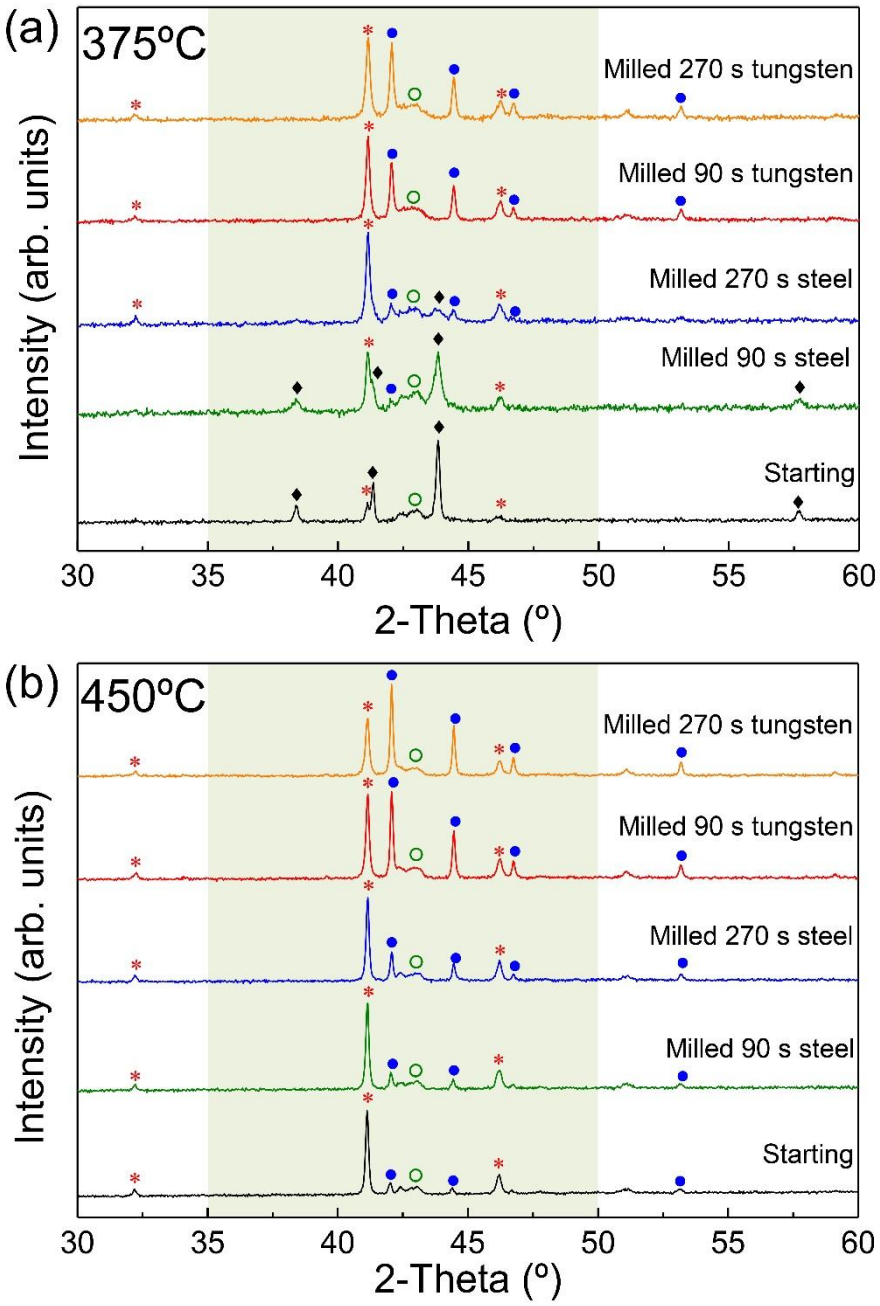

Figure 16. XRD patterns of the starting material and milled powders annealed at (a) 375 ºC and (b) 450 ºC for 10 min. (♦) ε-phase, (*) τ-phase, (●) β-phase and (o) γ_2-phase. Shaded area corresponds to the 2-Theta interval measured by T-XRD in Fig. 14

(a) Annealing at 375 ºC (see XRD patterns in Figure 16 (a)):

- Starting powder. Beginning of ε-to τ-MnAl phase transformation takes place. However, the temperature is not high enough to conclude the process, only to begin it. This is observed by the large amount of ε-phase that remains untransformed.
- Powder milled for 90 s with steel. The content of the τ-MnAl phase in the annealed powder is higher than that observed in the starting powder, and crystallization of β- phase occurs. Microstructural refinement at this early stage is thus working efficiently on phase transformation.
- Powder milled for 270 s with steel. Further microstructural refinement accompanied by beginning of amorphization leads to enhanced contents of τ and β phases after annealing at this temperature. However, the temperature is not high enough to guarantee complete transformation of the ε-phase.
- Powder milled for 90 s with tungsten carbide. The microstructural refinement and beginning of amorphization observed in the as-milled powder (Figure 12 (c)) explains the higher content of τ and β phases after annealing, respectively, by comparison with any of the previous samples (as-atomized and powder milled in steel even for a higher duration of 270 s). This short milling time is sufficient to guarantee the complete disappearance of the ε-phase after annealing at this rather low temperature.
- Powder milled for 270 s with tungsten carbide. Following the observed trend, a more powerful milling process accompanied by an increased milling time results in further refinement and a higher degree of amorphization (Figure 12 (d)), which eases the transformation of ε-phase to τ-MnAl phase and an increased recrystallization of the amorphous in β-phase upon annealing.

(b) Annealing at 450 ºC (see XRD patterns in Figure 16 (b)):

- Starting (as-atomized) powder. The ε- to τ-MnAl phase transformation is completed. A minor content of β-phase can be now observed. The γ_2-phase content does not vary significantly by comparison with that existing in the powder annealed at the lower temperature of 375 ºC.
- Powder milled for 90 s with steel. The use of a higher annealing temperature eases the complete transformation of ε- to τ-MnAl

phase and formation of the β-phase. The content of β-phase remains rather low since only microstructural refinement, with no amorphization effect, is obtained in the as-milled powder (Figure 12 (a)).

- Powder milled for 270 s with steel. A higher β-phase content is obtained by comparison with the powder resulting from the previous milling time (90 s). This is due to the recrystallization of the amorphous material created after this longer milling process. There is not any minor intensity peak of ε-phase by comparison with as-milled powder annealed at 375 ºC (Fig. 16(a)).
- Powder milled for 90 s with tungsten carbide. Annealing at 450 ºC results in complete crystallization of the amorphous material by comparison with powder annealed at 375 ºC. As a consequence a higher β-phase content is observed.
- Powder milled for 270 s with tungsten carbide. Following the observed trend, a more powerful milling process accompanied by an increased milling time results in further refinement and a higher degree of amorphization (Figure 12 (d)), which eases the transformation of ε-phase to τ-MnAl phase and an increased recrystallization of the amorphous in β-phase upon annealing.

The variation of the ratio between the τ- and β- phases with the annealing temperature is directly related with the magnetic properties. Hysteresis loops of the as-atomized powders and the samples milled 270 s (using steel and tungsten carbide media) annealed at 400 ºC are represented in Figure 17.

It can be observed that the sample milled 270 s with tungsten carbide media annealed at 400 ºC has similar magnetization than the starting material annealed at the same temperature, but the milled powder has a coercivity more than 3 times larger (4.6 kOe vs 1.5 kOe). On the other hand, the sample milled with steel media has the highest remanence of the three samples annealed at this temperature, with an intermediate coercivity of 2.8 kOe.

The differences in the magnetic properties between the three samples are directly related with the different phases presented. In the case of the milled samples, both samples have completed the ε→τ transformation, but the amount of the β-phase is higher in the sample milled with tungsten carbide media. The higher β/τ ratio in the sample milled with tungsten carbide promotes a lower magnetization and a higher coercivity than the sample milled 270 s with steel media. On the other hand, the as-atomized sample

presents the same magnetization than the sample milled 270 s with TC media, which means that both samples have the same amount of τ-phase. It occurs because the starting material has not finished the full transformation of the τ-phase, so the magnetization observed in the hysteresis loop shown in Figure 17 could increase by the increment of the annealing temperature, i.e. by the increment of the amount of τ-phase.

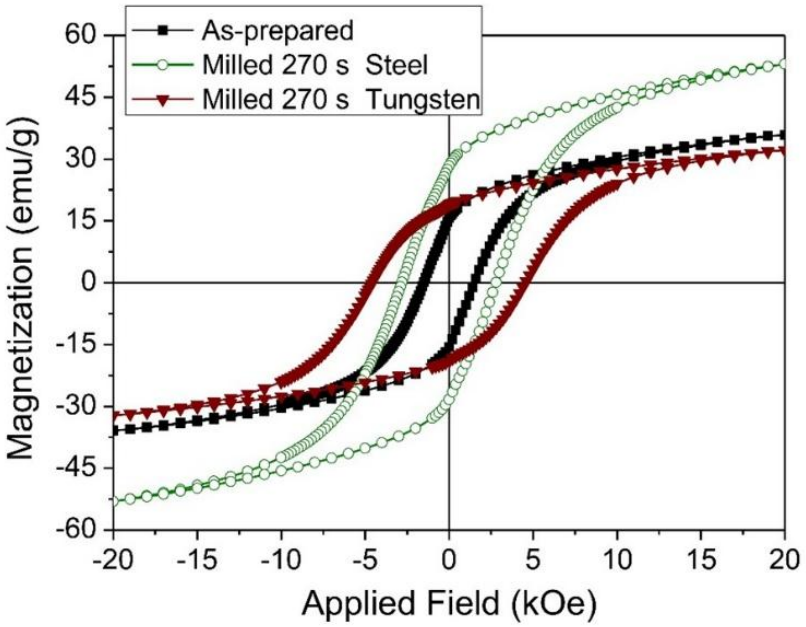

Figure 17. Hysteresis loop of the as-atomized material and the samples milled 270 s with steel and with tungsten carbide annealed at 400 ºC.

As the optimum temperature is not the same for all the samples, the correct comparison between the magnetic properties of each sample should be done by the study of the evolution of $M_{20\ kOe,}$ M_r and H_c of the starting material and the different milled powders with annealing temperature. This comparison is shown in Figure 18.

The left-hand side column shows the evolution of the magnetic properties for MnAl powder milled with steel, whereas the column on the right corresponds to the powder milled with tungsten carbide. As in the previous experiment, it is worth mentioning that recording of the hysteresis loops was done with a maximum applied magnetic field of 20 kOe, which means that the samples were not fully saturated. In all cases, and for comparison purposes, magnetic properties of the gas-atomized powder under identical annealing conditions are included.

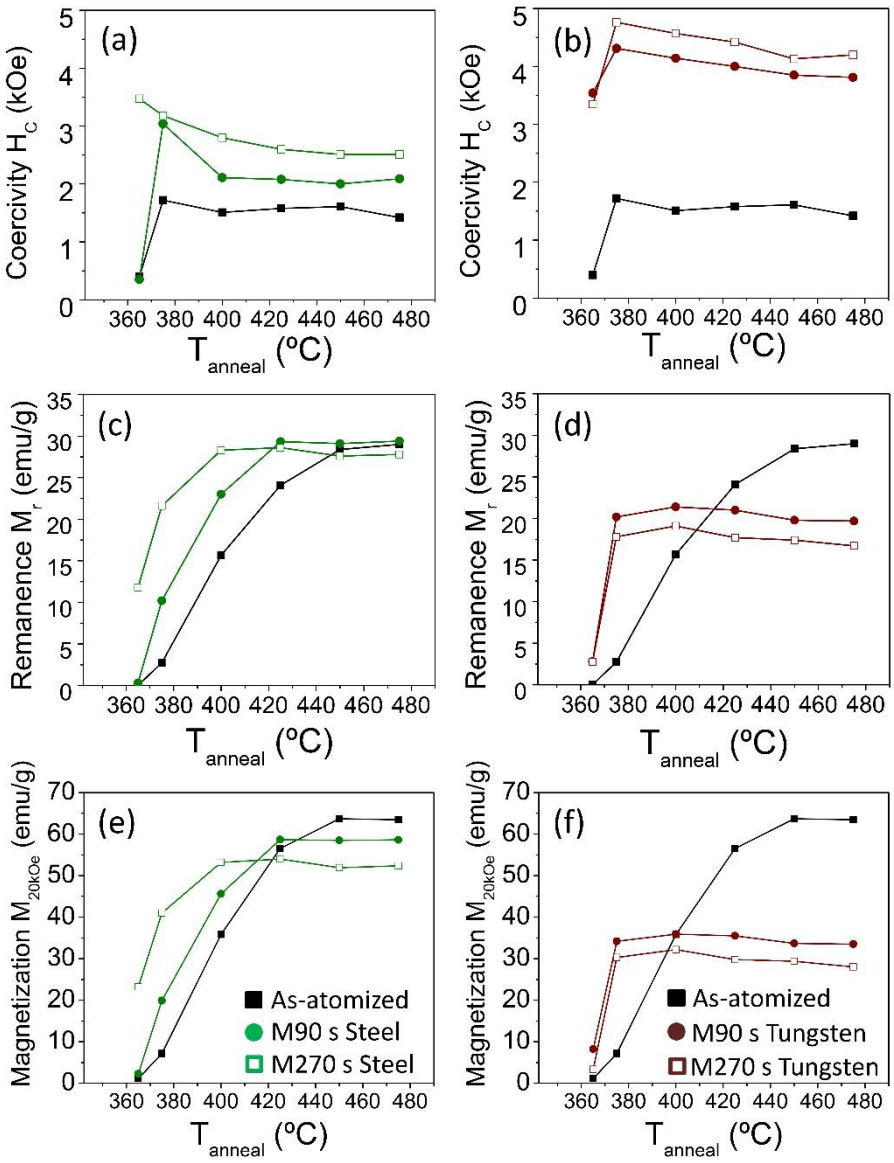

Figure 18. Influence of annealing temperature, T_{anneal}, on coercivity H_c ((a) and (b)); remanence, M_r ((c) and (d)); and magnetization measured with a maximum applied field of 20 KOe, M_{20kOe} ((e) and (f)), for the starting material and powders milled (90 and 270 s) with steel and tungsten carbide.

(i) Evolution of coercivity, H_c.

The evolution of coercivity with the annealing temperature, T_{anneal}, for powder milled with steel and tungsten carbide can be observed in Figs. 18(a) and 18(b), respectively. In both cases and independently of the material used as milling media, an increase in Hc is observed for a fixed T_{anneal} when increasing the milling time, and also by comparison with Hc of the as-atomized powder. This effect correlates well with an enhanced β-phase content resulting from crystallization of the amorphous material created during extended milling (Figs. 14 and 15). Enhancement in coercivity has been previously correlated with an increased β-phase content in the MnAl system, and attributed to the role played by this phase as pinning centers during magnetization reversal [63] [81]. In addition to effects related to phase transformation, the microstrain induced during milling is enhanced with increasing the milling time. This effect, in combination with a reduced mean crystallite size, eases the creation of defects, which will also act as pinning centers [80], i.e. enhancing coercivity. The main difference between both types of pinning centers is that the β-phase will not be removed through annealing (as β is a stable phase) while those finding its origin in the induced strain will disappear by increasing T_{anneal} due to relaxation effects. Maximum coercivity values of 1.7 kOe (T_{anneal}=375 ºC), 3.0 kOe (375 ºC) and 3.5 kOe (365 ºC) are obtained for as-atomized, milled 90 s and milled 270 s, respectively. The last two values contrast with the enhanced coercivities of 4.3 and 4.8 kOe (375 ºC) obtained by milling for 90 and 270 s, respectively, with tungsten carbide media.

Therefore, it is clearly shown that, as in the previous work, an increment of the milling time enhances the coercivity of the sample. In addition to that, it is also proved that a higher density of the milling media will promote higher coercivity. It is observed a difference superior to 1 kOe between the samples milled the same time but with different milling media (1.5 between the samples milled 90 s and 1.5 kOe between the samples milled 270 s)

It must be remarked that not only coercivity but also magnetization values (discussed in the following) need to be addressed before deciding the best combination of magnetic properties (H_c and M_r, in particular).

(ii) Evolution of magnetization: remanence, M_r, and magnetization at 20 kOe, M_{20kOe}.

Magnetization values dependence on the milling time and the annealing temperature are shown in Figs. 18(c)-(f) for the gas-atomized powder milled in steel and tungsten carbide media. As the τ-phase is the only ferromagnetic phase in the MnAl, the evolution of the magnetization is directly related with the evolution of the τ-phase in each sample.

It was explained before how the microstructure refinements reduce the thermal energy needed to nucleate the τ-phase, i.e. the ferromagnetic τ-phase is formed at lower temperature in the milled samples. Accordingly, there is a shift to lower values in the annealing temperature needed to achieve optimized M_r (Figs. 18(c) and (d)) and M_{20kOe} (Figs. 18(e) and (f)) when comparing as-atomized and as-milled powders. In the case of milling with steel, a progressive shift to lower temperatures (425 and 400 ºC) is observed when increasing the milling time (90 and 270 s) by comparison with that needed for the as-atomized powder (450 ºC). A more dramatic decrease (375 ºC, i.e. 75 ºC lower than that of the as-atomized powder) is observed when milling with tungsten carbide independently of the milling time. Best magnetic properties of each sample and the temperature needed to achieve these properties are shown in Table 2. Temperatures shown in Table 2 agree well with observations done from the DSC results on determination of the onset temperature for the formation of the τ-MnAl phase. They also agree with the results obtained from the temperature dependent XRD maps shown in Figure 14.

Table 2. Annealing temperature, $\mathbf{T_{anneal}^{opt}}$, required to achieve an optimized combination of magnetic properties (M20kOe, Mr and Hc) for gas-atomized powder in the as-prepared state and after milling with steel and tungsten carbide, TC (milling times of 90 and 270 s).

Materials	T_{anneal}^{opt} (ºC)	M_{20kOe} (emu/g)	M_r (emu/g)	H_c (kOe)
As-atomized	450	63.7	28.4	1.6
M90s Steel	425	58.7	29.1	2.1
M270s Steel	400	53.2	28.6	2.8
M90 s TC	375	34.2	20.2	4.3
M270 s TC	375	30.3	17.8	4.8

The observation already done when discussing the XRD results (Figs. 14 and 16) related to the recrystallization through annealing of the amorphous phase produced during milling in the more favorable β-phase (stable) against the τ-MnAl phase (metastable) is the reason behind the variation in the magnetization values observed in Fig. 18. A higher content of β-phase in samples milled for longer times and/or with higher density milling media has

an associated decrease in the content of the τ-MnAl phase, which results in lower magnetization values (M_r and M_{20kOe}). The annealed as-atomized material shows the lowest β-phase content after annealing, and the highest τ-MnAl phase content (Figure 16 (b))among the samples under study, which results in the largest M_{20kOe} value of about 64 emu/g. By comparison, the use of tungsten carbide as milling media results in a high amorphization level of the as-atomized powder and, subsequent annealing favors recrystallization in β-phase from the amorphous material. As a consequence, the lowest magnetization values are obtained for the longest milling time and by using the milling media of higher density, accompanied by the largest coercivity (result from the combination of defects induced during milling and the highest β-phase content, both acting as pinning centers). As it is shown in Table 2, the samples milled with steel media present a gradual decrease in magnetization and increase in coercivity, which correlates with the morphological and microstructural features induced during milling. The lower impact energy of the steel balls eases to modify the microstructure of the particles without the formation of high amount of amorphous powder, maintaining therefore a high magnetization. The samples milled during 90s and 270 s with steel achieve the same remanence than the starting material with a T_{anneal}^{opt} 25 and 50 ºC lower than the as-atomized powder, respectively (Table 2).

As a result, it is possible to classify the samples obtained in two different groups, attending to the magnetic properties obtained by the choice of the milling media and the annealing parameters:

-High coercive MnAl powder: the samples milled with tungsten carbide can reach a coercivity up to 4.8 kOe, 3 times larger that of the as atomized powder. The amount of β-phase is higher than the 50% of the crystalline powder, obtaining therefore a magnetization below 40 emu/g.

-MnAl powder with a balanced combination of magnetization and coercivity: an increase in coercivity of about 57% (H_c = 2.8 kOe vs 1.6 kOe for the starting) while preserving the remanence of the starting powder finds a good compromise to maintain a good combination of PM properties.

3.3 Conclusions

Isotropic nanocrystalline $Mn_{54}Al_{46}$ permanent magnet powder with quasi-spherical particles produced by gas-atomization process with no presence of τ-phase has been successfully improved by nanostructuring and controlled phase transformation.

The optimization of the milling time and the use of milling media with dissimilar densities have allowed to establish a correlation between morphology, microstructure and magnetic properties. It has been reported how 30 s of milling time with tungsten carbide vials can reduce the crystallite size to 17 nm without practically any amorphization of the powder, while the increment of the milling time above 90 s reduce the crystallite size below 10 nm and produces amorphization in the MnAl powder. It is also possible to reduce the amorphization produced by the choice of the milling media with a lower density, like the steel. The ball milling process with steel media can reduce the crystallite size of the ε-phase below 15 nm with a low amount of amorphous powder.

It has been also reported, for the first time, the formation of τ-phase during the milling process without any content of τ-phase in the starting material, by the induction of the strain in the particles and the induced disorder during the milling process. It is only possible through the use of tungsten carbide as material of the milling media, because a high impact energy is needed to produce the transformation without any heat treatment.

The post-annealing technique used in this work transforms the ε-phase into the ferromagnetic τ-phase and, simultaneously, recrystallize the amorphous powder into the non-magnetic β-phase. The defects and the strain originated during the milling process reduce the thermal energy needed to nucleate the τ-phase, reducing the onset temperature of the nucleation of the τ-phase. It has been proved by DSD and T-XRD measurements how the milling process can reduce the onset temperature from 415 ºC to 365 ºC.

A correlation has been established between the phases of the MnAl obtained after the annealing process and the magnetic properties of the powder. The rather low coercivity typically associated to a pure τ-phase MnAl alloy has been overcome by the inducement of strain during the milling process and the creation of β-phase from recrystallization of the amorphous phase through post-annealing.

Ball milling during the unprecedented time of just 270 s enhances the coercivity up to 5.1 kOe. This enhancement is obtained through the increment of the strain above 0.25% and the formation of the β-phase (which is acting as pinning center). A coercivity of 5.1 kOe is one on the highest values reported in literature, and it is the first time reported that a coercive field above 5 kOe is obtained in less than 5 minutes of ball milling; the second shortest time reported is 2 h. However, as the τ-phase is the only ferromagnetic phase in the MnAl system, the high amount of β-phase produced reduces the magnetization of the system.

A milder milling process with steel media (close-to-half density of tungsten carbide) halves the value of the energy transferred in a collision and thus results in less strained grains and diminished amorphization effects. As a consequence, the β/τ ratio is reduced, causing an increment in the magnetization of the samples milled with steel. 270 s of milling with steel vials achieves a M_{20kOe} 23 emu/g higher than the sample milled the same time but using tungsten carbide as milling media (53.2 vs 30.3 emu/g), and it maintains practically unchanged the remanence (about 30 emu/g) of the annealed gas-atomized particles. On the other hand, given that the β-phase raises the coercivity, the use of steel as milling media prevents the increment of the coercivity above 3.5 kOe.

A similar result is obtained by the reduction of the milling time. 30 s of milling with tungsten carbide vials induce enough strain as to increase the coercivity of the starting material more than 100% and it maintains, at the same time, the remanence of the starting material.

It is concluded, therefore, that it is possible to control the microstructure refinement produced during the milling process, being able to choose between producing a material with good coercivity and good remanence, or producing a material with a very high coercivity to combine it with a soft material.

Bibliography

[1] Q Zeng, I Baker, JB Cui, and ZC Yan. Structural and magnetic properties of nanostructured mn–al–c magnetic materials. *Journal of Magnetism and Magnetic Materials*, 308(2):214–226, 2007.

[2] Luke G Marshall, Ian J McDonald, and LH Lewis. Quantification of the strain-induced promotion of τ-mnal via cryogenic milling. *Journal of Magnetism and Magnetic Materials*, 404:215–220, 2016.

[3] Jung-Goo Lee, Xiao-Lei Wang, Zhi-Dong Zhang, and ChuI-Jin Choi. Effect of mechanical milling and heat treatment on the structure and magnetic properties of gas atomized mn–al alloy powders. *Thin Solid Films*, 519(23):8312–8316, 2011.

[4] Hailiang Fang, Sofia Kontos, Jonas Ångström, Johan Cedervall, Peter Svedlindh, Klas Gunnarsson, and Martin Sahlberg. Directly obtained τ-phase mnal, a high performance magnetic material for permanent magnets. *Journal of Solid State Chemistry*, 237:300–306, 2016.

[5] Wei Lu, Junchao Niu, Taolei Wang, Kada Xia, Zhen Xiang, Yiming Song, Hong Zhang, Satoru Yoshimura, and Hitoshi Saito. Low-energy mechanically milled τ-phase mnal alloys with high coercivity and magnetization. *Journal of Alloys and Compounds*, 675:163–167, 2016.

[6] Anurag Chaturvedi, Rumana Yaqub, and Ian Baker. A comparison of τ-mnal particulates produced via different routes. *Journal of Physics: Condensed Matter*, 26(6):064201, 2014.

[7] Anurag Chaturvedi, Rumana Yaqub, and Ian Baker. Microstructure and magnetic properties of bulk nanocrystalline mnal. *Metals*, 4(1):20–27, 2014.

[8] FJ Pedrosa, J Rial, KM Golasinski, M Rodrguez-Osorio, G Salas, D Granados, J Camarero, and A Bollero. Tunable nanocrystalline cofe 2 o 4 isotropic powders obtained by co-precipitation and ultrafast ball milling for permanent magnet applications. *RSC Advances*, 6(90):87282–87287, 2016.

[9] Bernard Dennis Cullity. Elements of x-ray diffraction. 2001.

[10] JJ Van Den Broek, H Donkersloot, G Van Tendeloo, and J Van Landuyt. Phase transformations in pure and carbon-doped al45mn55 alloys. *Acta Metallurgica*, 27(9):1497–1504, 1979.

[11] Thaddeus B Massalski et al. Binary alloy phase diagrams asm international. *Materials Park, OH*, pages 1442–1446, 1990.

[12] JZ Wei, ZG Song, YB Yang, SQ Liu, HL Du, JZ Han, D Zhou, CS Wang, YC Yang, A Franz, et al. τ-mnal with high coercivity and saturation magnetization. *AIP Advances*, 4(12):127113, 2014.

[13] P Saravanan, Jen-Hwa Hsu, VTP Vinod, Miroslav Cernk, and SV Kamat. Coercivity enhancement in mn-al-cu flakes produced by surfactant-assisted milling. *Ápplied Physics Letters*, 107(19):192407, 2015.

[14] H Zhao, WY Yang, ZY Shao, G Tian, D Zhou, XP Chen, YH Xia, L Xie, SQ Liu, HL Du, et al. Structural evolution and magnetic properties of l10-type mn54. 5al45. 5-xgax (x= 0.0, 15.0, 25.0, 35.0, 45.5) phase. *Journal of Alloys and Compounds*, 680:14–19, 2016.

[15] T Klemmer, D Hoydick, H Okumura, B Zhang, and WA Soffa. Magnetic hardening and coercivity mechanisms in l10 ordered fepd ferromagnets. *Scripta Metallurgica et Materialia*, 33(10-11):1793–1805, 1995.

[16] F Bittner, J Freudenberger, L Schultz, and TG Woodcock. The impact of dislocations on coercivity in l10-mnal. *Journal of Alloys and Compounds*, 704:528–536, 2017.

[17] Shuang Zhao, Yuye Wu, Chi Zhang, Jingmin Wang, Zhongheng Fu, Ruifeng Zhang, and Chengbao Jiang. Stabilization of τ-phase in carbon-doped mnal magnetic alloys. *Journal of Alloys and Compounds*, 755:257–264, 2018.

[18] N Burgio, A Iasonna, M Magini, S Martelli, and F Padella. Mechanical alloying of the fe- zr system. correlation between input energy and end products. *Il nuovo cimento D*, 13(4):459–476, 1991.

Chapter 4

4.Influence of composition and starting morphology in the nanostructuring of MnAlC gas-atomization powder.

MnAl gas atomized powder doped with Carbon has been nanostructured by ball milling and post-annealing treatment. The relation between the initial composition and particle size with the effectiveness of the nanostructuring process is studied in this chapter. Furthermore, it has been analyzed the influence of the starting phase (ε- or τ- phase) in the magnetic properties after the milling and annealing process. Morphological, microstructural and magnetic characterizations of the starting and milled samples have been performed.

4.1 Influence of precursor on gas-atomized and milled powder: comparison of ε- and τ-MnAl based powders.

MnAl system presents only one ferromagnetic phase, the τ-phase. For that reason, the formation of this ferromagnetic phase is necessary to develop permanent magnet properties in the MnAl powder. As the τ-phase can be obtained from the ε-phase by an annealing process, there are two possible ways to nanostructure the material.

Some groups have reported a nanostructuring process where ε-phase is first transformed into τ-phase and, once that the powder is ferromagnetic, a subsequent milling process is applied to improve the magnetic properties [81] [21] [59]. On the other hand, it has been also reported that it can be first nanostructured the ε-phase, creating defects and changing the morphology and microstructure of the sample, and a subsequent annealing process to transform

the ε-phase into τ-phase is performed after the nanostructuration process [63] [6] [21].

To perform the best optimization possible in the magnetic properties, it is necessary to analyze which of these two routes is better in the nanostructuring of the MnAlC gas-atomized powder through the fast-milling process.

Same milling parameters than in the previous chapter have been used in this section. The milling process has been performed using a rotation speed of 900 rpm with tungsten carbide vials and balls, as well as ball-to-powder mass of 40:1. The powders were milled by surfactant-assisted (oleic acid) mechanical milling, in order to reduce possible oxidation and mitigate agglomeration. The powder-to-oleic acid ratio used in this experiment was 5:1. The milling time used was 270 s.

4.1.1. Microstructural characterization

Two different powders were used in this experiment. In order to analyze just the differences between the two possible routes explained before, both samples have the same composition, $(Mn_{57}Al_{43})_{100}C_{1.2}$.

Morphology and microstructure of each sample are represented in Figure 1. It can be observed that, besides the composition, both samples present similar particle size (below 50 μm). The only difference between them is, therefore, the predominant phase in each sample. Whereas the sample 1 present more than 90% of ε-phase (Figure 1 (c)), sample 2 does not show any amount of ε-phase in its XRD-pattern, presenting almost all τ-phase, with a few amount of the non-magnetic β- and γ_2-phases (Figure 1 (d)).

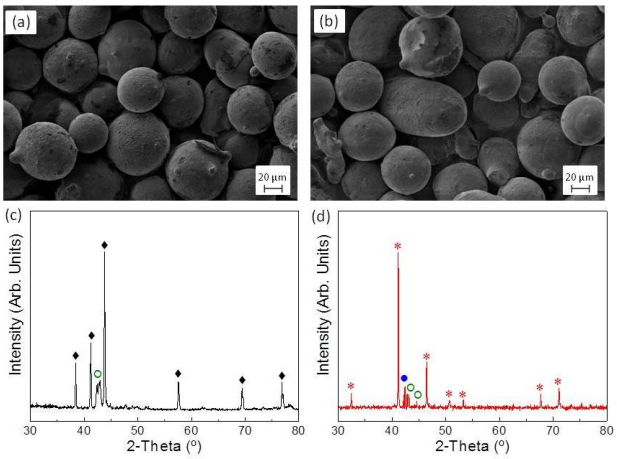

Figure 1. SEM images ((a) and (b)) and XRD patterns ((c) and (d)) of the sample 1 and 2, respectively. Phase identification: (♦) ε-phase, (o) γ_2-phase, (●) β-phase and (∗) τ-phase.

VSM results of both starting samples, showed in Figure 2, correlate perfectly with the XRD measurements, showing only a ferromagnetic hysteresis loop in the sample 2, due to the τ-phase content in this sample. On the other hand, sample 1 requires application of annealing to proceed with the ε-to-τ phase transformation, i.e., to develop the permanent magnet properties.

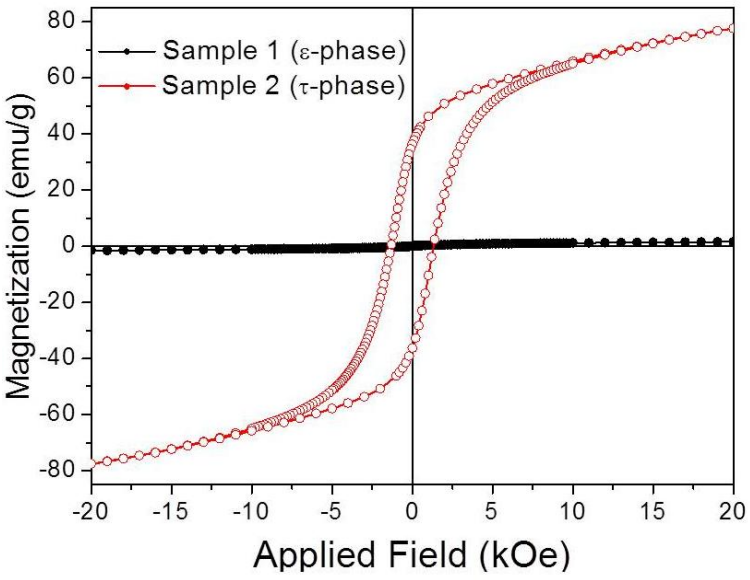

Figure 2. Magnetic response of the as prepared sample 1 and 2.

In order to compare the two possible routes mentioned before, sample 1 (ε-phase) and sample 2 (τ-phase) were nanostructured by ball milling process during 270 s, modifying their morphology and their microstructure. SEM images of the gas-atomized samples after the milling process are shown in Figure 3.

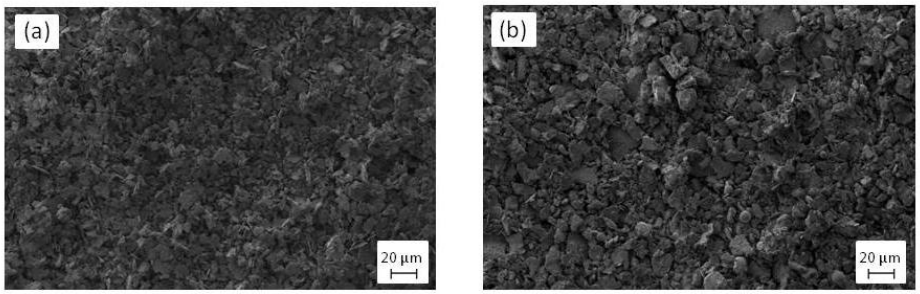

Figure 3: SEM images of (a) sample 1 and (b) sample 2 after fast-ball-milling for 270 s.

It is observed in Figure 3 how the milling process produces similar morphological modifications in both samples. Independently of the initial phases, the ball-milling process is able to reduce the particle size of the powder below 10 µm. However, the similarities observed in the morphology contrast drastically with the important differences that can be appreciated in the microstructure of each samples after the milling process. XRD patterns of the milled sample 1 (a) and milled sample 2 (b) are shown in Figure 4. As it is shown, while the milling process changes drastically the microstructure of the sample 1 (the sample with ε-phase), producing high amount of amorphous powder and reducing its mean crystallite size under 10 nm, the same process in the sample 2 only produces a reduction of the mean crystallite size of the τ-phase, from 60 to 20 nm, without any important amorphization in the powder.

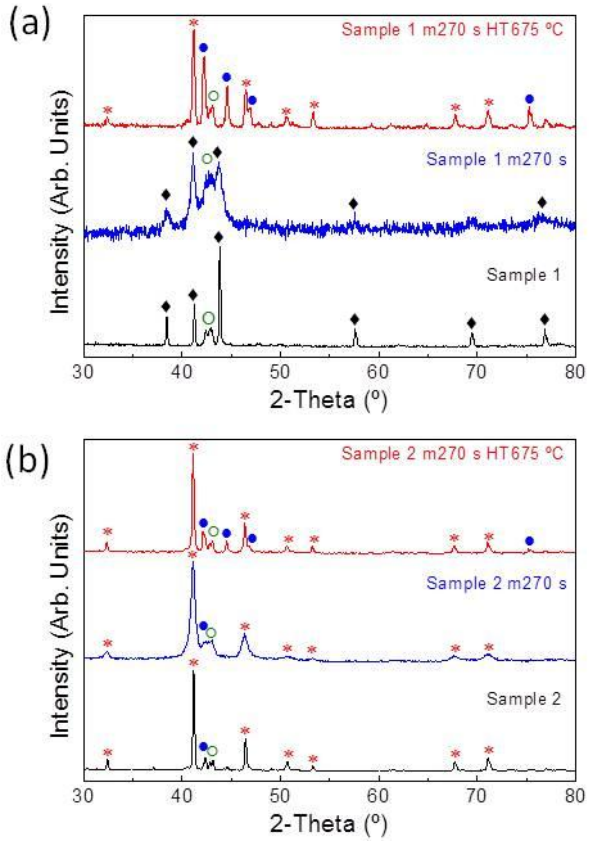

Figure 4: XRD patterns of (a) sample 1 and (b) sample 2 in different states: as-atomized, as-milled and after milling and annealing. Phase identification: (♦) ε-phase, (o) γ_2-phase, (●) β-phase and (∗) τ-phase.

The difference between the two samples proves that the τ-phase structure, the tetragonal $L1_0$, is more stable than the hexagonal hcp ε-phase. While the morphological changes are the same, the τ-phase sample presents lower amount of microstructural changes after the milling process, blocking therefore the nanostructuration of the material. It causes that, after an annealing process at 675 ºC during 10 min in N_2 atmosphere, the ratio of β-phase in both samples presents important differences (Figure 4). The sample 1, that has been partially amorphized during the milling process, has a β/τ ratio of 0.9. On the hand, the sample 2 only shows a slight increment in the β/τ ratio, in comparison with the starting material, from 0.1 to 0.2.

The difference ratio of the phases achieved in each sample, depending on the route chosen to modify the microstructure, will strongly influence the magnetic properties of each sample.

4.1.2 Magnetic characterization

Figure 5 shows the second quadrant of the hysteresis loops of the different ferromagnetic samples analyzed during the experiment.

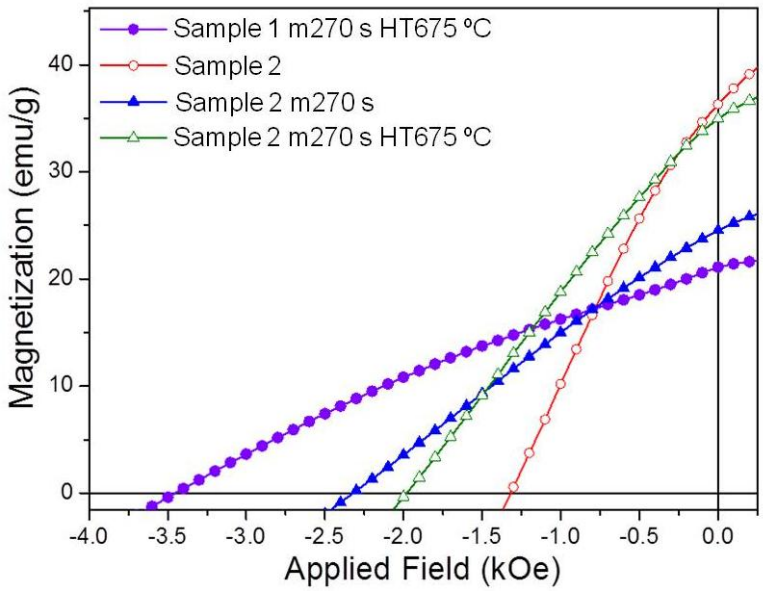

Figure 5: Hysteresis loops of samples 1 and 2 after milling and annealing process.

As it was expected, the sample with the highest remanence magnetization is the as-prepared sample 2. The starting sample 2 is an almost pure τ-phase sample, so the magnetization of this powder is the highest of the samples analyzed. On the other hand, as the ball milling process has not been applied to this sample, the coercivity is the lowest of the four samples represented in Figure 5.

The second sample with the highest magnetization and the lowest coercivity is the sample 2 after the milling and annealing process. The annealing after the milling process dissipates any possible strain induced in the sample and, as the order in the sample is the same than in the starting sample 2, the magnetization is almost the same. The slightly increase in coercivity is due to the formation of β-phase, which could be acting as pinning center. This result proves that the milling and annealing process applied to a τ-phase powder is able to increase its coercivity while maintaining the initial remanence of the powder. However, the increment in coercivity is too low as to use the material for permanent magnet applications.

An important drop in magnetization can be observed between the two samples mentioned and the next two samples. The τ-phase-sample 2 only milled during 270 s decreases its remanence magnetization up to 24 emu/g, 10 emu/g lower than the others two samples. If it is true that the milling process is not able to amorphize this powder, the high-energy ball milling process disorders the τ-phase structure, causing an antiferromagnetic coupling between the Mn in the tetragonal structure. For that reason, while the amount of τ-phase observed in the Figure 4 (b) of the three τ-phase-samples is practically constant, the remanence magnetization of the sample 2 milled 270 s is almost 30% lower than the other two τ-phase samples. The disorder of the τ-phase does not produce any change in the coercivity values, being the strain induced during the milling process the responsible of the slight difference between the sample 2 milled and the sample 2 milled and annealed.

The sample with the highest coercivity is the sample 1, the almost pure ε-phase sample that has been first milled and subsequently annealed at 675 ºC. The milling process is very effective in this sample, easing the creating of a high amount of β-phase during the annealing process. If it is true that the formation of β-phase reduces the magnetization, the sample 1 milled and annealed presents a coercivity of 3.5 kOe, more than 1 kOe higher than the milled sample 2, with a remanence magnetization only 3 emu/g lower than the milled τ-phase sample (Figure 5).

The magnetic results obtained prove that both routes can be successfully applied in the gas-atomized samples to improve the magnetic properties of the powder. The milled and annealed sample 2 has higher Hc than the starting material, while maintaining very close Mr values. On the other hand, starting from ε-based material (sample 1) results in larger coercivity in view of the use of this material in exchange-coupled composites.

As the aim of this part of the study is achieving a MnAlC powder with high coercivity to be used as hard magnetic phase, the study will be focused in the processing (fast-milling and annealing) of as-atomized ε-phase materials.

4.2 Composition and particle size optimization of the gas atomized MnAlC precursor powder

In the previous chapter, it has been explained the improvement of coercivity in MnAl gas-atomized particles through the fast-ball milling process, by the induction of strain and the formation of β-phase, which could be acting as pinning center. However, as the β-phase is a non-ferromagnetic phase, i.e. its formation decreases the magnetization of the sample, it is necessary to control the formation of this phase in order to improve the coercivity without producing big losses in magnetization.

The big differences between the milling time used by the different authors, explained in the introduction, demonstrated that the milling parameters can be influenced by the starting MnAl material properties. The initial particles shape (which will be given by the fabrication techniques, e.g. approximately spherical particles obtained by gas-atomization or ribbons fabricated by melt-spinning), the size of the particles or its composition will be crucial for the magnetic properties development.

Herein it is reported a deep study about obtaining the desired structures in the MnAl gas-atomized powder through the control of the nanostructuring process, considering the influence of the composition and particle size of the starting MnAlC gas-atomized particles on the formation of the different crystallographic phases and, consequently, on the development of permanent magnet properties.

MnAlC powders prepared by gas-atomization process under argon atmosphere have been used as starting material. The compositions of the powder in this work have been $(Mn_{57}Al_{43})_{100}C_{1.2}$ and $(Mn_{54}Al_{46})_{100}C_{0.8}$ (± 0.4 % at composition), namely Composition A and B in the following, respectively. Gas atomization powders were sieved in three different particle size ranges (<36 μm, 45-75 μm and 100-180μm, namely range 1, 2 and 3 in the following, respectively). The combination of composition and particle size gives six different samples, which further on the text will be referred with a name resulting from the combination of the composition (i.e., *A* or *B*) and the particle size (i.e., *1*, *2* or *3*).

The sieved MnAlC samples were milled using the same parameters than in the previous section: during 270 s using oleic acid as surfactant to avoid particles oxidation and mitigate agglomeration. The ball milling process was performed

at a rotation speed of 900 rpm. All the samples were milled with tungsten carbide vials and balls allowing for a high collision energy ($E= 8.3 \times 10^4$ J/collision) due to the high density of the material (15.8 g/cm^3). A balls-to-powder mass ratio of 40:1 and a powder-to-oleic acid ratio of 5:1 were used in the milling experiments. The vials loading and sealing were performed in an Ar-controlled atmosphere glove box to prevent oxidation. As-atomized and milled samples were annealed in N_2 at 675 ºC with a heating ramp of 10K/min.

4.2.1 Microstructural characterization

The starting gas-atomized powder consists on quasi-spherical particles with different particle size: < 36 μm, 45-75 μm and 100-180 μm (Figure 6). XRD patterns of the different starting powders are represented in Figure 7. Independently of particle size or composition, more than 90% of the sample shows an ε-phase based crystallographic structure, being γ_2-phase the remaining amount. This small amount of γ_2-phase is formed during the gas-atomization if the cooling process is not fast enough [Chatuverdi2014(2)]. It is observed that the amount of γ_2 is slightly higher in particles made of composition B, due to the lower amount of Mn. It is shown in the phase diagram of the MnAl how low amount of Mn promotes the formation of γ_2-phase, and high amount of Mn eases the formation of β-phase [64]. The mean crystallite size of the ε-phase in the gas-atomized samples is 100 ± 10 nm for both compositions, and for all the particles sizes included in this study.

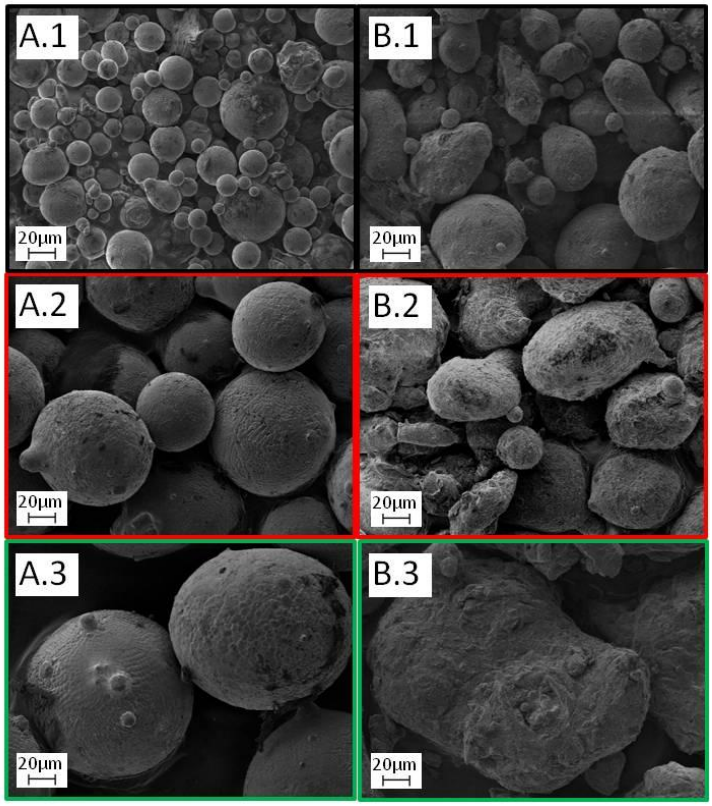

Figure 6. SEM images of the starting powders for both composition (A and B) and for the three different particle size: (1) <36 µm, (2) 45-75 µm and (3) 100-180 µm.

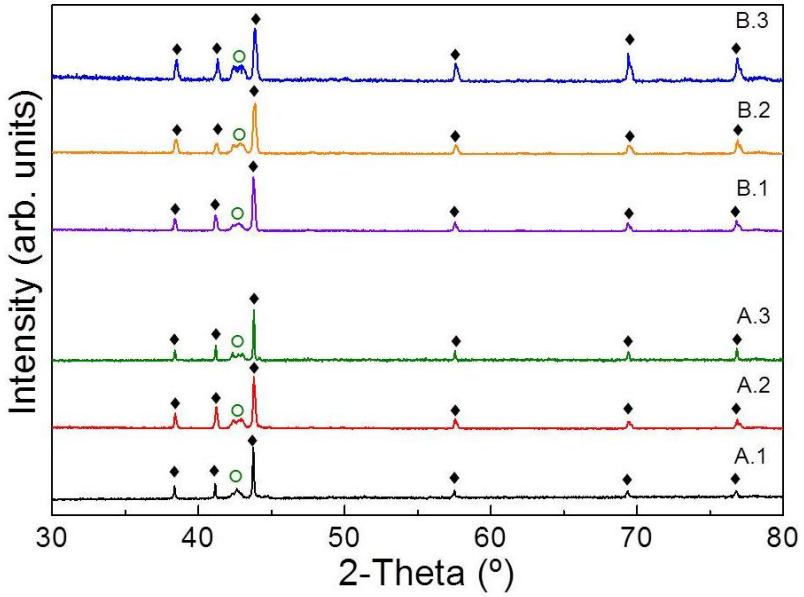

Figure 7. X-ray diffraction patterns of the different gas-atomized samples. Phase identification: (♦) ε-phase, and (o) γ_2-phase

The different gas-atomized powders were ultrafast ball-milled for a milling time of 270 s. Morphological and microstructural characterization of the milled A and B samples are represented in Figure 8 and 9, respectively.

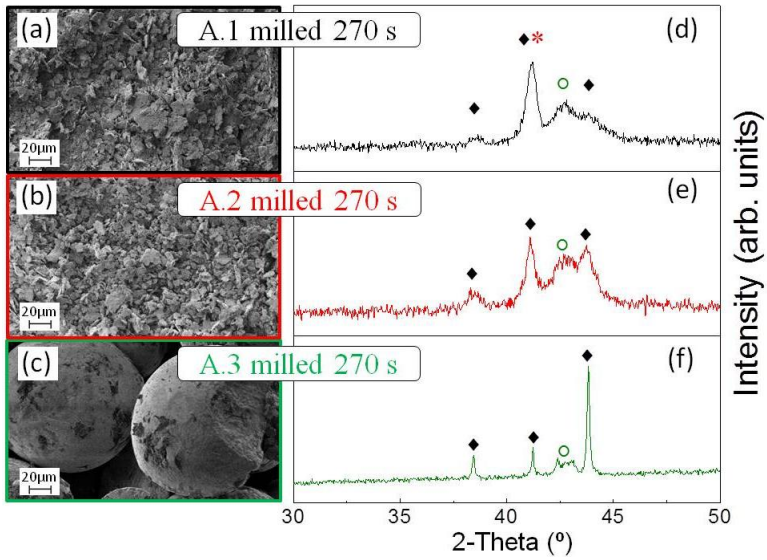

Figure 8. SEM images ((a), (b) and (c)) and XRD patterns ((d), (e) and (f)) of the milled A samples with different starting particle size: <36 μm, 45-75μm and 100-180 μm. Phase identification: (♦) ε-phase, (o) γ_2-phase, and (∗) τ-phase.

It is observed how the ball-milling process is very effective in samples with a particle size below 75 μm, transforming their initial quasi-spherical morphology into flake-like shape particles (Fig. 8(a) and (b) and Fig 9 (a) and (b)) in comparison to the quasi-spheres that are still observed in the A.3 and B.3 samples (Fig. 8(c) and 9(c)). In order to compare the evolution of the morphology of the A- and B- samples, it has been calculated the average particle size of the different milled samples by analysis of the SEM images. Milled A.1 and A.2 samples show smaller particle size (6 and 8 μm, respectively) in comparison to the B.1 and B.2 powders (9 and 11 μm), which indicates that milling process is more efficient for reducing particle size in the samples with higher content of Mn. The thickness of the flake-like shape particles originated during the milling process is between 1 and 2 μm for both composition (Fig. 10). Milled A.3 and B.3 samples present a particle size above 100 μm, which is similar to the particle size of the starting powders.

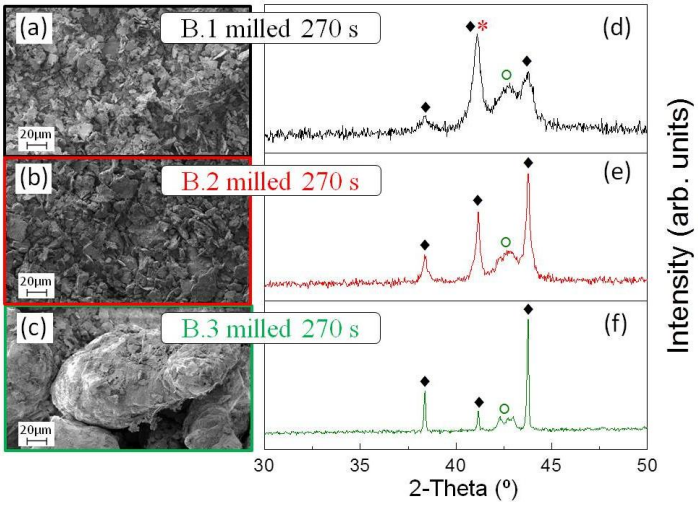

Figure 9. SEM images ((a), (b) and (c)) and XRD patterns ((d), (e) and (f)) of the milled B samples with different starting particle size: <36 μm, 45-75μm and 100-180 μm. Phase identification: (♦) ε-phase, (o) γ_2-phase, and (*) τ-phase.

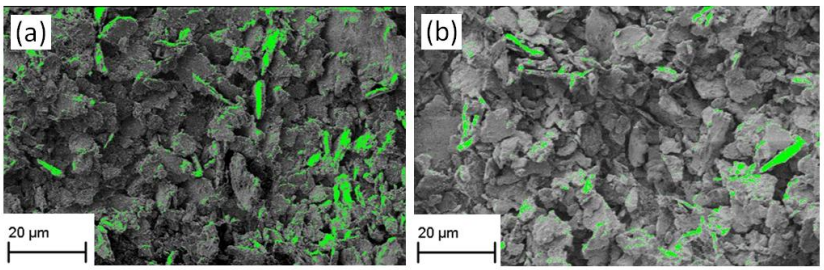

Figure 10. SEM images of (a) A.1 and (b) B.1 samples milled 270 s. Green color show the side view of flake-like particles which has been used to determine their thickness

Accordingly, the larger difference in the XRD diffractograms is observed between the diffractograms of the milled A.1 and A.2 samples (Fig. 8(d) and (e), respectively) and the diffractogram of the milled A.3 sample (Fig. 8(f)). For milled A.1 and A.2 samples the XRD patterns show broader peaks, however for the milled A.3 sample, a similar crystallographic structure to the corresponding starting powder is observed, confirming that the milling process is much more effective for reducing particle and crystallite size if the starting powders shows reduced particle size. In addition to that, the comparison of XRD diffractograms in Fig. 8 and 9 shows that the A samples (Fig. 8) present broader peaks and higher amorphization degree than B samples (Fig. 9). The A-samples have an excess of 3% of Mn in comparison with the most stable ε-phase composition ($Mn_{54}Al_{46}$) [64], which is presented in the B-sample. The excess of Mn makes it easier to refine and induce

amorphization, which is indicated by the broadening of the peaks of A samples. It is also remarkable partial ε to τ phase transformation in the A.1 and B.1 samples, with particle size below 36 μm, during the ball milling. This τ-phase formation has been only reported in high-energy ball milling experiments where it is possible to modify the ε-structure due to the high impact energy during the process [2].

Besides the change in the particle shape or the amorphization in the crystallographic structure, the efficiency of the nanostructuring can be quantified by the reduction of the crystallite size of the ε-phase. The mean crystallite size of the ε-phase of each milled sample is collected in Table 1.
Samples A.3 and B.3 present a crystallite size above 75 nm, very similar to the 100 nm determined for the corresponding gas-atomized powders, which means that the milling process induced a slight microstructure refinement.
Samples A.1 and A.2 have similar crystallite size, which indicates that for particles with size below 100 μm, the milling process promotes a deep modification of the crystallographic structure. Despite it is possible to modify the morphology and refine the microstructure of the B.2 sample, the high stability of the ε-phase in this composition avoids the reduction of the crystallite size below 40 nm after the milling process for intermediate particle size. Only the B sample with the smallest particle size has reduced its crystallite size below 20 nm, as the A.1 and A.2 samples.

Table 1. Mean crystallite size of the ε-phase in the different samples after the milling process. Error: 5 nm

	ε-phase mean crystallite size (nm)	
Particle size (μm)	Composition A	Composition B
(1) <36	7	15
(2) 45-75	9	40
(3) 100-180	80	95

Therefore, the analysis of the XRD patterns of the milled samples in comparison to the ones for the starting powders proves that the particle size and the composition of the initial MnAlC powder strongly influence the effectiveness of the milling process. A particle size below 100 μm is necessary to be able to transform the morphology and to perform a microstructure refinement by ultrafast ball-milling.
Annealing treatment was performed on gas-atomized and milled powders to transform the ε- into τ-phase for developing the magnetic properties.

XRD patterns of the gas-atomized samples annealed at 675 ° C are represented in Figure 11.

All the samples present more than 90% of τ-phase, with a similar crystallite size of 70±7 nm. The absence of ε-phase peaks confirms that the ε→τ transformation has been completed. The annealing temperature used in the experiments was higher than previous works with MnAl gas-atomized particles [6], due to the use of MnAl particles doped with C. It has been reported that the addition of C into the MnAl structure can raise the ε→τ transition temperature more than 100 ºC [71].

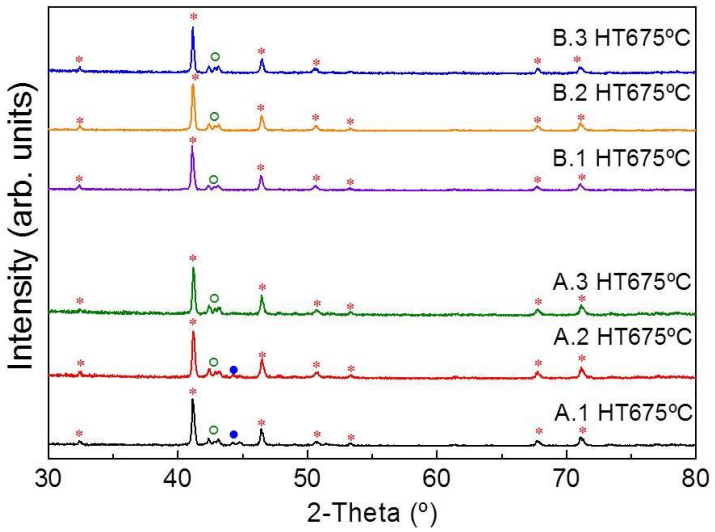

Figure 11. X-ray diffraction patterns of the different starting samples annealed at 675 ºC; (♦) ε-phase, (o) γ_2-phase, (●) β-phase, and (∗) τ-phase.

Figure 12 shows the XRD patterns of the milled and annealed samples. Together with the τ-phase, which is also observed in the annealed gas-atomized particles (Figure 11) a large amount of β-phase appeared in the milled and annealed samples.

The formation of β-phase in the MnAlC powder promotes significant changes in the magnetic properties of the material. The β/τ ratio for the different milled and annealed samples has been calculated using the reference intensity ratios (RIR) method [Zhou2018], and the results are collected in Table 2.

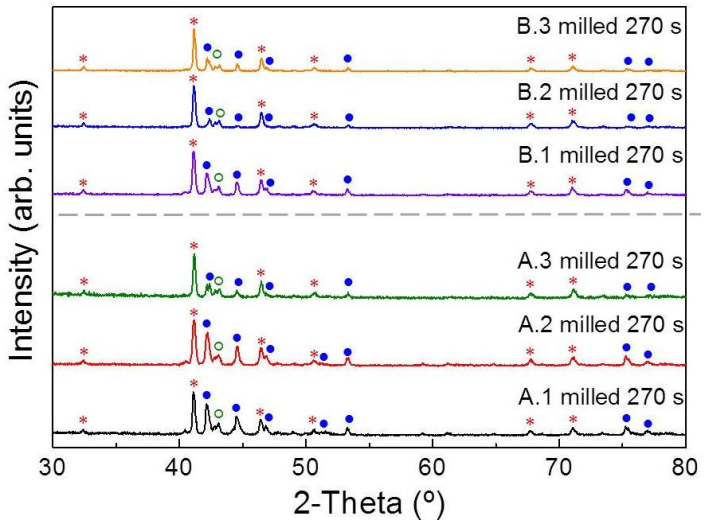

Figure 12. X-ray diffraction patterns of the different milled samples annealed at 675 ºC; (♦) ε-phase, (o) γ_2-phase, (●) β-phase, and (∗) τ-phase

Table 2. β/τ ratio of the milled samples annealed at 675 ºC in N_2 atmosphere. Error: 0.1

	β/τ ratio	
Particle size (μm)	Composition A	Composition B
(1) <36 μm	0.9	0.6
(2) 45-75 μm	0.9	0.4
(3) 100-180 μm	0.1	<0.1

Comparing the two compositions, it is observed that the A samples have significantly higher percentage of β-phase than the B samples. Avoiding the comparison between A.3 and B.3 samples (which do not present any significant change after the milling process), the A.1 and A.2 samples have a β/τ ratio of 0.9, a 50% higher than the B.1 sample (0.6), and more than 2 times higher than the B.2 sample (0.4). This difference comes from the starting material: composition A presents an excess of Mn that eases the formation of amorphous powder during the milling process. This amorphous Mn-rich powder will preferentially recrystallize, after the heat treatment, in β(Mn)-phase [rial2018]. The higher content of Mn in A samples makes the particles more fragile, so the milling process is more effective: if the particle size is small enough as to produce changes during the milling, the ε-phase presented in the A samples is amorphized, regardless the size range of the particles.

The partial amorphization of the powder causes an increment in the β/τ ratio from 0.1 to 0.9 after the annealing, in both the A.1 sample and the A.2. In contrast, the amorphization in the B samples during the milling is progressive,

making possible the control of the amount of β-phase by choosing the appropriate particle size (Table 2).

4.2.1 Magnetic characterization

The differences observed in the amount of crystallographic phases (β/τ ratio) will have a strong influence on the magnetic properties of milled and annealed powders. As the effectiveness of the nanostructuring is influenced by the initial particle size, graphs showing the hysteresis loops for the samples grouped according to the three different particle size ranges have been plotted (Figure 13). In each graph, the milled samples and the starting gas-atomized samples, annealed at the same temperature, are compared to differentiate the effect of the milling from the effect of the annealing processes on the magnetic properties of the particles.

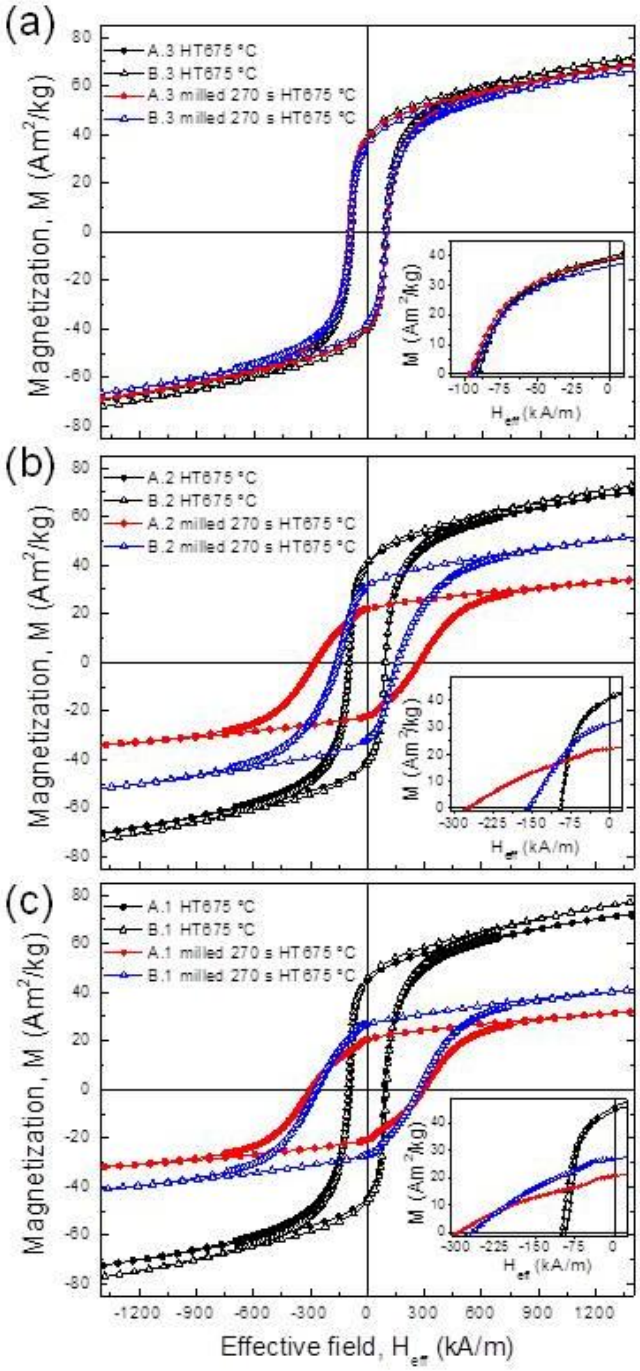

Figure 13. Hysteresis loops of the gas-atomized and milled powders with a particle size above (a) 100 μm, (b) between 45-75 μm and (c) below <36 μm annealed at 675 ºC

The samples with the largest particle size (> 100 μm) are compared in Figure 13 (a). In this case, the annealed milled and gas-atomized samples show similar hysteresis loops, which means that the short-milling time process does not promote significant changes on the magnetic properties of the samples. The difference in the composition does not have any effect on the magnetic properties, obtaining similar remanence magnetization (M_r = 38 Am^2/kg) and coercive field (H_c = 95 kA/m) in the four samples.

When the initial particle size is below 75 μm, it is observed a decrease in the magnetization of the milled samples in comparison with the starting powders, accompanied by a large increment in coercivity. As the τ-phase is the only ferromagnetic phase in the MnAl system and the β-phase has been proposed to act as pinning centers [63], the evolution of the magnetic properties can only be understood through the analysis of the MnAl phases content in each sample. H_c, M_r and M_{max} of the different milled and annealed samples and the β/τ ratio of each sample have been plotted in Figure 14.

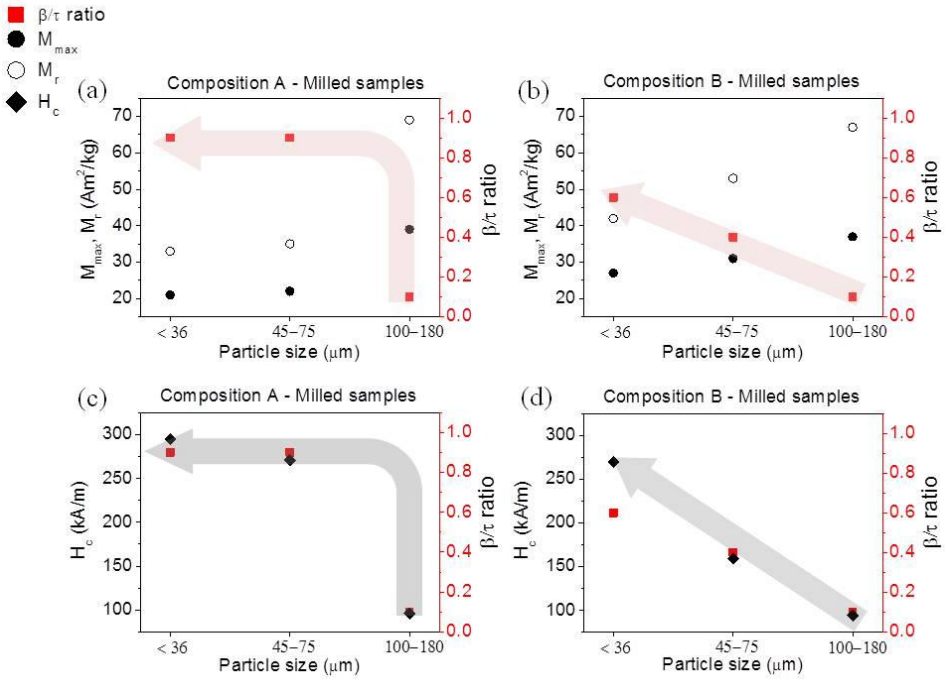

Figure 14. Comparison of the magnetization measured at the maximum applied field and the remanence (M_{max} and M_r, respectively) (a-b) and coercivity (H_c) (c-d) together with the β/τ-ratio of the different milled samples considering their initial particle size. Guide arrow has been plotted to follow the β/τ-ratio evolution of the A and B samples.

Figures 14 (a) and 14 (b) show that magnetization decreases when β/τ ratio increases, independently of the composition. As the only ferromagnetic phase of the system is the τ-phase, a decrease in the amount of this phase implies a reduction in the magnetization value. For the same particle size, it is observed how the milled B samples present higher magnetization than the milled A samples. This is due to the higher content of Mn in A samples which promotes the formation of β-phase, which explains the difference of almost 9 Am^2/kg between A.2 and B.2 samples (22 Am^2/kg vs 31 Am^2/kg) (Figure 13 (b)).

While the β-phase causes a decrease in the magnetization, its formation raises the coercivity of the milled samples above 250 kA/m (Figure 14 (c) and (d)). It was explained before how the fragility of the A samples, due to the excess of Mn in the samples, eases the formation of β-phase, and it increases the coercivity. If the particle size is below 100 μm, the coercivity increases up to 270 kA/m in the milled A.2 sample and up to 295 kA/m in the milled A.1 sample (Figure 14 (c)). Although the amount of β-phase causes an important detriment in the magnetization, the large increment in coercivity shows that is possible to obtain a successfully nanostructuring in the A samples through the ultra-fast ball milling process.

For the samples of composition B, which has a lower M content, the evolution of coercivity is more progressive (Figure 14 (d)). In this case, as the material is sturdier, the formation of the β-phase can be monitored by the control of the particle size. The control of the formation of the β-phase allows to raise the coercivity up to 150 kA/m in the B.2 sample by the increase of the β/τ ratio until 0.4, and up to 270 kA/m when the initial particle size is below < 36 μm (Figure 14 (d)).

The slow progression in the B samples avoids the formation of an excess of β-phase. As result of this, the samples A.2 and B.1 reach the same coercivity of 270 kA/m with a different β/τ ratio (0.9 and 0.6, respectively), so the sample B.1 reaches this coercive value with a remanence 22% higher than the remanence of the sample A.2.

The remanence of the milled B.1 has been achieved in the chapter 3, but the correct optimization of the starting material (i.e. composition and particle size) allows to obtain, after the nanostructuring process, a coercivity of 270 kA/m (3.4 kOe), 20% higher than the coercivity reported in the previous chapter (3.4 vs 2.8 kOe).

4.3 Conclusions

Gas-atomized MnAlC particles with two different nominal compositions have been synthesized by gas-atomization process and sieved in three different particles sizes ranges. In order to prove the influence of the nominal composition and the particle size in the effectiveness of the nanostructuring process, the different samples have been milled during 270 s and annealed at 675 ºC.

Along this study it has been simultaneously proved that:

- Ultrafast ball milling promotes significant changes in the morphology and in the atomic structure of the MnAlC powders. Furthermore, the short milling time needed in this process prevents the increment of the temperature during the nanostructuring process.

- High content of Mn in the starting ε-phase base powders promotes a high amorphization degree during the milling process, originating an increased content of β-phase after crystallization occurring during the annealing process.

- The β-phase is proposed to act as pinning center, raising the coercivity of the system. However, as the β-phase is not ferromagnetic, its formation causes a detriment in the magnetization.

- An efficient nanostructuring of the material through ultrafast-milling process can be achieved by the choice of initial particle size below 100 μm. The particle size of the initial powders strongly influences the nanostructuring of the particles developed during the milling process.

The control of the composition and choice of the initial particle size has allowed a successful tuning of the magnetic properties in the samples with an initial particle size below 36 μm. The sample with a nominal composition of $(Mn_{54}Al_{46})_{100}C_{0.75}$ has achieved a coercive field of 270 kA/m with a remanence magnetization close to 30 Am^2/kg, while the sample with the nominal composition of $(Mn_{57}Al_{43})_{100}C_{1.19}$ has increased its coercivity up to almost 300 kA/m after the ultrafast-milling process, with a lower remanence magnetization of 21 Am^2/kg.
A proper combination of the composition and starting particle size of MnAlC gas-atomized particles and an extremely short milling time allowed for tuning the morphology and microstructure of MnAlC particles and in consequence

the development of permanent magnet properties. This study represents an in deep knowledge of MnAl-based systems, showing that the optimized combination of the gas-atomization and ultra-fast ball milling processes is a highly effective and promising route for its implementation in large-scale synthesis and processing of isotropic MnAl-based permanent magnet powder.

Bibliography

[1] Luke G Marshall, Ian J McDonald, and LH Lewis. Quantification of the strain-induced promotion of τ-mnal via cryogenic milling. *Journal of Magnetism and Magnetic Materials*, 404:215–220, 2016.

[2] Michael Lucis, Timothy Prost, Xiujuan Jiang, Meiyu Wang, and Jeffrey Shield. Phase transitions in mechanically milled mn-al-c permanent magnets. *Metals*, 4(2):130–140, 2014.

[3] Hailiang Fang, Sofia Kontos, Jonas Ångström, Johan Cedervall, Peter Svedlindh, Klas Gunnarsson, and Martin Sahlberg. Directly obtained τ-phase mnal, a high performance magnetic material for permanent magnets. *Journal of Solid State Chemistry*, 237:300–306, 2016.

[4] Q Zeng, I Baker, JB Cui, and ZC Yan. Structural and magnetic properties of nanostructured mn–al–c magnetic materials. *Journal of Magnetism and Magnetic Materials*, 308(2):214–226, 2007.

[5] Anurag Chaturvedi, Rumana Yaqub, and Ian Baker. A comparison of τ-mnal particulates produced via different routes. *Journal of Physics: Condensed Matter*, 26(6):064201, 2014.

[6] M Ellner. The structure of the high-temperature phase mnal (h) and the displacive transformation from mnal (h) into mn 5 al 8. *Metallurgical Transactions A*, 21(6):1669–1672, 1990.

[7] J Rial, M Villanueva, E Céspedes, N López, J Camarero, LG Marshall, LH Lewis, and A Bollero. Application of a novel flash-milling procedure for coercivity development in nanocrystalline mnal permanent magnet powders. *Journal of Physics D: Applied Physics*, 50(10):105004, 2017.

[8] Ping-Zhan Si, Hui-Dong Qian, Chul-Jin Choi, Jihoon Park, and Hong-Liang Ge. A novel method for measuring the phase transformation temperature and enhanced coercivity in cold-rolled mnalcx (x= 0–5) alloys. *Journal of Magnetism and Magnetic Materials*, 451:540–545, 2018.

Chapter 5

5.General Conclusions and Future Perspectives

Isotropic nanocristalline MnAl(C) permanent powders produced by gas-atomization and nanostructured by ball milling methods have been studied. Along this research, it has been deepened in the formation of the possible phases in the material, controlling their evolution through different nanostructuring processes. This has allowed establishing a proper correlation between morphological, microstructural and magnetic properties. The approaches followed in this study can be summarized as:

- Study of the MnAl(C) phase transformation and its influence on the magnetic properties of the compound.
- Improvement of the permanent magnet properties of the MnAl(C) gas atomized powder through ball milling process and subsequent annealing.

Study of the MnAl(C) phases and their influence in the magnetic properties of the compound

Most of the experiments here presented have started with MnAl(C) powder with the ε-phase as the main crystalline phase, with a presence of this phase always superior to the 80% of the total crystallite powder. The main conclusions of the MnAl phase analysis are outlined:

- Nucleation of the τ-phase powder has been achieved, for the first time, by microstrain induced during the ball milling process on the ε-phase gas atomized MnAl(C) particles. The high impact energy transferred to the powder during the ball milling process –by using a high-density material (tungsten carbide) as milling media– eases an ordering transformation of the *hcp*-ε-phase into the *fcc*-τ-phase and with no need of applying a post-annealing process. Subsequent annealing was needed to achieve an enhanced τ-MnAl phase content, i.e. magnetization development.

- Onset temperature of the ε-to-τ transformation has been successfully reduced from 415 ºC for the gas atomized MnAl particles to 365 ºC after application of an unprecedented short milling time of 90 s. The fast-ball milling can reduce the thermal energy of the transformation by microstructural refinement, introduction of defects and inducement of strain.

- Post-annealing treatment of the as-milled powder allows for transformation of the ε-phase into the ferromagnetic τ-phase and, simultaneously, recrystallization of the amorphous powder (for a sufficiently extended milling time) into the non-magnetic β-phase.

- A correlation has been established between the MnAl phases obtained after the annealing process and the magnetic properties measured for the MnAl(C) powder. The rather low coercivity typically associated to a pure τ-phase MnAl alloy has been overcome by the creation of β-phase, with experimental results pointing to its role as pinning centers.

- Varying the Mn:Al ratio in the starting ε-phase based MnAl(C) gas atomized powder makes possible increasing the amorphization degree during the milling process. The favored crystallization of the β-phase from the amorphous MnAl(C) during post-annealing process influences significantly the permanent magnet properties of the alloy. In particular, modification of the initial composition from $(Mn_{57}Al_{43})_{100}C_{1.19}$ to $(Mn_{54}Al_{46})_{100}C_{0.75}$ has reduced the β/τ fraction content of the milled and annealed powder from 0.9 to 0.6, respectively, causing an improvement in the magnetization of the MnAl(C) compound without any worsening in its coercivity.

Improvement of the magnetic properties of the MnAl(C) gas atomized powder through ball milling process and subsequent annealing.

Isotropic nanocrystalline $Mn_{54}Al_{46}$ permanent magnet powder with quasi-spherical particles produced by gas-atomization process has been successfully improved by nanostructuring and controlled phase transformation:

- The use of the fast-ball milling process here used facilitates the nanostructuring process in milling times from just 30 to 270 s,

reducing drastically the typically milling time of several hours previously reported and thus avoiding undesired grain growth, relaxation and phase transformation effects resulting from temperature rise originated in long milling time experiments.

- The use of milling media with dissimilar densities (i.e. impact energy during milling) has allowed to control the formation of the β-phase and, in consequence, it has been possible to tune the magnetic properties of the MnAl system:

    - MnAl particles milled with tungsten carbide media achieve coercive values of 5 kOe through the increment of the strain above 0.25% and the formation of β-phase. The formation of an excess of β-phase content is accompanied by a detriment in magnetization, with values that can be below 20 emu/g, making necessary to find a compromise between coercivity and magnetization.

    - The use of steel as milling media halves the value of the energy transferred in a collision and thus results in less strained grains and diminished amorphization effects, reducing the β/τ ratio after post-annealing. As a consequence, the coercivity attains a value of 2.8 kOe (still much higher than about 1.5 kOe achieved by the annealed gas-atomized initial powder), while the remanence is maintained practically unchanged (about 30 emu/g) by comparison with the annealed gas-atomized powder.

- The choice of the milling time eases to control the nanostructuring process. Milling process during only 30 s (using tungsten carbide vials) is sufficient to induce strain in the particles and it is also short enough as to produce a low grade of amorphization in the particles, maintaining a low β/τ ratio after the annealing process. The combination of the induced strain and the low β/τ ratio causes a remarkable increment of the coercivity, above 3 kOe, while maintaining the remanence of the as-prepared gas atomized MnAl particles.

- Proper choice of the initial particle size is important to be able to tune the magnetic properties in the MnAlC system when exploring the short milling time regime. Particles with an average particle size above 100 μm cannot be successfully nanostructured by the ultrafast-milling method, while particles with same composition and an average particle size below 75 μm can reach coercivities above 3 kOe after nanostructuring..

The results here presented have shown that, despite the τ-phase is the only ferromagnetic phase, it is benefitial the implementation of a low amount of β-phase to achieve a compromise between magnetization and coercivity. Future researches to determine the precise position of the β-phase in the MnAl particles are necessary to optimize the amount of this phase, managing to increase the coercivity while maintaining the highest possible magnetization.

The optimization of MnAl particles produced by gas-atomization process and the use of a short milling time open the possibility of an industrial implementation of the process for large scale production, due to the short processing time and its foreseen cost efficiency. Tuning the magnetic properties under the premise of maintaining remanence value at least as good as that of the initial gas atomized MnAl(C) particles while increasing the coercivity is a promising method to make magnetically harder the actual MnAl powder,. On the other hand, the use of the high-coercive MnAl powder here obtained in an exchange-coupled composite with a magnetically soft material (providing high saturation magnetization) is a promising route in the attempt to try to substitute bonded rare earth-based permanent magnets.

Conclusiones Generales y Líneas Futuras de Investigación

Se ha realizado en esta tesis un estudio sobre el polvo nanocristalino e isotrópico de MnAl(C) producido por gas-atomizado y nanoestructurado por el método de molienda de bolas. A lo largo de esta investigación, se ha profundizado en la formación de las posibles fases en el material, controlando su evolución a través de diferentes procesos de nanoestructuración. Esto ha permitido establecer una correlación adecuada entre las propiedades morfológicas, microestructurales y magnéticas. La investigación realizada puede dividirse en:

- Estudio de la transformación de fases en el MnAl(C) y su influencia en las propiedades magnéticas del compuesto.
- Mejora de las propiedades de imán permanente del polvo gas-atomizado de MnAl(C) a través del proceso de molienda de bolas y un posterior calentamiento.

Estudio de las fases de MnAl(C) y su influencia en las propiedades magnéticas del compuesto.

La mayoría de los experimentos aquí presentados han comenzado con polvo de MnAl (C) con la fase ε como la fase cristalina principal, con una presencia de esta fase siempre superior al 80% del polvo cristalino total. Las principales conclusiones del análisis de fase MnAl son las siguientes:

- La nucleación del polvo de la fase τ se ha logrado, por primera vez, mediante microtensiones inducidas durante el proceso de molienda de bolas en las partículas de MnAl(C) con la fase ε. La alta energía de impacto que es transferida al polvo durante el proceso de molienda de bolas, gracias al uso de un material de alta densidad (carburo de tungsteno) como medio de molienda, permite una transformación ordenada de la fase hcp-ε en la fase fcc-τ sin necesidad de aplicar ningún calentamiento. Los calentamientos realizados después de la molienda sirvieron para mejorar la estructura de la fase, desarrollando una mayor magnetización.

- La temperatura de inicio de la transformación ε-a-τ se ha reducido con éxito desde los 415 ºC necesarios en las partículas de MnAl solamente atomizadas a 365 ºC, después de la aplicación de un proceso de molienda sin precedentes de 90 s. El proceso de molienda de bolas rápido permite reducir la energía térmica de la transformación mediante el refinamiento microestructural, la introducción de defectos y la inducción de tensión.

- El proceso de calentamiento aplicado al polvo molido permite la completa transformación de la fase ε en fase ferromagnética τ y, simultáneamente, la recristalización del polvo amorfo (producido durante el proceso de molienda en un tiempo suficientemente extendido) en la fase no magnética β.

- Se ha establecido una correlación entre las fases de MnAl obtenidas después del calentamiento y las propiedades magnéticas medidas para el polvo de MnAl(C). La baja coercitividad asociada a una aleación MnAl de pura fase τ ha sido aumentada mediante la cristalización de la fase β, que según los resultados experimentales parece que juega un papel clave como centros de fijación.

- La variación de la relación Mn: Al en el polvo atomizado de gas MnAl (C) con fase ε al inicio hace posible aumentar el grado de amorfización durante el proceso de molienda. La cristalización del MnAl(C) amorfo en fase β durante el calentamiento influye significativamente en las propiedades de imán permanente de la aleación. En particular, la modificación de la composición inicial de $(Mn_{57}Al_{43})_{100}C_{1.19}$ a $(Mn_{54}Al_{46})_{100}C_{0.75}$ ha reducido el contenido de fracción β/τ del polvo molido y recocido de 0.9 a 0.6, respectivamente, causando una mejora en la magnetización del compuesto de MnAl(C) sin empeorar su coercitividad.

Mejora de las propiedades de imán permanente del polvo gas-atomizado de MnAl(C) a través del proceso de molienda de bolas y un posterior calentamiento.

El polvo de imán permanente nanocristalino isotrópico $Mn_{54}Al_{46}$ con partículas cuasi-esféricas producidas por el proceso de gas-atomizado se ha mejorado con éxito mediante nanoestructuración y transformación controlada de las fases:

- El uso del proceso de molienda rápida de bolas utilizado aquí facilita el proceso de nanoestructuración en tiempos de molienda de solo 30 a 270 s, reduciendo drásticamente el tiempo de molienda de varias horas previamente reportado, y evitando así el crecimiento indeseado de granos, la relajación y los efectos de transformación de fase resultantes del aumento de temperatura originado en experimentos de tiempo de molienda largo.

- El uso de medios de molienda con densidades diferentes (es decir, diferente energía de impacto durante la molienda) ha permitido controlar la formación de la fase β y, en consecuencia, ha sido posible ajustar las propiedades magnéticas del sistema MnAl:

    - Las partículas de MnAl molidas con medios de carburo de tungsteno alcanzan valores coercitivos de 5 kOe a través del incremento de la tensión por encima del 0,25% y la formación de la fase β. La formación de un exceso de contenido de la fase β va acompañada de un detrimento en la magnetización, con valores que pueden estar por debajo de 20 emu / g, lo que hace necesario encontrar un compromiso entre la coercitividad y la magnetización.

    - El uso del acero como medio de molienda reduce a la mitad el valor de la energía transferida en las colisiones y, por lo tanto, produce granos con menor tensión y disminuye el grado de amorfización del polvo, reduciendo la relación β/τ después del calentamiento. Como consecuencia, la coercitividad alcanza un valor de 2.8 kOe (aún más alto que el valor de 1.5 kOe en el polvo inicial calentado), mientras que la remanencia se mantiene

prácticamente sin cambios (aproximadamente 30 emu/g) en comparación con el polvo gas-atomizado únicamente calentado.

- La variación del tiempo de molienda facilita el control del proceso de nanoestructuración. El proceso de molienda durante solo 30 s (usando medios de carburo de tungsteno) es suficiente para inducir tensión en las partículas y también es lo suficientemente corto como para producir un bajo grado de amorfización en las partículas, manteniendo una baja relación β/τ después del proceso de calentamiento. La combinación de la tensión inducida y el bajo valor de la relación β/τ causa un notable incremento de la coercitividad, por encima de 3 kOe, mientras se mantiene la remanencia de las partículas de MnAl gas-atomizadas.

- La elección adecuada del tamaño de partícula inicial es importante para poder mejorar las propiedades magnéticas en el sistema MnAlC al explorar el régimen de tiempo de molienda corto. Las partículas con un tamaño de partícula promedio superior a 100 μm no se pueden nanoestructurar con éxito mediante el método de molienda rápida, mientras que las partículas con la misma composición y un tamaño de partícula promedio inferior a 75 μm pueden alcanzar coercitividades superiores a 3 kOe después de la nanoestructuración.

Los resultados aquí presentados han demostrado que, a pesar de que la fase τ es la única fase ferromagnética, es beneficiosa la implementación de una baja cantidad de fase β para lograr un compromiso entre la magnetización y la coercitividad. Futuras investigaciones que permitan determinar la posición concreta de la fase β dentro de las partículas de MnAl ayudarán a optimizar la cantidad de fase β en el material, lo que logrará aumentar la coercitividad mientras se mantiene la mayor magnetización posible.

La optimización de las partículas de MnAl producidas por el proceso de gas-atomizado y el uso de un tiempo de molienda corto abren la posibilidad de una implementación industrial del proceso para la producción a gran escala, debido al corto tiempo de procesamiento y a la rentabilidad prevista. Ajustar las propiedades magnéticas bajo la premisa de mantener el valor de remanencia al menos tan bueno como el de las partículas de MnAl (C) iniciales mientras se aumenta la coercitividad es un método prometedor para hacer magnéticamente más duro el polvo de MnAl. Por otro lado, el uso del

polvo de MnAl de alta coercitividad aquí obtenido como material duro en un compuesto acoplado con un material magnéticamente blando (que proporciona una alta magnetización de saturación) es una ruta prometedora en el intento de intentar sustituir los imanes permanentes de inyección basados en tierras raras.

Appendix I

I.1 Cryomilling of melt-spun MnAl ribbons

The samples studied in this appendix have been produced and milled in collaboration with the group of Dr. Peter Svec at the Slovak Academy of Sciences (SAV) in Bratislava (Slovakia); and the group of Dr. Stefano Deledda at Institute for Energy Technology (IFE) in Lillestrøm (Norway).
The research herein presented focuses on the nanostructuring of melt-spun ribbons of MnAl.
Unlike the gas-atomized powder, the shape and the flexibility of the ribbons prevent an efficient nanostructuring of the sample through the ultrafast ball milling process.

The cryo-milling is a variation of mechanical milling, in which the powders are milled in liquid nitrogen ambient. The extremely low temperature of the liquid nitrogen (77 K) embrittles the ribbons, making possible to break the them. Therefore, the nanostructuring of the ribbons were achieved by the use of a cryo-milled system.

I. 1. Cryo-milled system.

In this system, the ribbons are introduced in a cylindrical vial beside a cylindrical piece of steel, which pulverizes the ribbons (Figure 1). The piece of steel is magnetically shuttled back and forth against the steel end plugs, crashing the ribbons and reducing their size.

A higher frequency means that the steel cylinder will be moving at higher velocity, increasing its kinetic energy. As the energy is directly transferred to the ribbons, if the frequency of the movement is higher, the cryo-milling process will be more energetic, increasing the morphological and microstructural changes in the material. Two different frequencies have been used in this work: 10 and 15 collisions per second (cps).

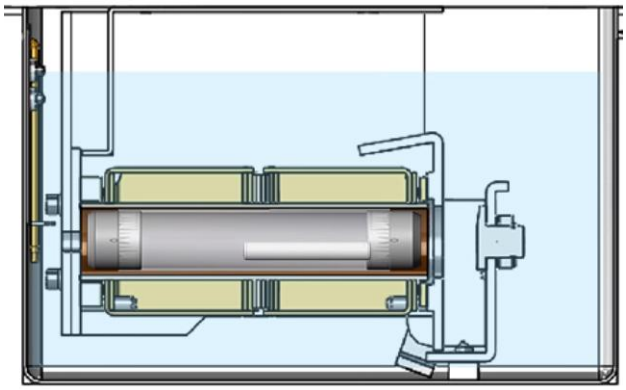

Figure 1. Diagram of the cryo-milling system.

The properties of the ribbons after the cryo-milling will be related with the frequency of the back and forth movement and with the milling time:

On the other hand, as it was explained in the previous chapters, it is known that an excessively milling time causes amorphization of the powder, resulting in a decreased magnetization. In order to optimize the milling time to increase the coercivity maintaining a reasonable remanence (above 20 emu/g), three different milling times have been used in the cryo-mill experiments: 4, 8 and 12 mins.

I. 2. Influence of the velocity and the milling time in the MnAl structure.

I. 2. 1. Microstructural properties and post-annealing process

The starting ribbons were prepared by planar flow casting (PFC) method [75] by Prof. Peter Svec in IPSAS, Bratislava. The initial samples consist on ribbon of 3mm wide and ~ 17 μm thick [75]. Only ε-phase is detected in the as-prepared ribbons, without any presence of τ-phase (Figure 2). The crystallite size of the initial ε-phase is 90 ± 10 nm.

The starting ribbons were milled during three different milling times (4, 8 and 12 min) at two different velocities, f= 10 and 15 cps.

The cryomilled process manages to pulverize the ribbons, transforming the initial melt-spun ribbons into powders with an average size below 50 μm (Figure 3). Independently the velocity or the milling time, all the cryomilled samples present a mix of particles with an average size below 10 μm and particles with a size between 20 and 50 μm. The milling also damages the microstructure, reducing the crystallite size of the ε- phase. Milling for 4 min at f=10 cps decreases the crystallite size to 20 nm (Table 1). Increasing the milling time up to 8 min or raising the frequency up to 15 cps, it is possible to reduce the crystallite size below 7 nm (Table 1). As in the previous experiments with gas-atomized particles [2] [3], the reduction of the crystallite size from 90 nm to less than 20 nm is accompanied by the formation of amorphous powders.

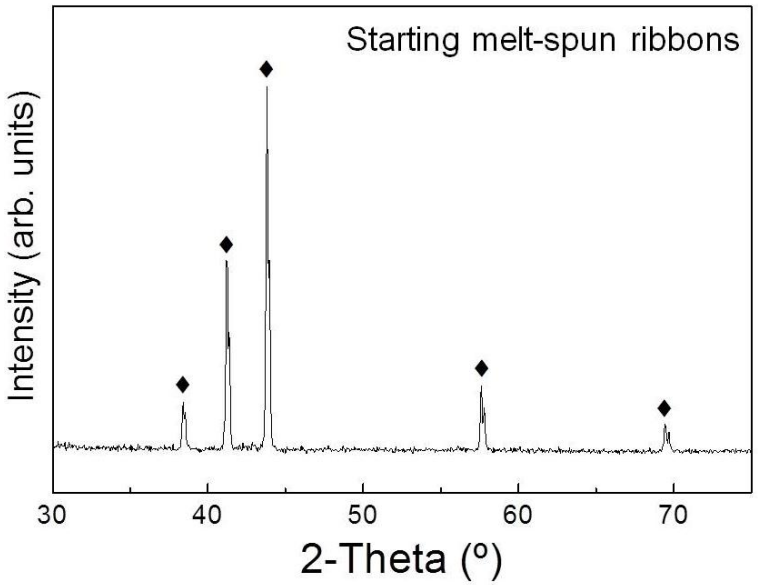

Figure 2. X-ray diffraction patterns of the starting ribbons. Phase indentification: (♦) ε-phase. Crystallite size: 90 ± 10 nm.

The increment of the milling time or the frequency causes an enhanced amorphization degree. Samples milled at f= 15 cps present peaks with lower intensity than the samples milled at f=10 (Figure 4). The same trend is observed when the milling time increases: maintaining constant the frequency, the ribbons milled 12 min presents lower intensity in the XRD peaks than the ribbons milled 4 min.

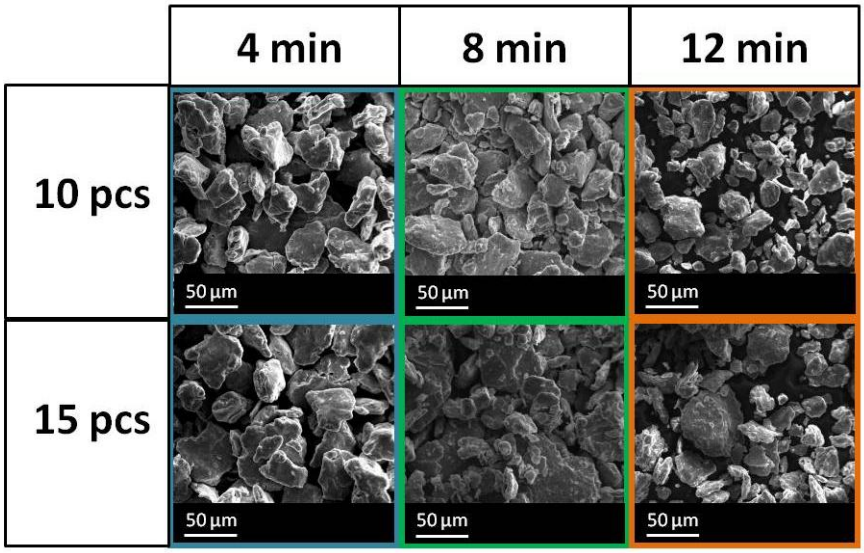

Figure 3. SEM images of the MnAl ribbons milled at different times (4, 8 and 12 min) and at different frequencies (10 and 15 cps). Scale bar: 50 µm.

Table 1. Mean crystallite size of the ε-phase in the different samples after the milling process. Error: 5 nm

Crystallite size (ε-phase)			
	4 min	8 min	12 min
f=10 cps	21 nm	7 nm	4 nm
f= 15 cps	7 nm	5 nm	3 nm

Regardless the frequency or the milling time, an annealing process is necessary to nucleate the τ-phase. In order to optimize the annealing process, the transition temperature of the different samples has been calculated by T-XRD maps and DSC measurements. Representative T-XRD maps of the starting ribbons and the samples milled 12 min at f=10 cps and f=15 cps are represented in Figure 5, and representative DSC measurements of the ribbons milled at f= 15 cps are represented in Figure 6.

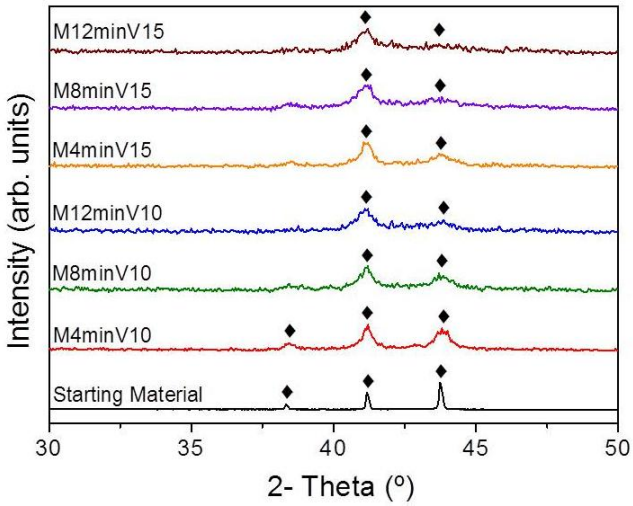

Figure 4. X-ray diffraction patterns of the starting ribbon and the as-milled samples. (♦) ε-phase

It is shown how, independently of the frequency, the cryo-milling process reduces the transition temperature of the starting ribbons 60 ºC: from the onset temperature of 430 ºC of the starting ribbons to the onset temperature of 370 ºC calculated in the milled ribbons, in agreement with the values obtained by DSC measurements (Table 2). It is remarkable that only 4 minutes are needed to reduce the transition temperature. The strong reduction in the crystallite size from 90 to 20 nm is enough to reduce the onset temperature until ~370 ºC. An increase in the milling time does not promote any change in the ε→τ transition temperature, causing exclusively a refinement in the crystallite structure (i.e reducing crystallite size and forming amorphous powder).

Table 2. Onset temperature of the τ-phase crystallization in the starting ribbon and in the milled samples.

Frequency	Onset temperature (Transformation of ε-to-τ phase)			
	Starting ribbon	Sample milled 4 min	Sample milled 8 min	Sample milled 12 min
	429 ºC			
f= 10 cps		369 ºC	368 ºC	368 ºC
f= 15 cps		368 ºC	368 ºC	368 ºC

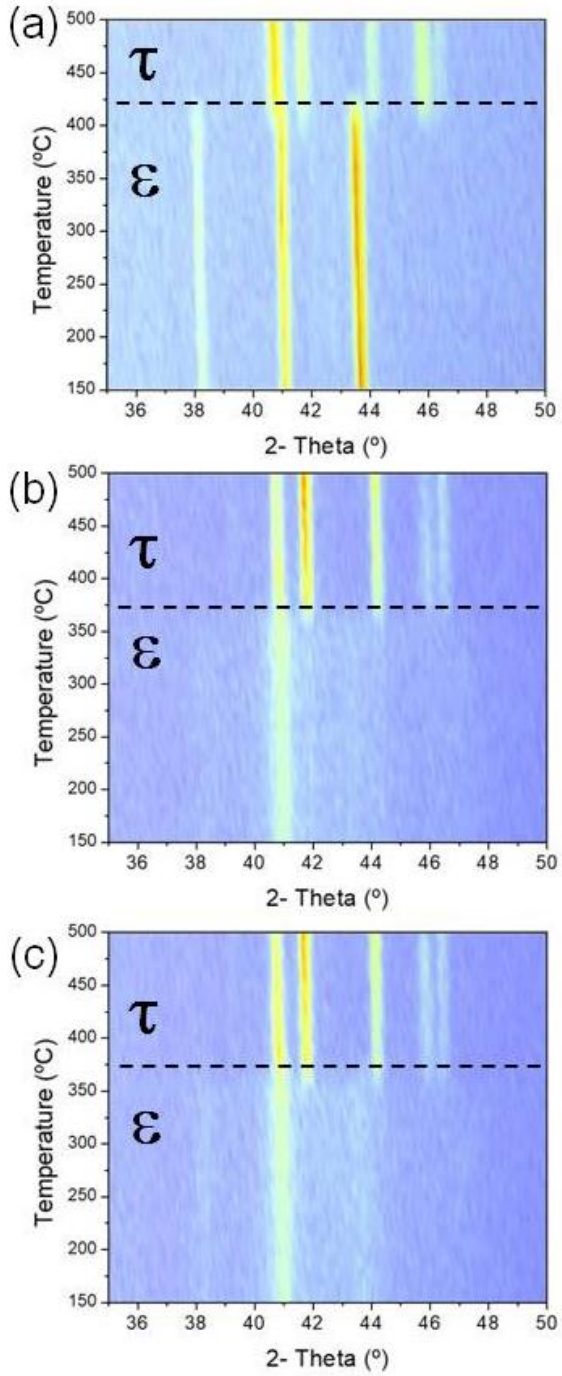

Figure 5. Temperature dependent X-ray diffraction pattern map of (a) as-spun MnAl ribbon; (b) ribbon milled for 12 min at 15 cps (b) and at 10 cps (c). Samples were annealed in-situ from 150 to 500 ºC using a temperature ramp of 1 K/min during recording of the measurement. Dashed lines are guide to the eyes showing the transition temperature for the transformation of ε- to τ-phase.

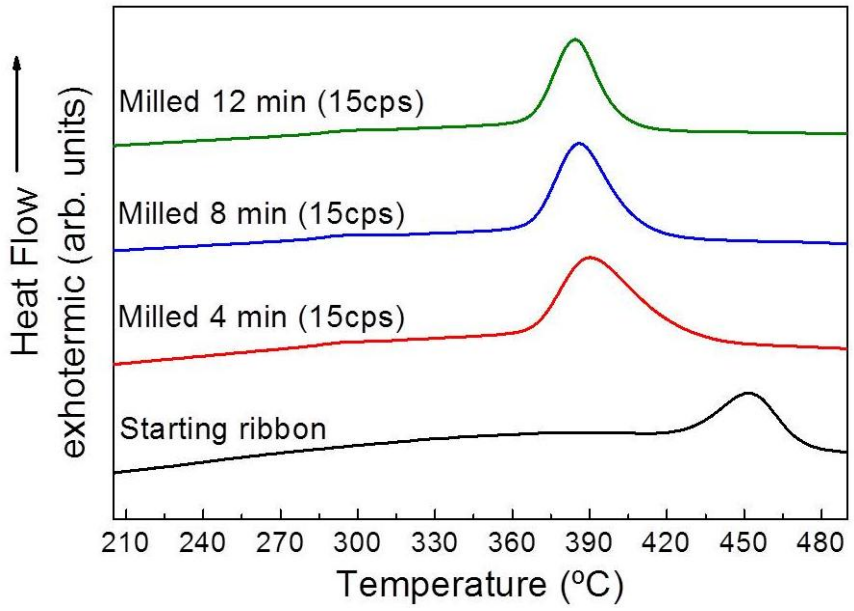

Figure 6. DSC measurements of the starting MnAl ribbons and the samples milled at 15 cps for 4, 8 and 12 min. Heating rate: 10 ºC/min.

In order to compare the starting and the milled samples, the annealed temperature has to be high enough as to finish the formation of the τ-phase in the starting material. For that reason, the starting material and the milled ribbons have been annealed at 450 ºC during 10 min in N_2 atmosphere. The XRD structure of the samples is represented in Figure 7.

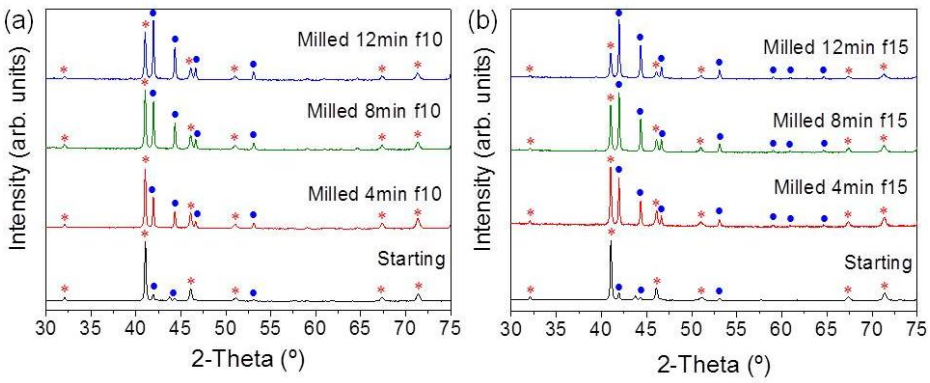

Figure 7. XRD patterns of the starting ribbon and the samples milled at 10 cps (a) and at 15 cps (b) annealed at 450 ºC for 10 min. (*) τ-phase and (●) β-phase.

Only peaks corresponding to the τ-phase and the β- phase are presented in the XRD measurements, without any presence of ε-phase peaks. The ratio

between both phases varies attending to the velocity or the milling time. It has been calculated the β/τ of each sample annealed at 450 ºC by the RIR method [4], and it is represented in Table 3.

Table 3. β/τ ratio in the different milled samples. Error: 0.1

Frequency	Milled 4 min β/τ ratio	Milled 8 min β/τ ratio	Milled 12 min β/τ ratio
f= 10 cps	0.8	1.0	1.6
f= 15 cps	0.9	1.6	3

When the frequency is 10 cps (Figure 7 (a)), the increment in the milling time raises the content of the β-phase, increasing the ratio between τ- and β- phase a 100%, from 0.8 to 1.6. The recrystallization of the β-phase in the cryomilled ribbons occurs in the same way that in the milled gas-atomized powder; the amorphous powder formed during the milling process recrystallizes into β-phase during the annealing process. For that reason, longer milling times cause higher β/τ ratio. The same trend is observed when the frequency is maintained at 15 cps; longer milling time increases the β/τ ratio up to 3, when the milling time is 12 minutes.

On the other hand, maintaining constant the milling time and varying the frequency, it is observed how the increment in the frequency causes a higher amorphization. Higher frequency causes higher impact energy that, in an extended time, will increase the content of amorphous powder.

During the first four minutes of cryomilling, the system pulverizes the ribbons and reduces the particle size, without causing a high amorphization in the system. As a result, the β/τ ratio is similar in samples milled at different velocities. Extending the milling time up to 8 minutes does not promote any particle size reduction (Figure 3), causing only changes in the microstructure (i.e. reduction of the crystallite size and formation of amorphous powder). In this case, the amount of β-phases increases in both cases, but the difference in the frequency promotes a higher amount of β-phase in the case of f=15 cps, causing a difference between the β/τ ratio of both phases of 0.6, i.e. a 60% of difference. This result shows how the increment in the velocity prevents the control of the nanostructure process, causing an excessive amorphization. An increment of the milling time up to 12 min produces higher amorphization in both samples, causing therefore an increase in the β/τ ratio in both samples until 1.6 for the sample milled at 10 cps and 3 in the sample milled at 15 cps.

The changes in the microstructure of the τ-phase are related with the crystallite size of the phase and the strain in the planes, that have been calculated by the Scherrer method [24] and are represented in the Table 4.

It is shown in Table 4 how, regardless the velocity; the samples milled the same time have similar crystallite size. The velocity of the process only increases the amorphization of the MnAl, without promoting any change in the crystallite size or the strain of the τ-phase. Therefore, the milling time is the decisive factor to reduce the crystallite size of the τ-phase or to induce strain in the particles.

It was explained before how the increment in the milling time causes higher modifications in the MnAl structure. For that reason, the samples milled 12 min present the lowest crystallite size of all the samples, with a mean crystallite size of ~ 50 nm. The reduction in the milling time avoids the diminution of the crystallite size, obtaining a mean crystallite size of ~60 nm when the samples are milled 4 minutes. Moreover, the cryomilling process increases the strain in the particles. Only 4 minutes of milling are needed to double the strain, from 0.09 to 0.18. Longer milling times only promote a slightly increment of 0.04.

The microstructure differences shown in Table 3 and Table 4 between the different samples are related with their magnetization differences, explained in the following section.

Table 4. Crystallite size and strain of the τ-phase of the starting and milled ribbons annealed at 450 ºC.

	Crystallite size (nm)	Strain (%)
Starting	70	0.09
m4 v10	60	0.18
m8 v10	58	0.19
m12 v10	52	0.21
m4 v15	61	0.18
m8 v15	56	0.19
m12 v15	50	0.22

I. 2. Magnetic properties

The XRD measurements have proven the effect of the cryo-milling process in the microstructure of the MnAl ribbons, reducing its crystallite size and inducing strain in the system. These modifications in the microstructure influence the magnetic properties. The hysteresis loops of the starting (as-spun) material and samples milled at different times and impactor frequency are represented in Figure 8, and the determined values for coercitivity (H_c), remanence magnetization (M_r) and magnetization at 20 kOe (M_{20kOe}) of each sample are represented in Table 5.

Table 5. Magnetic properties of the as-spun ribbons and the cryo-milled samples annealed at 450 ºC.

HT 450 ºC	Starting	M4min f10	M8min f10	M12min f10	M4min f15	M8min f15	M12min f15
H_c (kOe)	1.80	2.90	3.57	4.18	3.32	4.10	4.58
M_r (emu/g)	37.6	32.0	27.4	23.6	28.5	24.6	17.6
M_{20kOe} (emu/g)	80.7	57.5	47.3	40.0	50.3	41.4	29.6

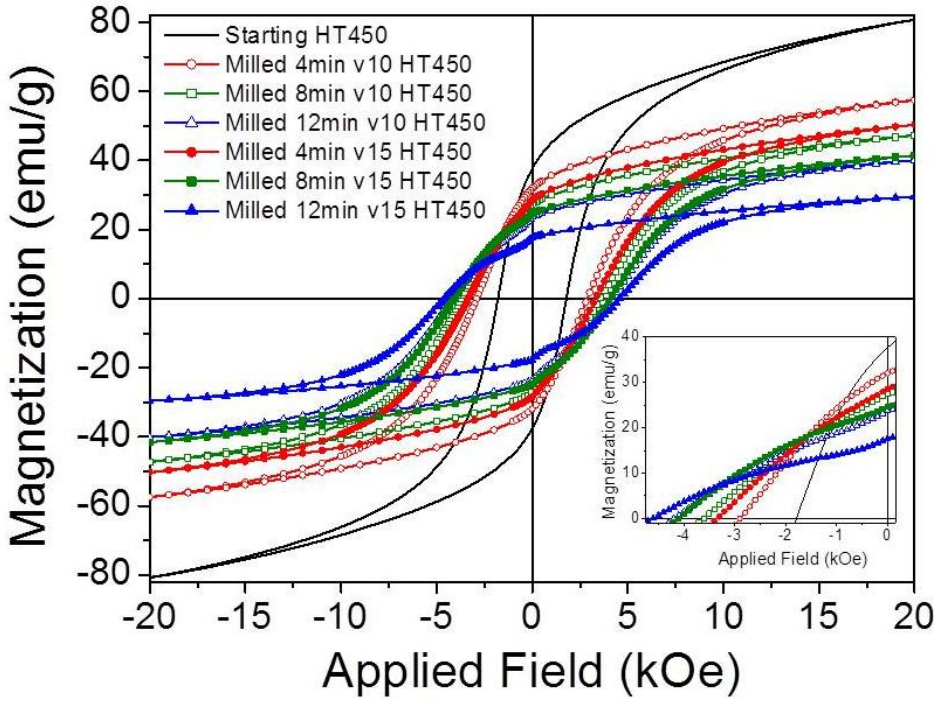

Figure 8. Hysteresis loop of the starting ribbon and the milled samples annealed at 450 ºC

The as-spun ribbon annealed at 450 ºC has the highest magnetization of all the samples (M_r= 37.6 emu/g; M_{20kOe}=80.7 emu/g). The pure ε-phase composition of the melt-spun ribbon diminishes the formation of β-phase during the annealing, obtaining an almost pure τ-phase material (Figure 7), with a percentage of β-phase less than 10%. On the other hand, as the cryomilled samples have higher amount of β-phase (Table 3), i.e. a decreased τ-phase content, the magnetization of the milled samples is lower than the starting material. The sample milled 4 min at f= 10 cps have a M_{20kOe} almost 23 emu/g lower (57.5 emu/g). Increasing the milling time up to 12 minutes, the M_{20kOe} decreases until 40 emu/g.

However, the difference in M_{20kOe} of 33 emu/g between the starting and the sample milled 4minutes is reduced to just 5.6 emu/g in remanence (37.6 vs 32.0), due to the high strain induced in the milled powder during the cryomilling process. The strain in the powder hinders the desmagnetization process, maintaining in remanence more than 55% of the M_{20kOe} of the milled powders. In comparison, the starting material just maintains a bit more of the 45% of its magnetization at 20 kOe. It proves that, despite the formation of β-phase owing to the amorphization during the milling process, the quadrature of the hysteresis loops achieved through the induction of strain in the particles eases to maintain a competitive remanence. The same trend is observed in the samples milled with f= 15 cps, where the magnetization at 20 kOe decreases until 50 emu/g when the sample is milled during 4 minutes, and until 30 emu/g when the milling time is increased from 4 to 12 minutes. As in the previous case, the remanence magnetization undergoes a smaller drop than the M_{20kOe}, maintaining more than the 55% of the M_{20kOe} in remanence.

Besides the increment in the $M_r/M_{20\ kOe}$ ratio, the cryo-mill process also raises the coercivity (H_c) of the MnAl ribbons, as it is shown in Figure 8. Coercivity of the cryomilled powders increase with the milling time, and the samples milled at higher frequency (15 cps) have higher coercivity than the samples milled at 10 cps.

Independently of the frequency, the increment in the milling time increases the coercivity owing to the higher level of nanostructuring achieved. The β-phase (Table 3), which has been argued to act as pinning center [81], contributes to increase the coercivity in the system. In addition to the β-phase, the strain in the particles is blocking the desmagnetization process[80], raising also the coercivity. The combination of these two parameters explains the trend observed in Figure 8.

The starting material, the sample with the combination of lowest β/τ ratio and lowest strain, presents the lowest H_c of all the samples, 1.8 kOe. When the ribbons are cryomilled only 4 minutes, the strain and the β-phase generated ease to raise the coercivity up to 2.9 kOe when the frequency is 10 cps; and to 3.4 kOe if the frequency is 15 cps. If the milling time is increased from 4 to 8 minutes, both samples raise their coercivity (3.6 kOe at 10 cps and 4.2 kOe at 15 cps). In both cases the improvement is similar: 0.7 kOe or 0.8 kOe in comparison with the ribbons milled 4 minutes. This increment is supported by the formation of more β-phase.

As it is observed in Table 5, the sample milled 4 min at 15 cps has only 250 Oe less coercivity than the sample milled 8 min at 10 cps. The small difference in the β/τ ratio between these samples (0.9 vs 1.0 (Table 4)) explains the small difference between their coercivity.

After milling for 12 min, the longest milling time considered in this work, the milled ribbons achieved their maximum H_c of 4.2 kOe (v=10 cps) and 4.6 kOe (v=15 cps). These values are higher than those previously reported by Marshall et al [20] and Fang et al. [9]. Marshall et al reported a coercivity of almost 3 kOe after 10h of cryomilling, and Fang et al reported a superior coercivity of 3.8 kOe after 2h of cryomilling.

However, the high amount of β-phase that has been necessary to develop a coercivity above 4.7 kOe have reduced its remanence magnetization under 20 emu/g, so that it makes mandatory to explore alternatives (e.g. coupled to a magnetically soft material providing high saturation magnetization) before it might be considered for permanent magnet applications. On the other hand, the use of a lower frequency (10 pcs) makes possible to induce strain in the sample and to maintain the magnetization above 20 emu/g. The sample milled 12 minutes at 10 cps present a high coercivity of 4.3 kOe with a remamence magnetization which is 30% higher than the ribbon milled at 15 cps (23.6 vs 17.5 emu/g).

I. 3. Conclusions

MnAl ribbons produced by melt-spinning were milled through the cryomilling technique. The extremely low temperature of the liquid nitrogen (77 K) used during the cryomill process embrittles the ribbons, making possible to break them into particles with an average size below 40 μm in only 4 minutes of milling. Independently on the frequency (f= 10 and 15 cps) or the milling time (4-12 min), the cryomill process diminish the crystallite size of the ε-phase below 20 nm and reduce the onset of the $\varepsilon \rightarrow \tau$ transition by 60 ºC.
It has been shown how is possible, through the cryomill process, to induce strain in the powders and, at the same time, to form amorphous powder that will recrystallize into β-phase during the annealing process. Longer milling time increases the changes in the microstructure, raising the strain and causing an increase of the β-phase content during the annealing step. As these two factors block de desmagnetization, the increment of the milling time increases the coercivity of the system. Cryomilling during just 4 min at 10 cps promotes an increment in the coercivity of a 50% in comparison with the starting material, maintaining the remanence above 30 emu/g. An increment of the milling up to 12 min time raises the coercivity until 4.3 kOe, reducing the remanence magnetization to 24 emu/g.

Moreover, hard material with coercivity above 4.5 kOe has been achieved by the combination of long milling time (12 min) and the use of high frequency (15 pcs), that produces a strain of 0.22% and a β/τ ratio of 3. Nevertheless, the high amount of β-phase needed to raise the coercivity reduces the remanence magnetization (18 emu/g).

The use of cryomill is presented as a successful and promising method to nanostructure MnAl ribbons. The low temperature of the milling has allowed obtaining a particle size reduction that had not been possible to obtain by the dry fast-milling process. Furthermore, the control of the milling process by the choice of the milling time or by the velocity allows tuning the magnetic properties.

Bibliography

[1] I Janotová, P Švec Sr, P Švec, I MatÊ¼ko, D Janickovic, J Zigo, M Mihalkovic, J Marcin, and I Škorvánek. Phase analysis and structure of rapidly quenched al-mn systems. *Journal of Alloys and Compounds*, 707:137–141, 2017.

[2] J Rial, M Villanueva, E Céspedes, N López, J Camarero, LG Marshall, LH Lewis, and A Bollero. Application of a novel flash-milling procedure for coercivity development in nanocrystalline mnal permanent magnet powders. *Journal of Physics D: Applied Physics*, 50(10):105004, 2017.

[3] JY Law, J Rial, M Villanueva, N López, J Camarero, LG Marshall, JS Blázquez, JM Borrego, V Franco, A Conde, et al. Study of phases evolution in high-coercive mnal powders obtained through short milling time of gas-atomized particles. *Journal of Alloys and Compounds*, 712:373–378, 2017.

[4] Xiang Zhou, Dong Liu, Hongling Bu, Liangliang Deng, Hongmei Liu, Peng Yuan, Peixin Du, and Hongzhe Song. Xrd-based quantitative analysis of clay minerals using reference intensity ratios, mineral intensity factors, rietveld, and full pattern summation methods: A critical review. *Solid Earth Sciences*, 3(1):16–29, 2018.

[5] AL Patterson. The scherrer formula for x-ray particle size determination. *Physical review*, 56(10):978, 1939.

[6] Luke G Marshall, Ian J McDonald, and LH Lewis. Quantification of the strain-induced promotion of τ-mnal via cryogenic milling. *Journal of Magnetism and Magnetic Materials*, 404:215–220, 2016.

[7] F Bittner, J Freudenberger, L Schultz, and TG Woodcock. The impact of dislocations on coercivity in l10-mnal. *Journal of Alloys and Compounds*, 704:528–536, 2017.

[8] F. JimÃ©nez-Villacorta L.H. Lewis. Perspectives on permanent magnetic materials for energy conversion and power generation. *Metallurgical and Materials Transactions A*, 44:220, 2013.

[9] Hailiang Fang, Johan Cedervall, Daniel Hedlund, Samrand Shafeie, Stefano Deledda, Fredrik Olsson, Linus von Fieandt, Jozef Bednarcik, Peter

Svedlindh, Klas Gunnarsson, et al. Structural, microstructural and magnetic evolution in cryo milled carbon doped mnal. *Scientific reports*, 8(1):2525, 2018.

[10] Q Zeng, I Baker, JB Cui, and ZC Yan. Structural and magnetic properties of nanostructured mn–al–c magnetic materials. *Journal of Magnetism and Magnetic Materials*, 308(2):214–226, 2007.

Appendix II

II.2. Synthesis of MnAlC/polymer composites for the extrusion of flexible and continuous permanent magnet filaments

In this appendix, it is reported the synthesis process of composite materials made of gas-atomized MnAlC magnetic particles embedded into a polyethylene polymer matrix with a high filling factor (over 85%)[1]. Composites were extruded into continuous and flexible magnetic filaments to be used in advanced technologies for PMs fabrication, such as 3D-printing. The possibility of tailoring the morphology and, consequently, the magnetic properties of the composite materials and magnetic filament is studied by tuning their filling factor, i.e. mass of magnetic material into the composites and filaments.

II.1 Synthesis of the polymer/PM-particles composites and fabrication of magnetic filament

The magnetic filament was prepared using gas-atomized MnAlC powder as magnetic material and polyethylene (PE) as the polymer matrix where the magnetic particles embedded.

The gas atomized MnAlC powder used to prepare the magnetic filament presents a composition of $(Mn_{57}Al_{43})_{100}C_{1.19}$ and it shows quasi-spherical particles with an average particle size below 36 μm (Figure 1 (a)). Initial MnAlC powder presents non-ferromagnetic ε-based crystallographic structure (Figure 1 (b)) with a minor content of γ_2-phase, as it has been reported in previous studies [2].I In order to fabricate a magnetic filament, starting MnAlC particles were annealed at 650 ºC in N_2 atmosphere for 30 min to

transform the ε-phase into τ-phase (Figure 1 (c)) for developing the magnetization in the material.

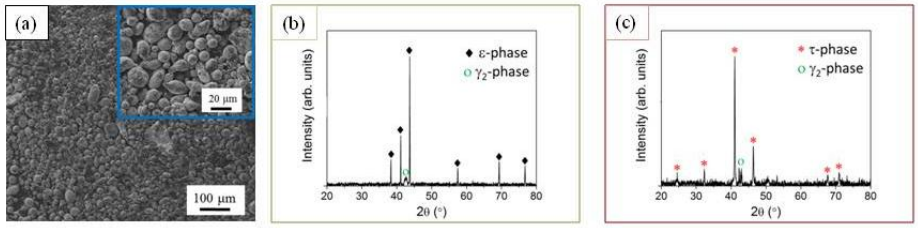

Figure 1. (a) SEM image of the starting MnAlC particles; and X-ray diffraction pattern showing the crystallographic structure of (b) the ε-based starting particles and (c) the τ-phase annealed particles.

The τ-phase MnAlC powder was embedded into a PE matrix by the solution casting method [3][4], being both starting material (magnetic particles and polymer) in powder-state. The amount of MnAlC particles into the PE matrix was tuned by tailoring the mass of materials used during the synthesis process. The magnetic composite was synthesized in several steps, following the process shown in Figure 2.

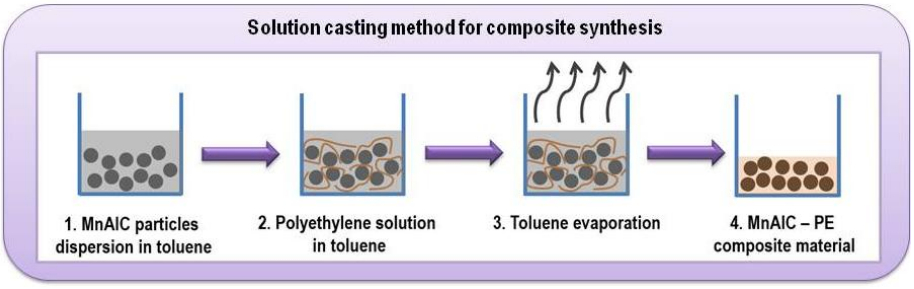

Figure 2. Scheme of the solution casting method used for the synthesis of MnAlC-PE composite materials.

Firstly, MnAlC particles were dispersed in 50 mL of toluene using magnetic stirring (Figure 2-1). While particles dispersion, the solution containing the magnetic particles and the solvent was heated up from room temperature up to 85 °C, temperature at which the polymer can be solved [4][5]. The amount of MnAlC particles ranged from 4.5 to 7.5 g in order to tune the filling factor of the composite.

Secondly, once the temperature was reached and stable, 1.5 g of PE powders were added to the solution (Figure 2-2).The amount of PE powder in comparison to the magnetic particles is lower due to the aim of obtaining

composite materials with an enhanced filling factor (i.e. over 60%). The solution was kept at 85 °C for 1 h to dissolve the PE and to form a polymeric matrix around the MnAlC particles.
Then, the solution temperature was reduced down to room temperature and the solution was kept at that temperature for residual toluene evaporation (Figure 2-3 and 2-4).

In this work, two different composites, hereinafter composite 1 and composite 2, were obtained, with a filling factor of 86.5 and 63.1 %, respectively. In order to have enough material for filament extrusion, the amount of composite materials was scaled up for each composition. The final composite mass used for extrusion experiments was 25 g.

The composite in pellets-like shape produced by the solution casting method were extruded into the final magnetic filament using an extruder from Noztek Ltd., based on a screw which transports the composite from the feeding hopper down to the extrusion nozzle. The filaments were fabricated by applying an extrusion temperature of 120 °C and using a nozzle with a nominal output diameter of 1.75 mm, being both parameters suitable to obtain an extrusion speed of approximately 20 cm/min. The composite mass used for the extrusion experiments was enough to obtain 12 m of filament with each composite, with a homogeneous circular cross section and a diameter of 1.75 mm.

However, it was observed during the extrusion process that part of the magnetic particles of the composites got stuck in the extruder screw wall due to the exerted pressures, i.e. originating a decrease in the filling factor of the extruded filaments. The extrusion of composite 1 (filling factor of 86.5 %) resulted in a filament with a filling factor of 72.3%; and the extrusion of composite 2 (filling factor of 63.1 %) led to a filament with a filling factor of 52.1%.

II.2 Characterization of as-prepared composites and as-extruded filaments.

The morphology of each as-prepared composite material and their corresponding extruded filaments is shown in Figure 3. It is observed that, for both compositions, the MnAlC particles are successfully embedded in the PE

matrix. An homogeneous morphology is also observed for the corresponding extruded filaments.

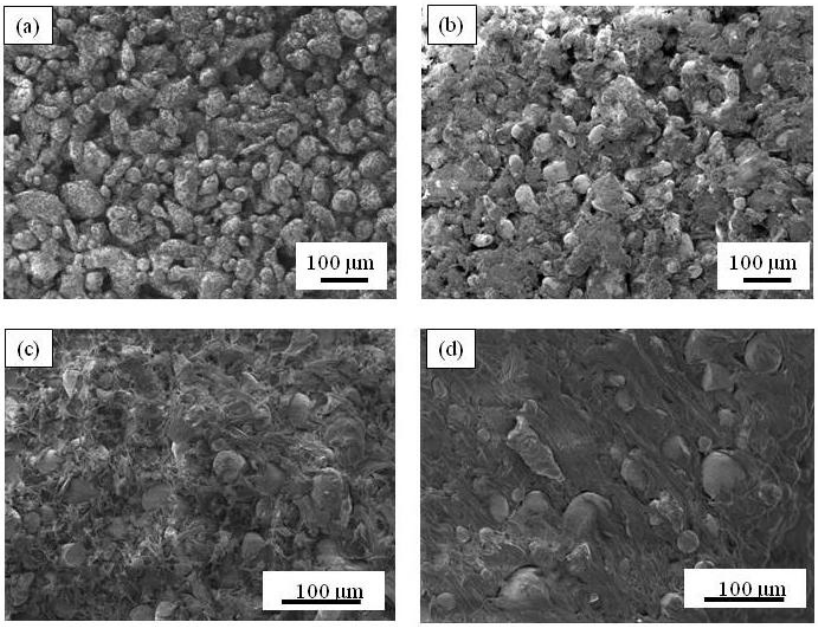

Figure 3. SEM images of the composite materials with a filling factor of (a) 86.5 % and (b) 63.1%, and the corresponding extruded filaments with a filling factor of (c) 72.3 % and (d) 52.1 %.

It is also possible to appreciate in Figure 3 the differences in the filling factor between the four samples. In the as-synthesized composite 1 (Figure 3(a)), the sample with the highest filling factor, the PE partially covers the magnetic particles (see dark contrast areas around MnAlC particles in Figure 3(a)). However, for the as-synthesized composite 2 (Figure 3(b)), where there is a higher amount of PE in the composite, PE agglomerates along the composite material. The morphology of the filaments, which present a lower filling factor than the as-synthesized composites show a higher amount of PE in their cross section than their corresponding as-synthesized composites (Figure 3 (c) and (d)).

The difference in the filling factor will promote differences in the magnetization of each sample. The hysteresis loops of the reference τ-MnAlC powder and the MnAlC-PE composites are plotted in Figure 4 (a). Figure 4 (b) shows a zoom in of the second quadrant of the hysteresis loops, which allows for better observing the coercive field, H_c, and remanence, M_r, values of the samples. The filling factor of the composites, referred to the mass of

magnetic material contained inside, was obtained considering the values of the magnetization at the maximum applied field (M_{20kOe}) and calculated by the ratio between M_{20kOe} for each material and that one for MnAlC starting powder. The values of the magnetic properties for each material (H_c, M_r and M_{20kOe}) are listed in Table 1. The highest values of M_r and M_{20kOe} are obtained for MnAlC powder, and they decrease proportionally to the amount of magnetic particles embedded into the polymeric matrix. Coercivity remains practically unchanged among the different samples and the slight differences (below 4%) may be ascribed to heating effects [refs] during the composite synthesis. Several samples of each composite material were measured to check their homogeneity. A relative standard deviation (RSD) of 7.54 and 7.07 % was calculated for the magnetization of the composites 1 and 2, respectively. It is important to remark that in Table 1, the values of M_{20kOe} and M_r normalized to the corresponding filling factors show no significant variations for all processed materials (composites and filaments) under study.

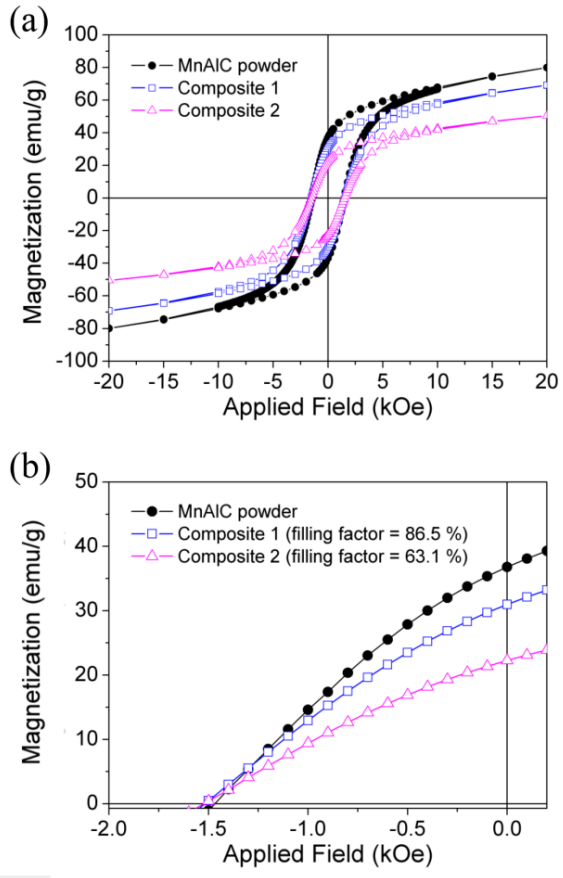

Figure 4. (a) Room temperature hysteresis loops of the starting MnAlC powder and the composites (1 and 2) with different filling factor (86.5 and 63.1% in mass, respectively); and (b) detail of the second quadrant of the hysteresis loops.

Table 1. Magnetic properties of MnAlC powder, MnAlC – PE composite materials and magnetic filaments: coercive field (H_c), remanence (M_r), and magnetization measured at a maximum applied magnetic field of 20 kOe (M_{20kOe}).

Sample	Filling factor (%)	H_c (kOe)	M_r (emu/g)	M_{20kOe} (emu/g)	M_{20kOe} / *filling factor* (emu/g)	M_r / *filling factor* (emu/g)
MnAlC powder	-	1.47	36.7	80.0	-	-
Composite 1	86.5	1.53	30.6	69.2	80.00	35.38
Composite 2	63.1	1.52	22.2	50.5	80.03	35.18
Filament 1	72.3	1.53	25.5	57.8	79.94	35.27
Filament 2	52.1	1.52	18.4	41.7	80.04	35.32

The proof that the magnetic properties of the MnAlC powder are not practically affected by the processing methods (composite synthesis and filament extrusion) comes from the comparison of the normalized hysteresis loops (i.e. normalized magnetization considering the filling factor of each processed material -composites and filaments). The normalized values for each magnetic material are gathered in Table 1, showing that, independently of the material, the normalized magnetization remains almost the same as compared to the magnetization of the starting MnAlC powder.

Technological work is in progress to manage an increase in the filling factor of the filament, i.e. enhanced magnetization values, by combining technological advances (redesign of the extruder) and material development (combination of MnAlC particles with different sizes and shapes).

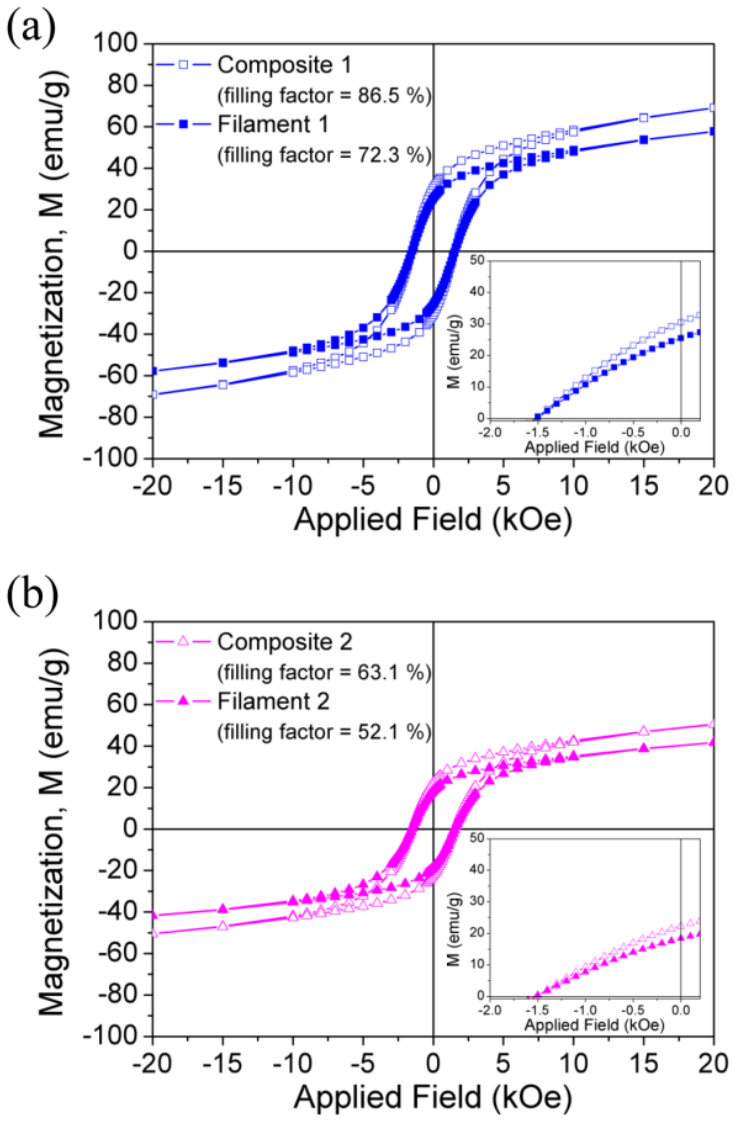

Figure 5. Room temperature hysteresis loops measured for extruded MnAlC – PE filaments with different filling factors expressed in mass: (a) 72.3% and (b) 52.1%. Hysteresis loops measured for the corresponding composites (1 and 2) are included for comparison. In both graphs, a detail of the second quadrant of the hysteresis loops is included as inset.

II.3 Conclusions

This work correlates the morphological, microstructural and magnetic properties of the first time reported MnAlC magnetic particles-based filament for its use in advanced fabrication techniques such as 3D-printing. Homogeneous composites consisting of MnAlC particles embedded in a PE matrix have been prepared through solution casting and used as precursors for filament extrusion. Importantly, in view of practical applications, no deterioration of the PM properties of the MnAlC particles was observed after composite synthesis and filament extrusion, with magnetization values scaling proportionally with the content of magnetic particles in the composites and in the filaments. The coercive field remains almost constant after the fabrication processes with a value of about 1.53 kOe for both the composites and the filaments. The filling factor of the composites and filaments (and consequently, their magnetic properties) can be easily tuned during the composite synthesis according to the final application. This study opens a new path for the application of bonding technologies (cold/warm compaction and advanced 3D-printing) to rare earth-free MnAl-based permanent magnet alternatives, allowing for arbitrary designs and realization of more efficient devices.

Bibliography

[1] Palmero E M, Rial J, de Vicente J, Camarero J, Skarman B, Vidarsson H, Larsson P-O and Bollero A, Development of permanent magnet MnAlC/polymer composites and flexible filament for bonding and 3D-printing technologies, Science and Technology of advances materials, 2018, 1, 465-473

[2] Chaturvedi A, Yaqub R, Baker I. Microstructure and magnetic properties of bulk nanocrystalline MnAl. Metals. 2014;4:20–27.

[3] Qureshi A, Mergen A, Eroğlu MS, et al. Dielectric properties of polymer composites filled with different metals. J Macromol Sci Phys Part A. 2008;45:462–469.

[4] Wong SL, Ngadi N, Abdullah TAT. Study on dissolution of low density polyethylene (LDPE). Appl Mech Mater. 2015;695:170–173.

[5] Achilias DS, Roupakias C, Megalokonomos P, et al. Chemical recycling of plastic wastes made from polyethylene (LDPE and HDPE) and polypropylene (PP). J Hazard Mater. 2007;149(3):536–542.

List of Publications

- V. Øygarden, J. Rial, A. Bollero, and S. Deledda, “Phase-pure τ-MnAlC produced by mechanical alloying and a one-step annealing route”, J. Alloys Compd. 779, 776 (2019).

- J. Rial, E.M. Palmero and A. Bollero, “Efficient nanostructuring of isotropic gas-atomized MnAl powder by rapid milling (30 s)”, Engineering (2019) doi: https://doi.org/10.1016/j.eng.2019.03.013

- J. Rial, P. Švec, E.M. Palmero, J. Camarero, P. Švec Sr., and A. Bollero, “Severe tuning of permanent magnet properties in gas-atomized MnAl powder by controlled nanostructuring and phase transformation”, Acta Mater. 157, 42 (2018).

- E.M. Palmero, J. Rial, J. de Vicente, J. Camarero, B. Skårman, H. Vidarsson, P.-O. Larsson, and A. Bollero, “Development of permanent magnet MnAlC/polymer composites and flexible filament for bonding and 3D-printing technologies”, Sci. Technol. Adv. Mater. 8, 19 (1), 465 (2018).

- J. Rial, M. Villanueva, E. Céspedes, N. López, J. Camarero, L.G. Marshall, L.H. Lewis, and A. Bollero, “Application of a novel flash-milling procedure for coercivity development in nanocrystalline MnAl permanent magnet powders”, J. Phys. D Appl. Phys., 50 (2017).

- J.Y. Law, J. Rial, M. Villanueva, N. López, J. Camarero, L.G. Marshall, j. S. Blázquez, J. M. Borrego, V. Franco, A. Conde, L. H. Lewis and A. Bollero, “Study of phases evolution in highcoercive MnAl powders obtained through short milling time of gas-atomized particles”, J. Alloys Compd. 712, 373 (2017).

List of Abbreviations

bbc	body-centered cubic
DSC	**D**ifferential **S**canning **C**alorimetry
EDX	**E**nergy **D**ispersive **X**-ray
fcc	face-centered cubic
hcp	hexagonal closest packed
PM	**P**ermanent **M**agnet
RE	**R**are **E**arth
SEM	**S**canning **E**lectron **M**icroscope
TEM	**T**ransmission **E**lectron **M**icroscope
TM	**T**ransition **M**etal
T-XRD	**T**emperature **X**-**R**ay **D**iffraction
VSM	**V**ibrating **S**ample **M**agnetometer
XRD	**X**-**R**ay **D**iffraction

List of symbols

a	Lattice patameter (Å)
$(BH)_{max}$	Maximum energy product (MGOe)
H_c	Coercive field or coercivity (Oe, A/m)
M_r	Remanence magnetization (emu/g, A/m)
M_s	Saturation magnetization (emu/g, A/m)
M_{20kOe}	Magnetization at 20 kOe (emu/g, A/m)